

A Kilometre-range Distributed Relative Humidity Fibre Sensor

Présentée le 4 mars 2022

Faculté des sciences et techniques de l'ingénieur
Groupe SCI STI LT
Programme doctoral en photonique

pour l'obtention du grade de Docteur ès Sciences

par

Tiago Filipe PIMENTEL DAS NEVES

Acceptée sur proposition du jury

Prof. C. Moser, président du jury
Prof. L. Thévenaz, directeur de thèse
Prof. F. Berghmans, rapporteur
Prof. S. Girard, rapporteur
Prof. F. Sorin, rapporteur

"The reward of the young scientist is the emotional thrill of being the first person in the history of the world to see something or to understand something. Nothing can compare with that experience"

– Cecilia Payne-Gaposchkin

To my parents.

Acknowledgements

First of all, I would like to thank my supervisors for the support and opportunity to accomplish my PhD objectives. I want to thank Paolo Petagna for the unique and amazing opportunity to work at CERN and for the amazing 7 years that we worked together. From the very first moment of my stay at CERN, Paolo was the best supervisor I could ask for, and was always present and ready to help me, clarifying all my doubts and supporting all my ideas and plans. Then, I would also like to express my gratitude to Prof. Luc Thévenaz for the excellent academic supervision and guidance, but also for the way that he received me in his laboratory. Apart from the pleasant and multi-cultural atmosphere in the group, Prof. Luc always promoted several social events that gave me the opportunity to know better Switzerland, to meet his family and lifestyle, and to live unique life experiences in the region.

I would also like to thank the member of my jury, Prof. Christophe Moser, Prof. Francis Berghmans, Prof. Sylvain Girard and Prof. Fabien Sorin for accepting to review and examine my thesis.

Naturally, during the last 7 years, I had the chance to interact with a lot of people from EPFL and CERN. I want to thank all the past and current members of GFO, especially Li, Simon, Flavien, Malak, Suneetha, Fan, Kenny and Zhisheng for all moments together. From CERN, firstly, I would also to thank all the EP-DT-FS section members for the daily interaction and coffees at Crystal Palace. Then, thanks to the KT members who always supported my ideas especially Ash and Filipe. Finally, thank you Lorenzo for all your help during the last years and for becoming a good friend that I will keep for life.

I want to extend the acknowledgements, as well, to FiberTech Lille (IRCICA - Université de Lille) for providing some of the optical fibres studied in this dissertation, and to Regina and Hugo, from Universidad de Alcalá, for providing the optical setup used in some of the tests campaign.

Additionally, I want to thank my friends who supported me from the first day. My football friends for all the goals that we scored together, my snowboarding friends for all the jumps that we failed together. To the Portuguese crew in Switzerland/France: Araújo, Meireles, Fraga, Alex, Filipe M., Rita, Diego, André H., Marco, Cláudio, Florêncio, Pierre, Zé Carlos, Afonso, Filipe R. and Carlota, and to all the others with whom I spend good time. A special thanks to Andreia, Miguel and Catarina for the shared moments and hours of chatting, cooking and eating, and

a huge thanks to Carolina for the fruitful discussions and for the endless and unconditional support given during the last months. To my friends from Coimbra: João, Flag, Carlos, Manel, Quim, Ana, Maria, Ju, Guida, Telma, Catarina and Filipa. Thanks for always receiving me back. Thanks as well to the Loop team, specially João and Bernardo for the support in the last months.

Last, but the most important, my gratitude to my whole family. To my brothers, my sisters, my nephews, my nieces but especially to the two most important persons of my life. My mother and my father, to whom I dedicate my work. Thank you for always supporting me no matter what, to always receiving me with a hot soup no matter what time I arrive but, mostly, for the unconditional support, comprehension and love that I feel every time I step into our home. This PhD was our shared dream and here you have it. From the bottom of my heart, it is for you.

Obrigado.

Lausanne, 2021

Tiago Neves

Abstract

Fibre optics sensors have been identified as very good candidates for environmental monitoring inside the silicon detectors operated at CERN's Large Hadron Collider. The objective of this dissertation is the development of a Relative Humidity (RH) distributed fibre optic sensor, based on coherent Rayleigh scattering, for long-distance applications using phase-sensitive optical time-domain reflectometry technique, which is a technique that is gaining the attention of industry and academy due to its ultra-high sensitivity.

Optical fibres are known to be intrinsically sensitive to temperature and strain; however the influence of humidity on coatings induces a secondary mechanical strain due to expansion/contraction when absorbing/desorbing water. Turning an optical fibre into a thermohygrometer requires a detailed investigation of the best coatings to measure RH and mitigate the cross-sensitivity with temperature. Several coatings were studied in order to find a fibre with an approximately constant humidity sensitivity at large range of temperature, as well as a purely temperature-sensitive optical fibre.

Polyimide-coated fibres are the best candidates for RH sensing over a temperature range from -20°C to 50°C , while the standard acrylate-coated fibre have a surprisingly non-negligible humidity sensitivity but a completely different behaviour at different temperatures.

Additionally, two families of humidity insensitive coated fibres were identified as excellent candidates for a pure temperature reference. The first is made of a multi-functional acrylate coating (Desolite) that provides a purely temperature-dependent measurement above 15° , with a negligible response at lower temperatures, while the second one uses a silicone composite that secures a complete immunity to humidity from -20°C to 50°C .

After identifying the best pair of coated optical fibres, an in-field application case was devised and validated at CERN. The new sensor makes use of a pair composed by a polyimide- and a desolite-coated optical fibres to monitor temperature and RH inside a block of concrete since the earliest moment of its curing process. The proposed solution represents a breakthrough improvement in the civil engineering monitoring systems.

Key words: fibre optics, sensing, relative humidity, temperature, distributed fibre sensing, phase-OTDR, Rayleigh scattering, coating, polyimide, acrylate, desolite, silicone, concrete.

Résumé

Les capteurs à fibres optiques ont été identifiés comme de très bons candidats pour la surveillance de l'atmosphère ambiante à l'intérieur des détecteurs au silicium exploités au Grand Collisionneur de Hadrons du CERN. L'objectif de cette thèse est le développement d'un capteur réparti d'humidité relative (RH) à fibre optique, basé sur la diffusion Rayleigh cohérente, pour des applications sur de longue distance utilisant la technique de réflectométrie optique temporelle sensible à la phase. Cette technique a gagné un intérêt certain en milieu industriel et académique, en raison de sa très haute sensibilité.

Les fibres optiques sont connues pour être prioritairement intrinsèquement sensibles à la température et à la déformation. Toutefois, l'influence de l'humidité sur leur gaine de protection induit une déformation mécanique supplémentaire due à l'expansion/contraction lors de l'absorption/désorption d'eau.

Transformer une fibre optique en thermo-hygromètre nécessite une étude détaillée des meilleurs matériaux formant la gaine primaire, pour mesurer l'humidité relative et la découpler de la sensibilité interférante à la température.

Plusieurs types de gânage ont été étudiés afin de trouver une fibre avec une sensibilité à l'humidité approximativement constante sur une large gamme de température, ainsi qu'une fibre optique purement sensible à la température. Les fibres revêtues de polyimide sont les meilleurs candidates pour la détection de l'humidité relative sur une plage de températures allant de -20°C à 50°C , tandis que les fibres standard revêtues d'acrylate ont une sensibilité à l'humidité non négligeable, mais une totale absence d'uniformité de la réponse à différente température.

De plus, deux familles de fibres gainées insensibles à l'humidité ont été identifiées. La première est composée d'un revêtement acrylate multifonctionnel (Desolate) qui fournit une pure mesure de température pour des températures supérieures à 15°C , avec une réponse restant toutefois négligeable à des températures inférieures, tandis que la seconde utilise un composite silicone qui garantit une immunité totale à l'humidité de -20°C à 50°C . Une pure référence de température a ainsi été trouvée.

Après avoir déterminé la meilleure paire de fibres optiques protégées par une gaine, un cas d'application sur le terrain a été conçu et validé au CERN. Le nouveau capteur utilise une paire de fibres optiques revêtues de polyimide et de désolite, afin de contrôler la température

et l'humidité relative à l'intérieur d'un bloc de béton dès l'origine de son processus de durcissement. La solution proposée représente une percée pour les systèmes de surveillance en génie civil.

Mots clefs : fibre optique, détection, humidité relative, température, détection par fibre distribuée, phase-OTDR, diffusion Rayleigh, gaine primaire, polyimide, acrylate, desolite, silicone, béton.

Contents

Acknowledgements	i
Abstract (English/Français)	iii
List of figures	ix
List of tables	xiii
1 Introduction	1
1.1 CERN and Large Hadron Collider	1
1.2 The Need of Relative Humidity Monitoring	4
2 Fundamentals of Fibre Optic Sensors	7
2.1 Point Fibre Optic Sensors	9
2.1.1 Fibre Bragg Grating	9
2.1.2 Long Period Grating	12
2.2 Distributed Fibre Optic Sensors	15
2.2.1 Rayleigh and Mie Scattering	16
2.2.2 Raman and Brillouin Scattering	28
2.2.3 Distributed Fibre Optic Sensors for RH sensing	35
2.3 Conclusions	37
3 Acrylate- and Polyimide-coated Fibres	39
3.1 A Kilometre-Range Distributed Relative Humidity Sensor	40
3.1.1 Experimental Setup	40
3.1.2 Experimental Results	42
3.1.3 Conclusions	48
3.2 Humidity Effect on Acrylate- and Polyimide-Coated Fibres	48
3.2.1 Experimental Setup	48
3.2.2 Experimental Results	51
3.2.3 Sensitivities Comparison of Polyimide-coated Fibres	59
3.3 Mathematical Model	61
3.3.1 Relative Humidity Model	62
3.3.2 Temperature Model	66
3.4 Conclusions	70

4	Relative Humidity Insensitive Optical Fibre	71
4.1	Desolite-coated Optical Fibres	71
4.1.1	Experimental Setup	71
4.1.2	Experimental Results	73
4.1.3	Conclusions	84
4.2	Desolite-coated Optical Fibre for Temperature Applications	84
4.2.1	Experimental Setup	84
4.2.2	Experimental Results	85
4.2.3	Conclusions	87
4.3	Silicone-Coated Fibres	87
4.3.1	Experimental Setup	87
4.3.2	Experimental Results	88
4.3.3	Conclusions	95
4.4	Conclusions	96
5	Distributed Thermo-hygrometer Fibre Sensor for Concrete Applications	97
5.1	Experimental Setup	99
5.1.1	Setup Preparation	100
5.2	Experimental Results	102
5.2.1	Temperature Analysis	102
5.2.2	Relative Humidity Analysis	106
5.2.3	Three-dimensional General Analysis	110
5.3	Conclusion	113
6	Conclusions and Research Perspectives	115
	Bibliography	119
	List of Acronyms	129
	List of Symbols	131
	List of Publications	133
	Curriculum Vitae	135

List of Figures

1.1	Full diagram and description of the CERN's accelerator complex.	2
1.2	Drawing of LHC machine view from a tunnel access point.	3
1.3	The need of relative humidity monitoring at CERN.	4
2.1	Structure of an optical fibre composed of: core, cladding and coating.	7
2.2	Optical fibre drawing from a preform to a coated optical fibre.	8
2.3	Internal structure of a FBG, its core refractive index modulation and the respective spectral response.	9
2.4	Mechanism of measuring RH with a FBG.	11
2.5	Schematic of the attenuation bands of a LPG sensor.	13
2.6	Comparison between the FBG reflection peak and LPG transmission band. . .	14
2.7	Illustration of a distributed fibre optic sensor.	15
2.8	Differences between Mie and Rayleigh scattering.	16
2.9	Schematic of Rayleigh scattering in optical fibres.	17
2.10	Coordinate geometry for Rayleigh scattering.	19
2.11	Typical response of an I-OTDR.	22
2.12	Comparison between the pulse width and the scattering points.	23
2.13	Scattering mechanisms in the optical fibres.	24
2.14	A typical ϕ -OTDR trace of a 650-metres long standard optical fibre.	24
2.15	Intensity of Rayleigh backscattered traces for the different scanning optical frequencies and respective local spectrum shift at position L_0 [63].	25
2.16	Illustration of OTDR spatial resolution.	26
2.17	Differences between the acoustic-like vibration in the left and the optical-like vibrations in the right.	29
2.18	Energy diagram of Stokes and Anti-Stokes components.	29
2.19	Spectrum of the light spontaneously scattered in optical fibres [70].	30
2.20	Illustration of Brillouin scattering.	32
2.21	Illustration of the Stimulated Brillouin scattering.	34
3.1	Optical fibres coiled in a stress-free configuration inside the climatic chamber.	40

3.2	Full schematic of the ϕ -OTDR setup. VOA - Variable Optical Attenuator; SOA - Semiconductor Optical Amplifier; EDFA - Erbium-Doped Fibre Amplifier; PD - PhotoDetector; OSA - Optical Spectrum Analyser; PG - Pulse Generator; OSC - Oscilloscope.	41
3.3	Comparison between the electronic temperature reference, in orange, and the bare fibre signal, in blue.	42
3.4	Climatic chamber conditions during the RH test at constant temperature. . . .	43
3.5	Full ϕ -OTDR frequency shift of the FUT during the RH test at constant temperature.	43
3.6	Comparison of polyimide-coated fibres responses during the RH test at constant temperature.	44
3.7	RH calibrations of polyimide-coated fibres.	45
3.8	Acrylate-coated fibres response during the RH test at constant temperature. . .	46
3.9	RH calibration of the acrylate-coated fibre.	46
3.10	Frequency shift of the 10 kilometres fibre spliced with 100 metres of polyimide-coated fibre.	47
3.11	Zoom of the last part of the frequency shift plot after 10 kilometres.	47
3.12	Photos of climatic chamber and pneumatic circuit.	49
3.13	Schematic of the climatic chamber including the pneumatic circuit and the electronic data acquisition system. MFC - Mass Flow Controller.	49
3.14	Schematic of a CP- ϕ -OTDR interrogator [65]. ECL - External Cavity Laser. SG - Signal Generator. SOA - Semiconductor Optical Amplifier. EDFA - Erbium-Doped Fibre Amplifier. BPF - Band Pass Filters. VOA - Variable Optical Attenuator. PD - PhotoDetector.	50
3.15	Optical fibres rolled in the strain-free holders.	51
3.16	Climatic chamber conditions during the temperature test at constant RH. . . .	52
3.17	Frequency shift of all fibres during the temperature test at constant RH.	52
3.18	Temperature calibration fittings of all fibres.	53
3.19	Example of the temperature compensation method. The fibre total frequency shift is plotted in orange, the reference bare fibre in blue and the compensated trace in black. The temperature reference is plotted in purple.	54
3.20	Climatic chamber conditions during the RH test at 25°C.	55
3.21	Fibres frequency shift during a RH test at 25°C.	55
3.22	RH calibration fittings of all fibres at 25°C.	56
3.23	RH Sensitivity at different temperatures of the acrylate- and polyimide-coated fibres.	57
3.24	Comparison between the temperature sensitivities in air and CO ₂	58
3.25	Comparison between the RH sensitivities in air and CO ₂	58
3.26	Temperature sensitivity of polyimide-coated fibres as function of the number of layers.	59
3.27	Comparison between the RH sensitivities of all polyimide-coated fibres. . . .	60
3.28	RH and temperature in the climatic chamber during the test.	63

3.29 Comparison between the experimental data of polyimide-coated fibre with 1 layer of coating and the range of theoretical expected data.	64
3.30 Comparison between the RH experimental data of 2 layers of polyimide and the theoretical expected data.	65
3.31 Comparison between the experimental data of 3 layers of polyimide and the theoretical expected data.	65
3.32 Comparison between the experimental data of 4 layers of polyimide and the theoretical expected data.	66
3.33 Temperature in the climatic chamber during the test.	67
3.34 Comparison between the temperature experimental data and the range of theoretical expected data	67
3.35 Comparison between the theoretical model and the experimental data of the fibre with 2 layers of polyimide coating.	68
3.36 Comparison between the theoretical model and the experimental data of the fibre with 3 layers of polyimide coating.	69
3.37 Comparison between the theoretical model and the experimental data of the fibre with 4 layers of polyimide coating.	69
4.1 Micrograph of a DeSolite-coated fibre and stress-free fibre holders.	72
4.2 Climatic chamber conditions during the temperature characterization test. Temperature in blue and RH in orange.	73
4.3 Grouped plot of all fibres frequency shift during the temperature characterization test.	74
4.4 Temperature calibrations plot of all fibres.	74
4.5 Variation of the temperature sensitivity, S_T , with the coating diameter.	75
4.6 Climatic chamber conditions during the RH characterization test. Temperature in blue and RH in orange.	76
4.7 Grouped plot of the frequency shifts of all fibres during the RH characterization test.	76
4.8 Grouped plot of the frequency shift of all desolite-coated fibres together with the bare fibre.	77
4.9 RH calibration of 5 desolite-coated fibres.	78
4.10 Climatic chamber conditions during the RH at 50°C.	78
4.11 Grouped plot of all fibres frequency shift during the RH test at 50°C.	79
4.12 Grouped plot of desolite-coated fibres frequency shift during the RH test at 50°C.	79
4.13 Example of minimum and maximum RH sensitivity.	80
4.14 Grouped plot of all fibre frequency shifts at different temperatures. A) Frequency shift at 15°C. B) RH calibrations a 15°C. C) Frequency shift at 0°C. D) RH calibrations a 0°C. E) Frequency shift at -10°C. F) RH calibrations a -10°C. G) Frequency shift at -20°C. H) RH calibrations a -20°C.	81
4.15 Response of fibre A and E1 in a RH test at 15°C.	82
4.16 Climatic chamber conditions in the 4-step RH test at 25°C.	83

4.17	Grouped plot of all desolite-coated fibres during the 4-step RH test at 25°C. . . .	83
4.18	Frequency shift of all fibres grouped during the temperature characterization test. . . .	85
4.19	Temperature calibration curves of all the FUT.	85
4.20	Silicone-coated fibres micrograph.	88
4.21	Silicone-coated fibres in a stress-free holder.	88
4.22	Climatic chamber conditions during the 3-step temperature characterization. . . .	89
4.23	Silicone-coated fibres compared with bare fibre in the temperature test.	89
4.24	Climatic chamber conditions during RH test at 25°C.	90
4.25	Silicone-coated fibres compared with bare fibre in the RH test at 25°C.	90
4.26	Silicone-coated fibre sample compared with bare fibre in the RH test at 25°C. . .	91
4.27	Climatic chamber conditions during the RH test at 0°C.	91
4.28	Frequency shifts of all fibres during the RH test at 0°C	92
4.29	Silicone-coated fibres compared with bare fibre in the RH test.	92
4.30	Climatic chamber conditions during the RH test at -20°C.	93
4.31	Silicone-coated fibres compared with bare fibre in the RH test at -20°C.	93
4.32	Silicone-coated fibres compared with bare fibre in the RH test at -20°C.	94
4.33	Climatic chamber conditions during the RH at 55°C.	94
4.34	Silicone-coated fibres compared with bare fibre in the RH test at 55°C.	95
4.35	Silicone-coated fibres compared with bare fibre in the RH test at 55°C.	95
5.1	Permeable silicone wrap tube in which the selected optical fibres were inserted. . .	100
5.2	Full schematic of experimental setup.	101
5.3	Wood formwork before and after pouring concrete, and concrete block after a few days of curing.	101
5.4	Reference temperature measured by PT100 during the 37 days of testing.	102
5.5	Fibre distribution in a spiral configuration.	103
5.6	Temperature measured by the desolite-coated fibres at the base of the block. . .	103
5.7	Temperature measured by the desolite-coated fibres in the middle of the block. .	104
5.8	Temperature measured by the desolite-coated fibres on the top of the block. . .	104
5.9	Imperfections in the concrete structure.	105
5.10	Comparison between the electronic reference and one fibre's measurement. . .	106
5.11	Reference RH measured by HIH4000.	106
5.12	RH measured by the polyimide-coated fibres on the base of the block.	107
5.13	RH measured by the polyimide-coated fibres in the middle of the block.	108
5.14	RH measured by the polyimide-coated fibres on the top of the block.	108
5.15	Comparison between the electronic reference and one fibre measurement in the middle of the block.	109
5.16	Response of the polyimide-coated fibres after adding water at the top of the block. .	110
5.17	Temperature and RH measurements after 1 hour of curing.	111
5.18	Temperature and RH measurements after 12 hours of curing.	111
5.19	Temperature and RH measurements after 2 days of curing.	112
5.20	Temperature and RH view measurements 37 days of curing.	112

List of Tables

3.1	List of FUT and respective coating characteristics and lengths.	41
3.2	RH sensitivities comparison with the respective standard errors and R^2	45
3.3	List of FUT and respective coating characteristics and lengths.	51
3.4	Temperature sensitivities comparison.	53
3.5	RH sensitivities of acrylate-coated fibres at different temperatures.	56
3.6	RH sensitivities of polyimide-coated fibre at different temperatures.	56
3.7	Temperature and RH sensitivities under pure CO ₂ atmosphere.	58
3.8	Physical parameters of polyimide and silica optical fibres.	62
3.9	Range of parameters values for polyimide-coated optical fibres.	62
3.10	Best parameters for modelling the polyimide-coated fibres.	63
3.11	Polyimide parameters for temperature modelling.	67
3.12	Temperature expansion coefficients for modelling.	68
4.1	List of FUT with their respective coating and core characteristics.	72
4.2	List of FUT with respective thicknesses and temperature sensitivities.	75
4.3	RH Sensitivities of all fibres in MHz/%RH.	82
4.4	List of FUT with their respective coating and core characteristics.	84
4.5	Comparison between the temperature sensitivities.	86
4.6	Temperature sensitivities comparison and respective measurement resolution.	87

1 Introduction

1.1 CERN and Large Hadron Collider

CERN, the European Organization for Nuclear Research, is one of the world's largest centres for scientific research and its objective is to help uncover and understand the fundamental structure of the universe and how it works [1]. CERN convention was signed in 1953 by 12 founding states ^I and established in 1954 [2]. Since CERN began, fundamental physics has been the core subject of research. CERN is based in a northwest suburb of Geneva on the Franco-Swiss border and derived from the name *Conseil européen pour la recherche nucléaire*. Today, CERN has 23 member states ^{II} while additional nations from around the globe also participate in the scientific program ^{III}.

CERN unites scientists from around the world in the pursuit of knowledge and hosts the world's largest and most complex scientific instrument ever made, composed of several purpose-built particle accelerators and detectors. The results obtained give the physicists clues to understand nature's laws and how the Universe works. The accelerator complex at CERN, schematized in Figure 1.1, is a succession of devices that accelerate particles to increasingly higher energies.

^IBelgium, Denmark, France, the Federal Republic of Germany, Greece, Italy, the Netherlands, Norway, Sweden, Switzerland, the United Kingdom, and Yugoslavia.

^{II}Austria, Belgium, Bulgaria, Czech Republic, Denmark, Finland, France, Germany, Greece, Hungary, Israel, Italy, Netherlands, Norway, Poland, Portugal, Romania, Serbia, Slovak Republic, Spain, Sweden, Switzerland and United Kingdom.

^{III}Cyprus, Estonia and Slovenia are the Associate Member States in the pre-stage to Membership. Croatia, India, Lithuania, Pakistan, Turkey and Ukraine are the Associate Member States. Japan, the Russian Federation and the United States of America, as well as the European Union, JINR and UNESCO currently have Observer status. Non-Member States with co-operation agreements with CERN include Albania, Algeria, Argentina, Armenia, Australia, Azerbaijan, Bangladesh, Belarus, Bolivia, Brazil, Canada, Chile, China, Colombia, Costa Rica, Ecuador, Egypt, Estonia, North Macedonia, Georgia, Iceland, Iran, Jordan, Korea, Malta, Mexico, Mongolia, Montenegro, Morocco, New Zealand, Peru, Saudi Arabia, South Africa, United Arab Emirates and Vietnam. CERN also has scientific contacts with Cuba, Ghana, Ireland, Latvia, Lebanon, Madagascar, Malaysia, Mozambique, Palestinian Authority, Philippines, Qatar, Rwanda, Singapore, Sri Lanka, Taiwan, Thailand, Tunisia, Uzbekistan.

CERN's Accelerator Complex

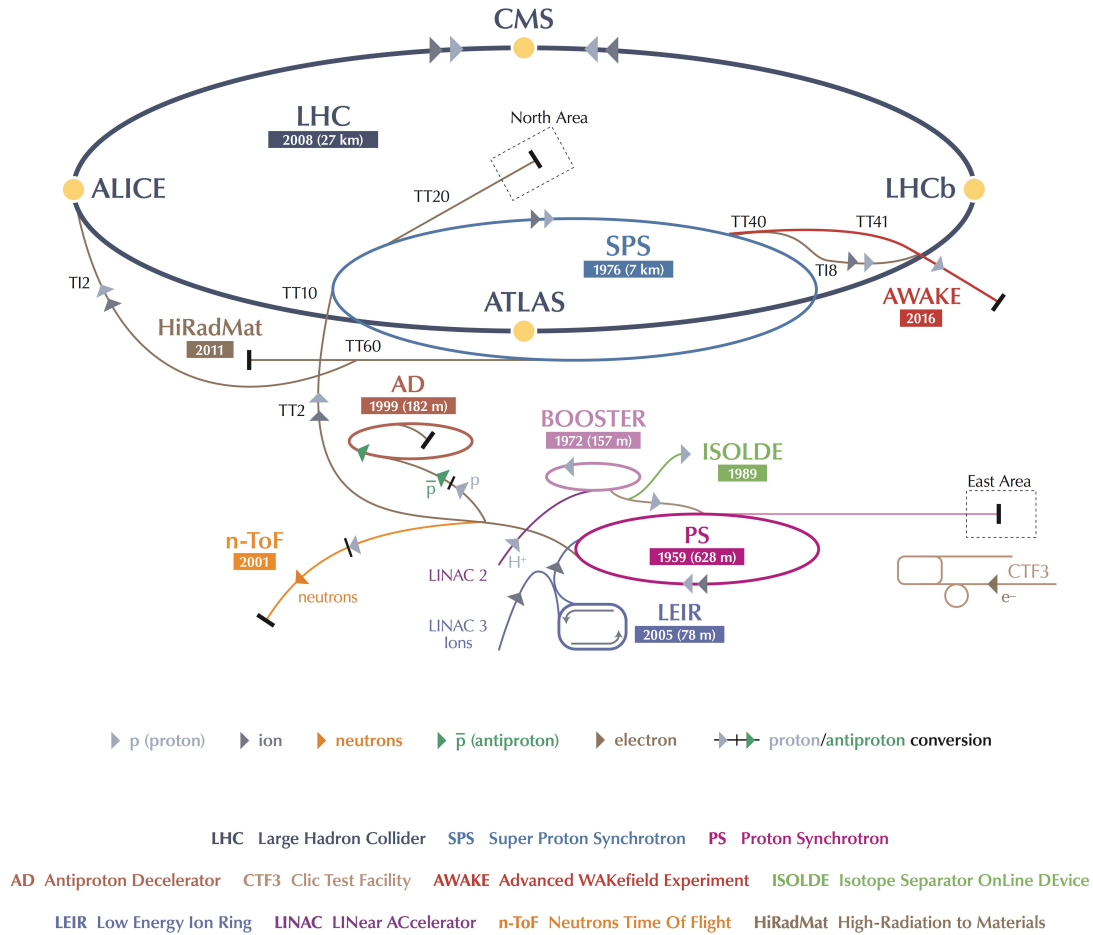


Figure 1.1 – Full diagram and description of the CERN's accelerator complex.

The cycle starts with a bottle of hydrogen gas in which an electric field is applied to strip electrons of hydrogen atoms to yield protons. This way, the protons are separated and can be injected into the cycle. The first accelerator in the chain is the Linear Accelerator 2 (LINAC 2), which accelerates the protons to the energy of 50 MeV^{IV}, followed by the Proton Synchrotron Booster (PSB), from which the protons get out with 1.4 GeV of energy. The next accelerator of the chain is the Proton Synchrotron (PS), where the proton beam is pushed to 25 GeV, before the Super Proton Synchrotron (SPS), where the beam reaches 450 GeV of energy. The protons are finally ready to be transferred to the Large Hadron Collider (LHC) that is divided into two beam pipes, one circulating clockwise and the other counterclockwise^V.

^{IV}Electron volt (eV) is a unit of energy used in atomic and nuclear physics that represents the energy needed to move an electron across a potential difference of one volt. $1 \text{ eV} = 1.602 \times 10^{-19} \text{ joule}$.

^VProtons are not the only particles accelerated in the LHC. Lead ions for the LHC start from a source of vaporised lead and enter LINAC 3 before being collected and accelerated in the Low Energy Ion Ring (LEIR). They then follow the same route to maximum energy as the protons.

The LHC is the current flagship of CERN and is housed in a 27 kilometre circumference tunnel located between 45 and 170 metres underground. It crosses the France-Switzerland border and Figure 1.2 shows the view from one of the tunnel access points. It takes 4 minutes and 20 seconds to fill each LHC ring, and 20 minutes for the protons to reach their maximum energy of 6.5 TeV. Afterwards, the two beams are brought into collision inside the four main detectors (ALICE, ATLAS, CMS, and LHCb), where the total energy is 13 TeV. Most of the other accelerators in the chain, which are controlled by operators 24 hours a day from the CERN Control Centre, have also their experimental halls where beams are used for experiments at lower energies.

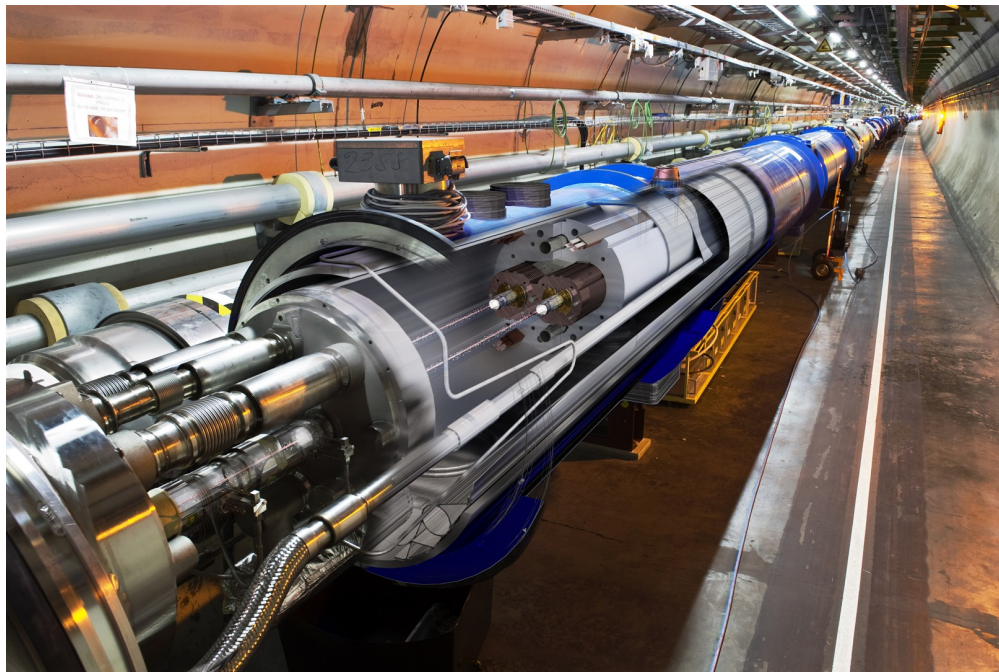


Figure 1.2 – Drawing of LHC machine view from a tunnel access point.

LHC is the world's most powerful particle accelerator and it started up in September 2008. Particles are guided around the accelerator by a strong magnetic field imposed by a ring of super-conduction magnets^{VI}. Special electric cables that operate in a super-conduction state are used to keep the electricity conduction efficient, without resistance or significant loss of energy. This requires an extremely low temperature of -271.3°C , turning LHC into one of the the coldest place on Earth.

^{VI}Thousands of magnets of different varieties and sizes are used to direct the beams around the accelerator. These include 1232 dipole magnets of 15 metres in length that bend the beams, and 392 quadrupoles magnets, each 5–7 metres long, which focus the beams. Just before the collision, another type of magnet is used to "squeeze" the particles closer together to increase the chances of collisions.

1.2 The Need of Relative Humidity Monitoring

Silicon detectors are widely used in particle physics experiments mostly for tracking the position of charged particles. Those operating at LHC detectors are subject to high radiation levels, which can rapidly downgrade their performance unless they are constantly kept at low temperatures, typically -10°C , with local peaks at -20°C [3, 4]. The cooldown process increases their lifetime and reduces the losses, mostly caused by noise and heating. At these temperatures, the relative humidity (RH) inside the detector enclosure should be strictly controlled, typically below 5% RH [5], in order to avoid any risk of condensation, potentially damaging the associated complex electronics. Figure 1.3 summarizes the need of RH monitoring at LHC.

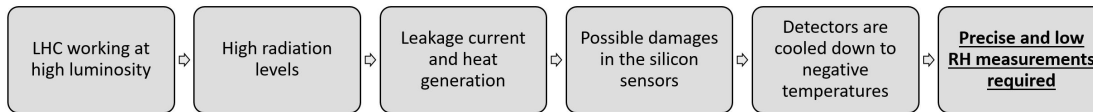


Figure 1.3 – The need of relative humidity monitoring at CERN.

The requirements for any environmental sensor to be installed at LHC detectors should fulfil the requirements of being radiation-resistant (doses up to MGy^{VII}) and insensitive to magnetic fields (up to 4 Tesla^{VIII}) while having small dimensions, in the order of a few millimetres. They must be able to multiplex to form large networks of hundreds of sensors and allow reliable readings over more than 100 metres, which is the typical distance between the detection points and the acquisition modules placed in the control room. Finally, they must have a reduced number of wires and allow remote calibration with long-term stability, due to the lack of accessibility that can last for a few years.

Nowadays, a large offer of miniaturized RH electronic sensors is available in the market [6], and a complete review of the RH electronic sensors implemented at CERN, including their advantages and disadvantages, was made by G. Berruti et al [7]. Notwithstanding the fact that the available RH electronic sensors fill some of the previous requirements, they fail especially when employed in harsh environments and in volumes with an intense electromagnetic field.

However, CERN is also a highly complex piece of civil engineering consisting of 83 kilometres of underground structures such as tunnels, shafts, caverns and alcoves. The long-term safety and structural health of those underground areas are critical to ensure the correct operation of the experiments. Therefore, the need for remote monitoring solutions increases, especially for measuring strain, temperature and humidity. Additionally, given that the accurate position of faults in large structures is difficult to determine, a monitoring solution with a high level of multiplexing significantly improves this accuracy. Finally, temperature and humidity are also key parameters for the concrete curing process, abundantly used in these structures. Monitoring both measurands within the concrete from the first day of curing provides useful

^{VII}One gray (Gy) is the International System of Units equivalent of 100 rads, which is equal to an absorbed dose of 1 Joule/kilogram.

^{VIII}Tesla is a derived unit of the magnetic field strength in the International System of Units.

and real time information about the quality of the structure, which can either speed up the waiting times if curing is complete, or delay them if more time is needed.

Considering both scenarios, the radiation environments and the structural health monitoring at large scales, Fibre Optics Sensors (FOS) have been identified as very good candidates, in particular for their good withstanding under strong radiation environments [8] but also for their high multiplexing capability and large sensing range. FOS take advantage of the extremely low transmission loss (0.2 dB/km) of an optical fibre cable and use it as the sensing element or as a means of transmitting signals from a remote sensor to the respective electronics processing unit. FOS technology can be divided into two main categories. The first is made of point FOS, such as Fibre Bragg Gratings (FBG) and Long Period Gratings (LPG), while the second is based on Distributed Fibre Optic Sensors (DFOS), in which the whole fibre makes a continuous sensor.

DFOS is a cost-effective technique that provides thousands of sensing points using a single interrogation unit and a single optical fibre cable. Three different types of DFOS can be identified, based on the exploited backscattering effect: Rayleigh and Brillouin, where the backscattered signal inside the material is directly dependent on the temperature and stress applied on the fibre; and Raman, where the backscattered signal only depends on the temperature [9]. Besides temperature and stress, relative humidity is other environmental parameter influencing the signal in the fibre: the fibre coating expands/contracts when absorbing/desorbing water vapour, transferring stress to the fibre.

The objective of this dissertation is the development of a relative humidity distributed fibre optic sensor, based on Rayleigh scattering, for long-distance applications using phase-sensitive optical time-domain reflectometry technique (ϕ -OTDR), which is a technique that is gaining the attention of industry and academy due to its ultra-high sensitivity.

The dissertation is structured as follows:

Chapter 2 gives a general overview of the FOS technology fundamentals, in particular FBGs, LPGs, and DFOS. The relevant state-of-the-art studies are presented, as well as the main features and limitations of the CERN technologies for RH monitoring. In addition, the working principles of different DFOS interrogation techniques are presented, particularly the ϕ -OTDR technique.

Chapter 3 presents the first proof of concept of a relative humidity distributed fibre optic sensor. The responses to humidity variations of different acrylate- and polyimide-coated optical fibres were compared and fully investigated at different temperatures. The experimental results of the polyimide-coated fibres were validated with a theoretical model.

Chapter 4 summarizes the behaviour of two new kinds of coated optical fibres, with acrylate and silicone coatings respectively, specially designed for mitigating the cross-sensitivities issue between temperature and relative humidity. Several fibres samples with different coating

thicknesses were produced in order to find the best suitable fibre to be the temperature reference in the thermo-hygrometer sensor.

Chapter 5 presents an application case where the developed distributed thermo-hygrometer sensor was installed, tested and validated. The developed ϕ -OTDR interrogator, which makes use of a pair of coated optical fibres, monitored temperature and RH simultaneously inside a concrete block from the very first moment of its curing process.

Chapter 6 summarizes the main results, the general conclusions and future perspectives for this research work.

2 Fundamentals of Fibre Optic Sensors

Since their discovery in 1966 by Charles K. Kao, optical fibres have had a huge impact on our society, not only in the world of telecommunications but also in sensing applications [10, 11]. Optical fibres have unique characteristics in terms of transmission losses and are considered the waveguides of the present and future: they are low cost, small in size, light in weight and not affected by electromagnetic radiation due to their dielectric silica-based (SiO_2) composition [12]. Most of the optical fibres are composed of a core, a cladding, and a coating, as seen in Figure 2.1, and light is trapped inside the core and guided through its length due to the difference in the refractive index between core and cladding. The outer surface of an uncoated optical fibre when exposed to air, moisture or other hazards, may have flaws in the glass surface. Initially, such defects may be microscopic but, over time, they can become larger cracks that affect the good condition of the optical fibre. Therefore, coatings play a key role in protecting the fibre from the atmospheric environment, but they also absorb any light that is not properly directed.

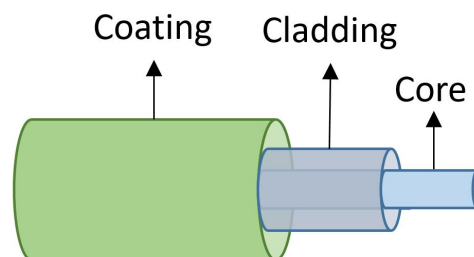


Figure 2.1 – Structure of an optical fibre composed of: core, cladding and coating.

The most conventional telecommunications optical fibres are known as single-mode fibres (SMF) and have a core diameter between 8 and 10.5 μm and a cladding diameter of 125 μm . Coatings are usually composed of 2 layers of acrylate [13]. The inner coating layer, with a diameter around 180 μm , is a soft polymer that alleviates the effects of micro-bending on the optical fibre, while the outer layer, with 250 μm of diameter, is a hard shell polymer that protects the optical fibre from the external environment including, in principle, the

humidity [14]. More recently, depending on the application environment where the fibre is installed, different materials such as polyimide, carbon or composite structures are used as optical fibre coatings [15]. In harsher environments, the optical fibres are further protected with additional layers of coating made of materials as aluminium or strong plastic polymers.

The manufacturing process of a standard silica-based SMF starts from a fibre preform, which is a cylindrical piece of optical glass that exhibits the same refractive index profile and core/cladding ratio as the targeted SMF. The preform is heated in a furnace that softens the glass until it starts to elongate. The diameter of the resulting thin fibre is tightly controlled by a diameter gauge before applying the thermo-cured coating. The fibre drawing process is explained in Figure 2.2.

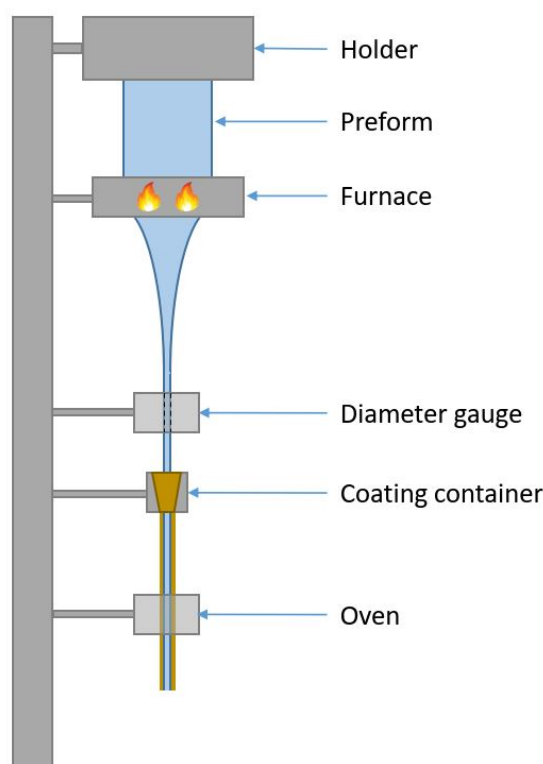


Figure 2.2 – Optical fibre drawing from a preform to a coated optical fibre.

The recent progresses in the field of optical fibres motivated the rapid growth of Fibre Optic Sensors (FOS) that can now be found in a large number of industrial applications [16, 17, 18, 19]. To name few examples: monitoring bridges, structures, pipelines, or railways. But the technology continues to progress and even more examples of applications can be explored [20, 21, 22].

A FOS encodes the physical quantities in one or more properties of an optical signal such as optical power, phase, state of polarization, or wavelength. The measurands will change the way the light is transmitted in the optical fibre in such a manner that these properties

will not be the same at the fibre input and output [23]. FOS can be divided into two groups: extrinsic, where the optical fibre only guides the signal from an external sensor to an electronic processing unit; and intrinsic, in which the optical fibre contains the sensing element or is the sensing element itself. The intrinsic class of FOS can be further divided into two different categories. The first is made of point FOS such as FBG and LPG, which can only sense at a specific position along with the optical fibre, while the second is based on DFOS, in which the whole fibre makes a continuous sensor.

2.1 Point Fibre Optic Sensors

2.1.1 Fibre Bragg Grating

A FBG is a reflective structure that results from a photo-induced periodic perturbation of the refractive index in the core of a SMF [24]. This physical perturbation acts as a wavelength-selective filter, reflecting part of the input signal at a certain wavelength, called Bragg Wavelength (λ_B), as represented in Figure 2.3.

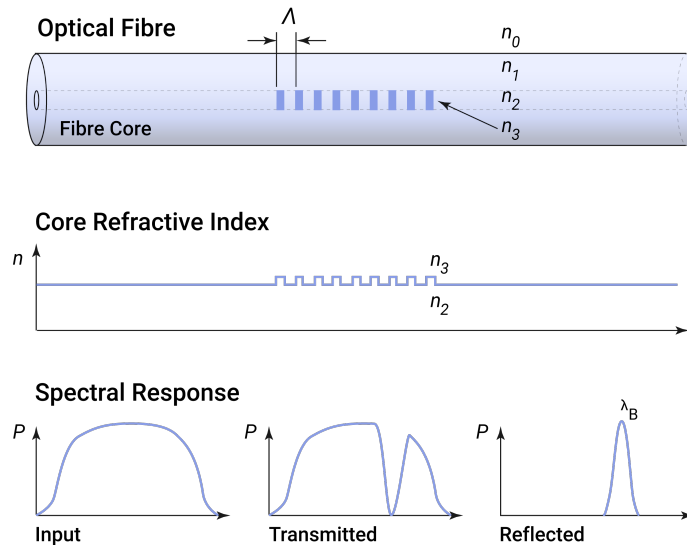


Figure 2.3 – Internal structure of a FBG, its core refractive index modulation and the respective spectral response.

A FBG, which typically has between 5 and 7 mm of grating length with a period around 500 nm [25], performs a direct transformation of the sensed parameter into optical wavelength and is not affected either by possible connector losses nor by the optical power level. Their narrowband operation makes them ideal for multiplexing applications because several FBGs at different wavelengths can be inscribed in the same optical fibre. Bragg's law, given by

Equation 2.1, shows that λ_B is dependent on the fibre effective refractive index (n_0) and the pitch of the grating (Λ) [26].

$$\lambda_B = 2n_0\Lambda \quad (2.1)$$

The refractive index and the grating pitch are directly dependent on the temperature and applied strain and a variation of both parameters causes a shift in the Bragg wavelength. Strain induces a change in the gratings spatial pitch and in the effective refractive index due to the elastic behaviour and elasto-optic effect, respectively. Temperature has a similar effect induced by the thermal expansion and the thermo-optic effect [27]. The influence of temperature and strain on the FBG wavelength can be calculated by the Taylor series expansion of the Bragg expression [28]. The general expression for the Bragg wavelength shift is given by Equation 2.2.

$$\frac{\Delta\lambda_B}{\lambda_B} = \varepsilon_z - \frac{n_0^2}{2} (\varepsilon_z p_{12} + \varepsilon_r (p_{11} + p_{12})) + \xi \Delta T \quad (2.2)$$

where ε_z and ε_r the axial and radial strains. The second component represents the strain-optic effect, where p_{11} and p_{12} are the principal components of the strain-optic tensor. The third component represents the thermo-optic effect, where ξ is the thermo-optic coefficient.

The simplified version of the Equation 2.2 for a FBG grating written in the single-mode optical fibre subjected only to axial strain is given by [29]:

$$\frac{\Delta\lambda_B}{\lambda_B} = (1 - P_e) \varepsilon_z + [(1 - P_e) \alpha + \xi] \Delta T \quad (2.3)$$

where α is the thermal-expansion coefficient. $P_e = p_{12} - (p_{11} + p_{12})$ represents the effective strain-optic coefficient, where ν is the Poisson's ratio.

Nowadays, FBG-based sensors are used in a wide number of applications, among different fields such as health and biomedical devices, maritime, civil and aerospace engineering, radioactive environments, and many others [30, 31]. At CERN, several FBGs for temperature and strain measurements were already installed and are currently working at one of the LHC detectors, the Compact Muon Solenoid (CMS) [32].

FBG for RH sensing

A bare FBG, i.e., without any coating, is insensitive to relative humidity due to the hydrophobic property of bare silica optical fibres. To turn a FBG into a RH sensor, the grating should be coated by a hygroscopic material, such as polyimide for example, whose volume changes in the presence of humidity. Figure 2.4 exemplifies the mechanism of measuring RH with a FBG. Changes in the volume, due to absorption/desorption of water, will induce a secondary mechanical strain into the grating, varying the Bragg wavelength.

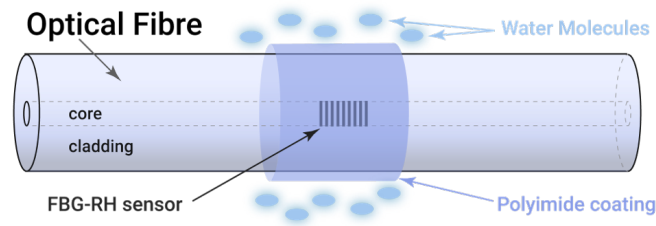


Figure 2.4 – Mechanism of measuring RH with a FBG.

Under these conditions, a FBG is sensitive to temperature, strain, and relative humidity but, if the FBG is installed in a strain-free package, the axial strain that causes Bragg wavelength shift will only be dependent on 2 components: RH-induced strain and temperature-induced strain. The updated Bragg shift equation (Equation 2.4) can be expressed as:

$$\frac{\Delta\lambda_B}{\lambda_B} = (1 - P_e) \varepsilon_{RH} + (1 - P_e) \varepsilon_T + \xi \Delta T \quad (2.4)$$

where ε_{RH} and ε_T are the strain induced on the optical fibre by the coating swelling and thermal expansion of the materials, respectively.

The influence of humidity and temperature on coated FBGs was firstly studied by Giaccari et al. [33] and, afterwards, by Kronenberg et al., who concluded that the response of a polymer-coated FBG is a linear superposition of RH and temperature effects [34]:

$$\frac{\Delta\lambda_B}{\lambda_B} = S_T \Delta T + S_{RH} \Delta RH \quad (2.5)$$

where S_{RH} and S_T are the RH and temperature sensitivities respectively. One should take into consideration that there is a temperature-RH cross-sensitivity so that any RH-FBG in-

stalled in real sensing applications should have a precise temperature compensation technique to isolate both variables.

$$S_{RH} = \left. \frac{\partial \lambda_B}{\partial RH} \right|_{\text{constant } T} \quad (2.6)$$

$$S_T = \left. \frac{\partial \lambda_B}{\partial T} \right|_{\text{constant } RH} \quad (2.7)$$

Based on this technology, few years later, G. Berruti et al. developed the first CERN generation of RH-FOS with polyimide coating [35]. For the first time, the authors fully investigated the effects of radiation and the behaviour of those RH-FBGs in low levels of RH (0 to 10%) at temperatures below 0°C. This study demonstrated that the polyimide-coated FBGs can work correctly under high radiation environments if performing a pre-irradiation campaign that saturates the cross-sensitivity due to radiation. This way, the RH-FBG is practically radiation insensitive. At the same time, it was also demonstrated that the developed RH-FBGs work correctly at low levels of RH and temperature. The project ended with the installation, in the CMS experiment, of 72 optic fibre-based thermo-hygrometers, each one formed by a FBG temperature sensor and one FBG relative humidity sensor [36].

Despite the success of the FBGs installation at CMS and their good performances, the first generation of RH-FOS developed at CERN presented some limitations. First of all, the RH sensitivity of a polyimide-coated FBG is in the order of a few pm/%RH [35], which is in the same order of magnitude of the optical interrogators resolution [37]. This means that the minimum resolution of a coated FBG for RH measurements can not be lower than 2%, which is comparable with the traditional electronic RH sensors resolution, between 2 and 4% [38]. For specific applications where RH should be precisely monitored and kept constant at extremely low levels, the FBGs resolution level is not enough and a more accurate measurement method is required. At the same time, RH-FBGs are significantly more sensitive to temperature than to RH (10 times more) and a small variation of temperature can induce a large error in the RH measurement if it is not correctly compensated. Based on these limitations, T. Venugopalan et al. proposed a new technology based on coated-LPGs, in particular targeting very high sensitivity in the low humidity range (RH<10%) [39].

2.1.2 Long Period Grating

A LPG is a photonic device based on a periodic modulation of the refractive index of the optical fibre's core. The grating period is between 100 and 500 μm with a length of 2 to 3 cm. The combination of these two parameters promotes a power transfer from the fundamental guided core mode to a discrete number of forward propagating cladding modes [40].

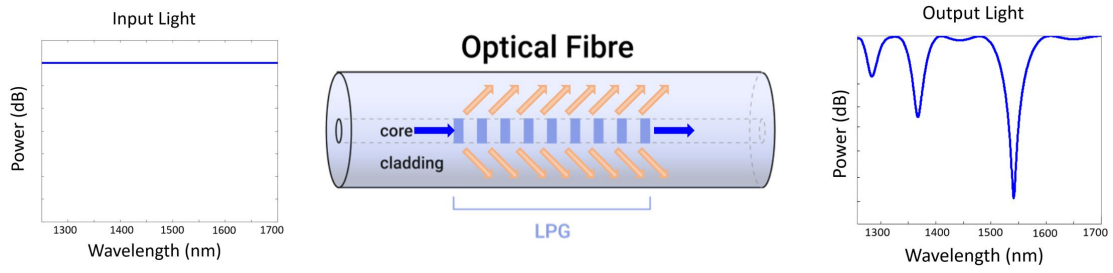


Figure 2.5 – Schematic of the attenuation bands of a LPG sensor.

The spectrum shape and the central wavelength are sensitive to the LPG period (Λ), length and to local environmental conditions such as temperature, strain, bend radius, and refractive index of the surrounding medium. The fact that a portion of the electromagnetic field present in the cladding modes is released to the environment makes the LPG technology more sensitive to the external environment than FBGs [41, 42]. The high attenuation of the cladding modes results in the transmission spectrum of the fibre that contains a series of attenuation bands centred at discrete wavelengths, as seen in Figure 2.5.

The coupling between the propagating modes happens at a specific wavelength and it is given by Equation 2.8 [43].

$$\lambda_{\text{res},i} = \left(n_{0,\text{co}} - n_{0,\text{cl}}^i \right) \Lambda \quad (2.8)$$

where $n_{0,\text{co}}$ and $n_{0,\text{cl}}^i$ are the effective refractive indexes of the core and of the i^{th} cladding mode, respectively.

LPG for RH sensing

As with the coated-FBG technology, in order to have a RH sensor based on a LPG, an appropriate hygroscopic material should be applied as coating. In this case, as one of the main features of a LPG is its sensitivity to the surrounding refractive index [44], the coating does not need to induce strain into the fibre's core, as RH-FBG does, but to change the refractive index in the presence of water molecules. The choice of a coating with a refractive index greater than of silica increases the effective refractive index of the cladding, changing the way the light is propagated and increasing the LPG sensitivity. If the coating changes its refractive index with a RH variation, the coated-LPG is able to measure RH.

In 2008, T. Venugopalan et al. proposed, for the first time, a LPG coated with PolyVinyl Alcohol (PVA) for RH monitoring applications [39]. The obtained results showed a high but non-linear RH sensitivity, especially in the range between 75 and 97%, and the authors suggested the use of this technology in industrial applications for RH monitoring.

More recently, several kinds of materials have been tested as a coating of a LPG-based RH sensors, most of them using polymers or gels that change their thicknesses in the presence of water molecules. M. Consales et al. summarized the kinds of material used in the literature and proposed, for the first time, a titanium dioxide (TiO_2) coating due to its high refractive index ($n = 1.96$) and hygrosensitive characteristics. These sensors were, therefore, proposed as the second generation of RH-FOS developed at CERN [45]. At that moment, there was no evidence in literature of any characterization of coated-LPGs at low levels of RH (below 20%) neither at temperatures lower than 15°C . The developed LPGs presented an extremely high RH sensitivity, which is 3 order of magnitude higher than the RH-FBGs in the same low RH conditions. In addition, the use of a metallic coating avoids the typical ageing problems of polymeric coatings, expected on the polyimide-coated FBGs. The novel TiO_2 -coated LPGs were submitted to an irradiation campaign and their RH sensitivities were not significantly affected [46, 47].

Generally speaking, RH-FOS based on gratings are only sensitive in the locations where the gratings are inscribed and they have an intrinsic limitation in terms of multiplexing, specially the LPGs. The LPG spectrum is significantly broader than the FBG reflection peak, as seen in Figure 2.6, and this is a limitation due to the spectral range of the optical interrogator typically used for fibre gratings.

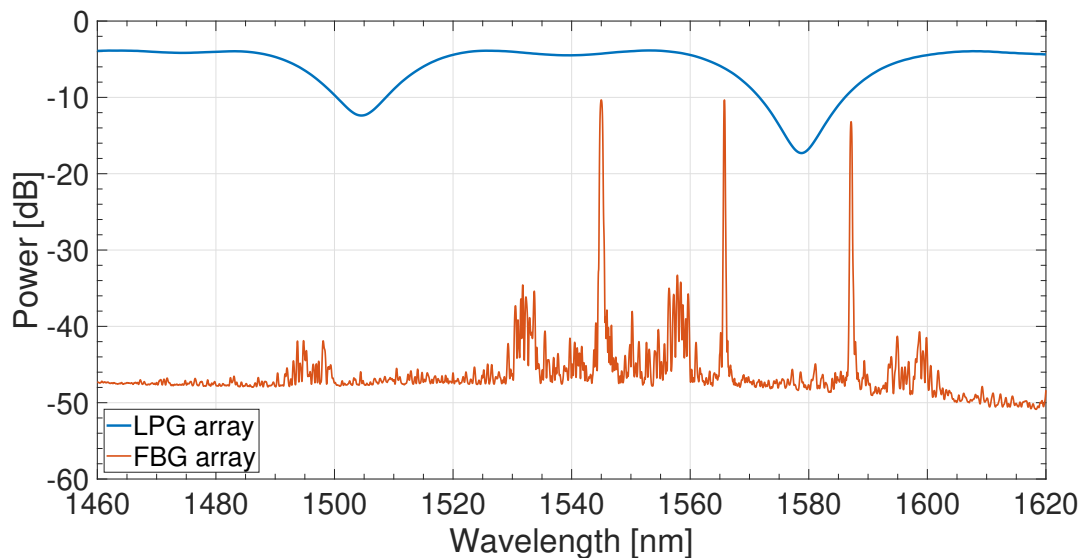


Figure 2.6 – Comparison between the FBG reflection peak and LPG transmission band.

Only few LPGs fit in the interrogators wavelength range, and building a multiplexed LPG system is an impossible task without a complex system based on an optical switch[48]. Additionally, the package is still in prototype stage. These limitations can be easily overcome with the distributed fibre sensors technology.

2.2 Distributed Fibre Optic Sensors

DFOS technology, illustrated in Figure 2.7, is employed in a large range of applications mostly for measuring temperature, strain, pressure, or vibration, and their use has significantly increased over the last years, mostly due to the possibility of having precise local information in real-time over a large sensing range [49]. These systems provide a cost-effective alternative to complex arrays of point FOS because the sensing range can be extended to hundreds of kilometres with a spatial resolution that can vary from few millimetres to some metres, using only a single interrogation unit with a single optical fibre [50].

The theoretical fundamentals of distributed fibre optic sensors are based on the light scattering phenomena, which is affected by changes applied in the optical fibre, typically temperature and strain. Such physical properties will be encoded in the scattered light, which carries them up to detection where it is processed to be spatially resolved.

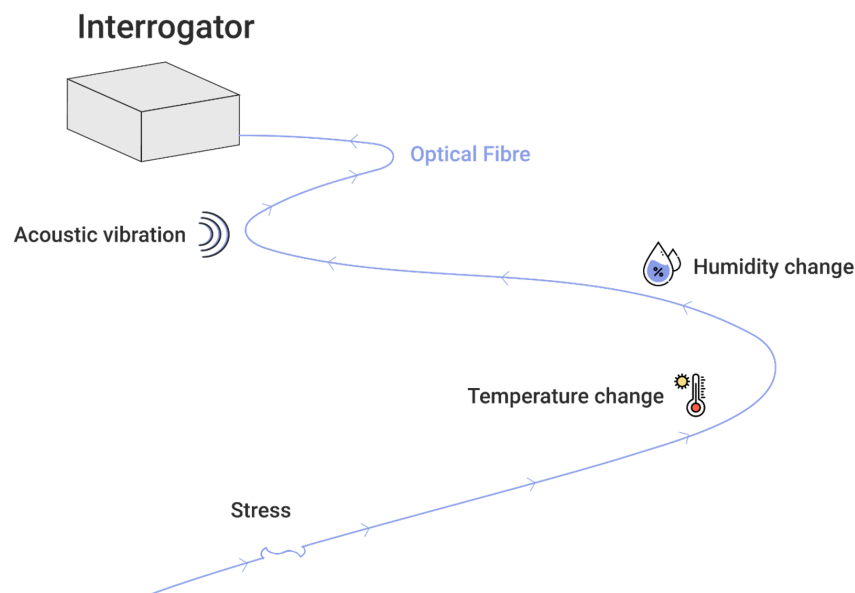


Figure 2.7 – Illustration of a distributed fibre optic sensor.

In a dense homogeneous medium, as a perfect crystal at zero absolute temperature, the molecules are arranged in a very regular way and the medium's response is the same in every position. Due to the symmetric structure, all the scattering waves mutually cancel out for all angles except in the forward propagation. In this case, there is no scattering but just a change in the overall velocity of propagation [51]. However, if the medium is non-homogeneous, such as glass, the medium's response varies randomly, causing different orthogonal scattering components that do not vanish completely. Each molecule acts as a scattering centre and any imperfection in the structure modifies the optical properties and results in lateral and backscattering waves.

The great majority of existing DFOS are based on three scattering mechanisms: Rayleigh and

Brillouin scattering, where the backscattered signal inside the material is directly dependent on temperature and stress applied on the fibre; and Raman, where the backscattered signal only depends on the temperature [52]. The three scattering mechanisms can have two flavours: spontaneous and stimulated. When the input light does not affect significantly the properties of the medium, the scattering is linear and named as spontaneous. On the other hand, if the light intensity increases to a level where the optical properties of the medium are modified and the scattered light efficiency is proportional to the power of the input light, the scattering is considered stimulated and enters in a non-linear regime [23]. The different scattering phenomena will be explained in detail in the following sections.

2.2.1 Rayleigh and Mie Scattering

Rayleigh and Mie^I scattering occur when the optical power is transferred from one propagation mode to another keeping the same frequency, and result from the non-homogeneous fluctuations of the medium density [53, 54]. If the size (a), of the scattering centres is in the same order of magnitude or larger than the incident wavelength (λ), it is called Mie scattering. In this case, there is a deformation of the incident waveform causing diffraction and mainly forward scattering. If the size of the medium particles is much smaller than the incident wavelength, it is called Rayleigh scattering. The wavefront is not distorted and the scattering happens in all directions. Figure 2.8 shows the differences between Mie and Rayleigh scattering.

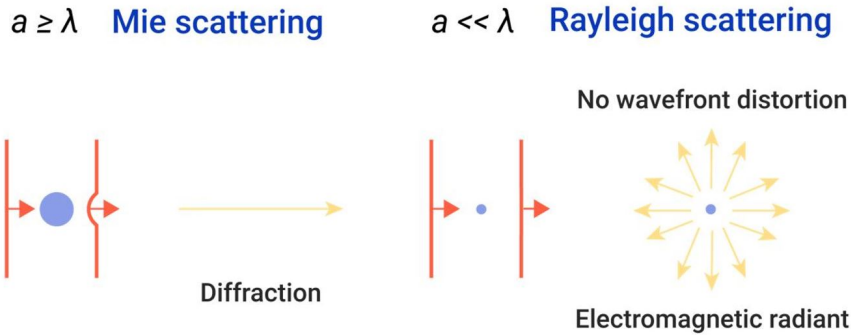


Figure 2.8 – Differences between Mie and Rayleigh scattering.

In Rayleigh scattering, part of the scattered light is recaptured by the waveguide and sent back in the opposite direction, as shown in Figure 2.9. This allows the incident and the backscattered waves to be injected in and measured from the same optical fibre end.

On the microscopic level, the molecular constituents of matter are constantly subjected to an intense ElectroMagnetic (EM) environment that is continuously rearranging their own electron cloud. These rearrangements influence the neighbouring molecules, which will readjust

^IIn this dissertation, the Mie scattering will not be addressed because it is irrelevant for studying scattering in optical fibres.

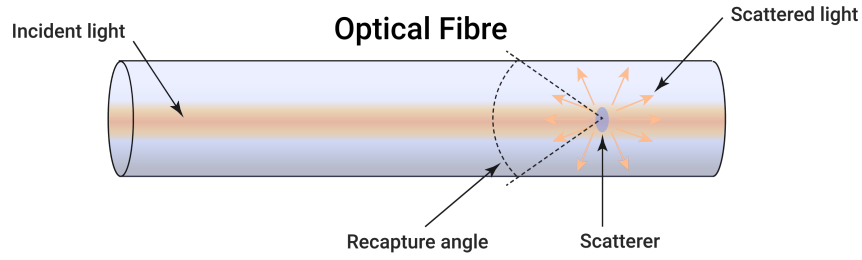


Figure 2.9 – Schematic of Rayleigh scattering in optical fibres.

to the new configuration and which in its turn generates fluctuations of density, temperature or strain in the internal structure. In the absence of incident light, these fluctuations will mutually cancel out and will not produce any macroscopic effect. On the contrary, when an incident wave propagates in the medium, the EM field reorients the random molecular fluctuations, creating a group response in the matter. The group response generates a macroscopic polarization, \mathbf{P} , that is proportional to the incident electric field, \mathbf{E} :

$$\mathbf{P} = \epsilon_0 \chi \mathbf{E} \quad (2.9)$$

where ϵ_0 is the permittivity of free space and χ is the susceptibility tensor that describes how the medium responds to an incident electromagnetic field.

Following the Maxwell equations, the electric displacement field vector, \mathbf{D} , is given by:

$$\mathbf{D} = \epsilon_0 \mathbf{E} + \mathbf{P} = \epsilon_0 (1 + \chi) \mathbf{E} = \epsilon \mathbf{E} \quad (2.10)$$

where ϵ is the dielectric tensor of the medium. Only the local variations of the dielectric tensor contribute to scattering so it can be written as:

$$\epsilon = \bar{\epsilon} \mathbf{I} + \Delta \epsilon \quad (2.11)$$

where $\bar{\epsilon}$ is the mean dielectric constant in the medium and \mathbf{I} is the identity matrix. The first component corresponds to the homogeneous contribution to the dielectric tensor and does not include any lateral scattering, while $\Delta \epsilon$ is the variation of the dielectric tensor expressed

as:

$$\Delta\epsilon = \Delta\epsilon I + \Delta\epsilon^t \quad (2.12)$$

The first term is a scalar contribution and originates from the fluctuations of thermodynamic quantities such as pressure, entropy, density and temperature. It results in Rayleigh and Brillouin scattering. The second term is the tensor term that results mostly in Raman scattering. In this section, only the first component responsible for Rayleigh scattering is explored.

The complex representation of the incident wave is written as [23]:

$$E(\mathbf{R}, t) = E_{\text{in}} \mathbf{e}_{\text{in}} e^{j(\boldsymbol{\beta}_{\text{in}}\mathbf{R} - \omega t)} \quad (2.13)$$

where E_{in} is the amplitude of the incident electric field, \mathbf{e}_{in} is the unit vector aligned with the state of polarization, $\boldsymbol{\beta}_{\text{in}}$ is the propagation vector, \mathbf{R} is the point of interest in the xyz coordinates and ω is the optical frequency. After the interaction between the incident field and a portion of the medium's volume (V), the scattered field at a position P far from the scattering volume is given by:

$$\mathbf{E}_s(\mathbf{R}, t) = E_{\text{in}} \frac{\omega^2}{c^2} [\mathbf{e}_s \times (\mathbf{e}_s \times \mathbf{e}_{\text{in}})] \frac{e^{j(\boldsymbol{\beta}_s\mathbf{R} - \omega t)}}{4\pi R} \frac{1}{\epsilon_0} \int_V \Delta\epsilon(\mathbf{r}', t) e^{j(\boldsymbol{\beta}_{\text{in}} - \boldsymbol{\beta}_s)\mathbf{r}'} d\mathbf{r}' \quad (2.14)$$

where c is the speed of light in free space, $\boldsymbol{\beta}_s$ is the propagation vector in the direction of the scattered wave, $\beta_s = |\boldsymbol{\beta}_s|$ and $R = |\mathbf{R}|$, \mathbf{e}_s is the unit vector aligned with the $\boldsymbol{\beta}_s$ direction. \mathbf{R} and \mathbf{r}' are the distance vectors described in Figure 2.10.

Analysing Figure 2.10, where the input light polarization is aligned with the X axis, and considering Equation 2.14, one can conclude that the scattered field is inversely proportional to the distance R between the position P and the scattering volume. The factor $e^{j(\boldsymbol{\beta}_s\mathbf{R} - \omega t)}$ expresses the phase change experienced by the scattered wave at the origin of the coordinate system and the vector $[\mathbf{e}_s \times (\mathbf{e}_s \times \mathbf{e}_{\text{in}})]$ indicates that the scattered field is proportional to $\sin\varphi$.

The scattered intensity (I_s) is proportional to the time averaged value of $\mathbf{E}_s \mathbf{E}_s^*$ and is given

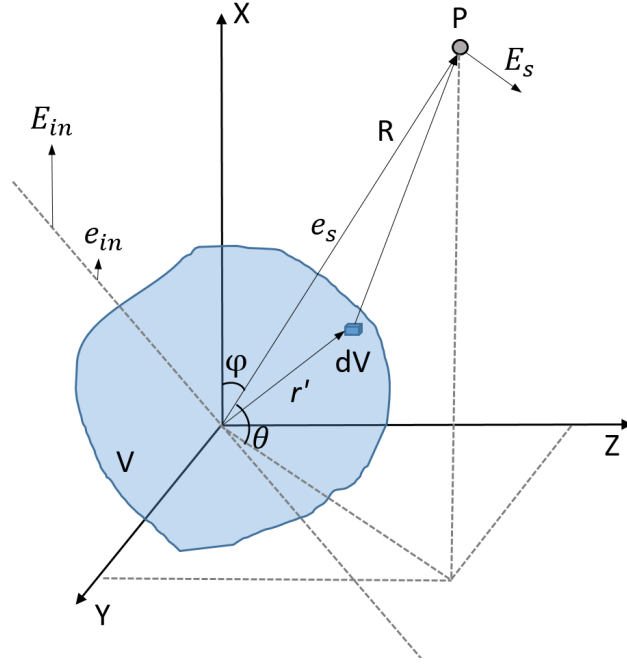


Figure 2.10 – Coordinate geometry for Rayleigh scattering.

by:

$$I_s = I_{in} \frac{\omega^4}{c^4} \frac{\sin^2 \varphi}{\epsilon_0^2 (4\pi R)^2} \int_V \int_V \langle \Delta\epsilon(\mathbf{r}'_1, t) \Delta\epsilon(\mathbf{r}'_2, t) \rangle e^{[i(\boldsymbol{\beta}_{in} - \boldsymbol{\beta}_s)(\mathbf{r}'_1 - \mathbf{r}'_2)]} d\mathbf{r}'_1 d\mathbf{r}'_2 \quad (2.15)$$

where I_{in} is the intensity of the input field.

As Equation 2.15 shows, the intensity of the light scattered by a particle much smaller than the wavelength is proportional to ω and, consequently, inversely proportional to the forth power of the wavelength, $1/\lambda^4$, as Lord Rayleigh found in 1871 [55]^{II}.

A simpler way to analyse the Equation 2.15 is to use the thermodynamic approach that consists in the description of the fluctuations in the material due to variations in density ρ and temperature T . The variation of the scalar term of the dielectric tensor $\Delta\epsilon$ is then given by:

$$\Delta\epsilon = \left(\frac{\partial \epsilon}{\partial \rho} \right)_{\rho_0} \Delta\rho + \left(\frac{\partial \epsilon}{\partial T} \right)_{T_0} \Delta T \quad (2.16)$$

^{II}These dependency explains why the telecommunications industry operates at higher wavelengths. Nowadays the most common used wavelengths is around 1550 nm, where the optical losses are the lowest [56].

where ρ_0 and T_0 are the average values of ρ and T in the medium, respectively. The second component can be neglected because the main variation of the dielectric constant is due to density fluctuations. The density variation can be expressed as function of the pressure p and entropy s of the medium:

$$\Delta\rho = \left(\frac{\partial\rho}{\partial p}\right)_{p_0} \Delta p + \left(\frac{\partial\rho}{\partial s}\right)_{s_0} \Delta s \quad (2.17)$$

where p_0 and s_0 are the average values of pressure and entropy of the medium, respectively. The first term corresponds to the pressure fluctuations, for a constant entropy, caused by the propagation of acoustical waves in the medium. This is the base of the inelastic Brillouin scattering that will be described in the next section. The second term corresponds to the entropy variations at constant pressure that cause a scattered wave at the same frequency that the incident wave. This is the fundamental of the Rayleigh scattering and the intensity of the scattered wave in the volume V that is much smaller than the wavelength of the incident wave ($|\mathbf{r}'_1 - \mathbf{r}'_2|$) is given by:

$$I_s = I_{\text{in}} \frac{\omega^4 V^2 \sin^2 \phi}{16\pi^2 R^2 c^4} \frac{\langle \Delta\epsilon^2 \rangle}{\epsilon_0^2} = I_{\text{in}} \alpha_s \quad (2.18)$$

where α_s defines the scattering losses due to the fluctuations of the dielectric constant. $\Delta\epsilon$ is assumed constant within the volume V and $\langle \Delta\epsilon^2 \rangle$ is expressed as function of the thermodynamic quantity of density:

$$\langle \Delta\epsilon^2 \rangle = \left(\frac{\partial\epsilon}{\partial\rho}\right)_\rho^2 \langle \Delta\rho^2 \rangle = \gamma_e \frac{\langle \Delta\rho^2 \rangle}{\rho_0^2} \quad (2.19)$$

where γ_e is the electrostrictive constant.

The fluctuations of the dielectric constant are caused by two main reasons. The first, α_{s1} , is due the local fluctuations in the manufacturing process while the second, α_{s2} , is caused by the fluctuations of the material composition mainly caused by the doping. α_{s1} is given by:

$$\alpha_{s1} = (10\log e) \frac{8\pi^3}{3\lambda^4} (n_0^2 - 1)^2 K_B C_T T_f \quad (2.20)$$

where K_B is the Boltzmann constant, C_T is the isothermal compressibility, T_f is the fusion

temperature and n_0 is the refractive index. α_{s2} is given by:

$$\alpha_{s2} = (10 \log e) \frac{8\pi^3}{3\lambda^4} \left(\frac{\partial n_0^2}{\partial N} \right)^2 \langle (\delta N)^2 \rangle \quad (2.21)$$

where N is the number of dopant molecules per unit of volume and $\langle (\delta N)^2 \rangle$ the mean square fluctuations of N compared to a homogeneous contribution.

Rayleigh scattering determines the minimum loss limit and that is an intrinsic characteristic of optical fibres. Even though the light losses have been significantly alleviated in the last years, it will never be completely suppressed because of the non-homogeneous nature of silica [57]. The Rayleigh scattering losses are approximately 0.15 dB/km, which are the typical losses achieved by the commercially available optical fibres. This scattering phenomenon is widely used to evaluate the losses over the optical fibre cables and the first experiment was demonstrated by Barnoski et al. in 1976 [58]. The setup is now commonly known as Optical Time-domain Reflectometry (OTDR).

Optical Time-domain Reflectometry

The principle of OTDR for Rayleigh backscattering detection is based on launching a pulse of light in the optical fibre and collecting the backscattered light in the same fibre end. The pulse round trip in the fibre results in a trace where each point represents one section/position of the fibre.

Typically, an OTDR system provides metre or sub-metre spatial resolution over tens of kilometres and there are three main types of Rayleigh OTDR systems: Incoherent-OTDR (I-OTDR), Polarization-OTDR (P-OTDR) and Phase-sensitive OTDR (ϕ -OTDR). The I-OTDR and P-OTDR techniques are briefly explained within this section, while the ϕ -OTDR has a dedicated section with a more detailed description.

Incoherent-OTDR

An I-OTDR measures the intensity of the reflected light and requires a high-power broadband incoherent source and a long acquisition time due to the weak Rayleigh signal. This method is most generally used by the telecommunications industry to locate anomalous points in the optical fibre cable.

When the input light launched into the optical fibre is a pulsed signal with a pulse width W , the location Δz where a perturbation occurs can be measured by the time delay of the speed

of light (c), as Equation 2.22 shows.

$$\Delta z = \frac{Wc}{2n_0} \quad (2.22)$$

The factor 2 is due to the round-trip experienced by the light.

The backscattered power of the Rayleigh scattering at a given position, z , is given by [23]:

$$P_R(z) = P_0 \alpha_s(\lambda, z) B_c(\lambda, z) \frac{W}{2} e^{-2\alpha z} \quad (2.23)$$

where P_0 is the pulse peak power, α_s is the scattering coefficient, B_c is the recapture coefficient, and α is the attenuation coefficient.

A typical response of an I-OTDR is shown in Figure 2.11. Connectors, bends, cracks but also the reflections at the input connector and at the optical fibre end will cause significant attenuation. The slopes in the optical power trace are due to the intrinsic optical fibre losses.

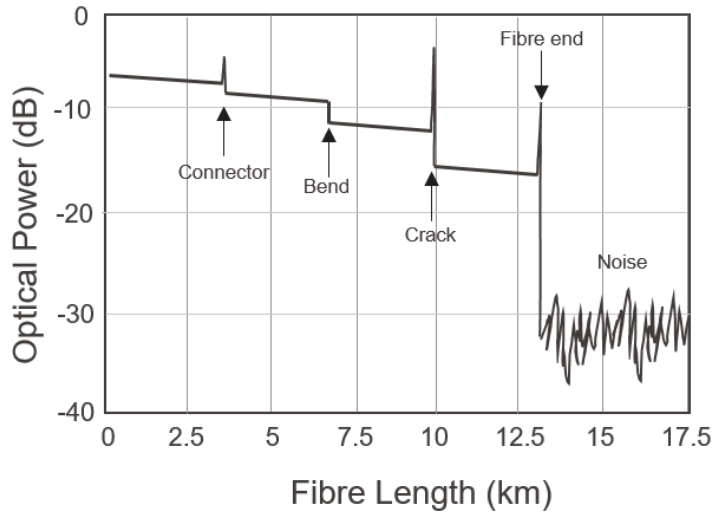


Figure 2.11 – Typical response of an I-OTDR.

Polarization-OTDR

A P-OTDR was proposed in 1981 [59] and consists of an OTDR setup followed by a polarizer that maintains the State of Polarization (SOP) of the input optical pulses. Polarized pulses are sent through a coupler towards the Fibre Under Test (FUT). The information contained in the SOP of the backscattered light is converted by a polarization-sensitive system into optical power that is measured by the OTDR.

If a perturbation occurs in one location, such as temperature, pressure, strain torsion or Faraday rotation, the SOP is modulated. This method can also be used to measure local birefringence, which is the optical property of a material having a refractive index that depends on the polarization and propagation direction of light.

Polarization measurements require the use of a coherent source to avoid light depolarization and one disadvantage of the P-OTDR technique is that a change of the SOP in one position can be affected by various parameters and in most of the cases, it is difficult to differentiate the contributions of the individual parameters.

Both techniques explained previously are used to detect dynamic perturbations but they are not able to quantify those perturbations. A technique capable of quantify the perturbations is the Phase-sensitive OTDR (ϕ -OTDR), which is used for monitoring the phase of the Rayleigh backscattered light along the sensing fibre.

ϕ -OTDR Technique

A standard I-OTDR uses a low coherence optical source but if the light source used in the setup is a highly coherent optical pulse, the system is called ϕ -OTDR. The ϕ -OTDR technique interrogates an optical fibre through the propagation of a sequence of rectangular optical pulses [60]. In this case, the laser coherence length is longer than the distance between two consecutive reflector centres and the total backscattered signal does not only depend on the intensity reflected by each centre, but also on the phase interference of the total backscattered field present in each fibre section, as shown in Figure 2.12.

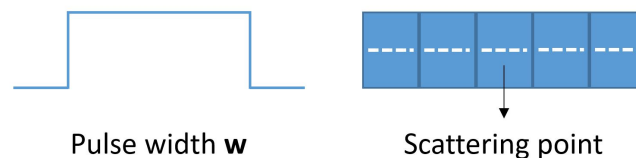


Figure 2.12 – Comparison between the pulse width and the scattering points.

The ϕ -OTDR is an interrogation technique that measures the noise-like but static Rayleigh backscattering signal caused by the frozen and random longitudinal entropic fluctuations of the Refractive Index (RI) alongside the optical fibre [61]. The fibre optic should be seen as a series of closely-packed refractive index discontinuities and each one causes a tiny and random amount of reflection, as represented in Figure 2.13. This method takes a "photo" of the optical fibre's core structure in order to have the fibre pattern that changes randomly if a perturbation occurs.

The backscattered light from the different scattering points interferes within the pulse width and results in a randomly varying signal in time which is highly dependent on the optical frequency and the refractive index. A typical ϕ -OTDR trace is shown in Fig 2.14.

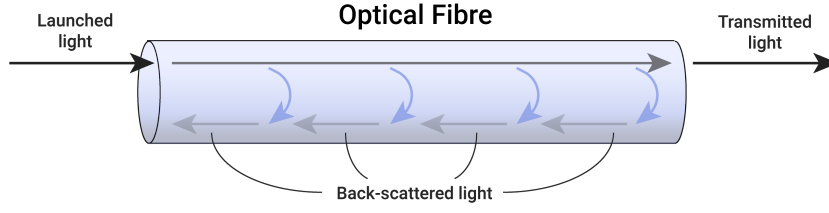
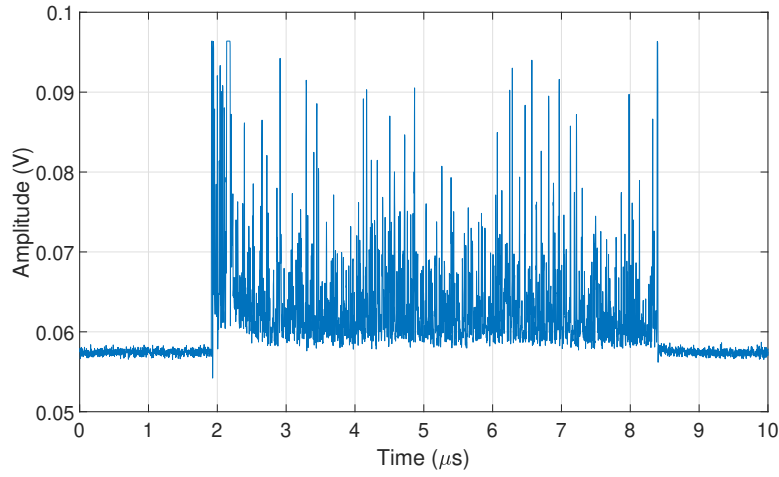


Figure 2.13 – Scattering mechanisms in the optical fibres.

Figure 2.14 – A typical ϕ -OTDR trace of a 650-metres long standard optical fibre.

This trace can be exactly reproduced under the same experimental conditions of temperature, strain and optical frequency and the complex amplitude of the reflected light vector from the scattering point at the position z is given by [62]:

$$\mathbf{E}_s(z) = \mathbf{E}_0 r_e(z) e^{-\alpha z + j\phi(z)} \quad (2.24)$$

where \mathbf{E}_0 is the input optical field, α the fibre's loss coefficient and $r_e(z)$ the complex reflection coefficient. The optical phase, ϕ , is expressed as:

$$\phi(z) = \int_0^z \beta(x) dx = 2\pi \frac{\nu}{c} \int_0^z n(x) dx \quad (2.25)$$

where β is the local propagating constant of the fibre.

A frequency-scanned ϕ -OTDR technique requires acquiring repeatedly the Rayleigh scattered intensity traces by sweeping the carrier optical frequency of the optical pulse, as demonstrated in Figure 2.15. Each fibre position will be individually analysed at different frequencies and, if the fibre is subjected to any change of temperature or strain, which changes its refractive index, the local spectrum will equivalently experience a frequency shift, similarly and in the same proportion like in a FBG.

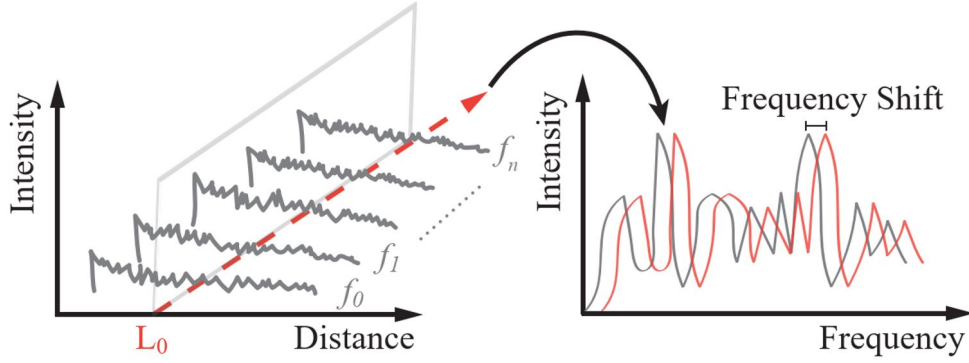


Figure 2.15 – Intensity of Rayleigh backscattered traces for the different scanning optical frequencies and respective local spectrum shift at position L_0 [63].

The spectrum frequency shift is generally estimated using techniques of cross-correlation between the two spectral distributions. It results in a correlation peak located at a frequency shift proportional to the local temperature or strain variations. The phase change is linearly proportional to the optical frequency shift $\Delta\nu$ and it is given by:

$$\Delta\phi_{ab} = \frac{2\pi n(z_a - z_b)}{c} \Delta\nu \quad (2.26)$$

The quantity ϕ_{ab} denotes the phase difference between the backscattered waves from the a and b scatter centres. Actually, the instrument determines an identical phase situation ($\Delta\phi_{ab}$) by compensating the change in the refractive index n by a frequency shift $\Delta\nu$, so that the product $n \times \Delta\nu$ remains constant. The sweeping range defines the maximum detectable temperature or strain changes while the frequency steps defines the minimum detectable variations of both measurands.

A deterministic spectral shift can also originate from a coating deformation, caused for example by the presence of water molecules that leads to local expansion/contraction. If the fibre is free of static mechanical strain, the total backscattered signal is only function of the temperature and humidity. With a proper temperature reference, the humidity can be measured and a distributed RH optical fibre sensor can be developed.

One important parameter of an OTDR system is its spatial resolution. The spatial resolution defines the minimum distance between two independent events that can be fully distinguished and the minimum length of an event. In general, the spatial resolution in an OTDR is determined by the pulse width and to achieve high precision spatial resolutions in the order of a millimetre, the required bandwidth is in the range of tens of GHz. Figure 2.16 illustrates the spatial resolution of an OTDR system.

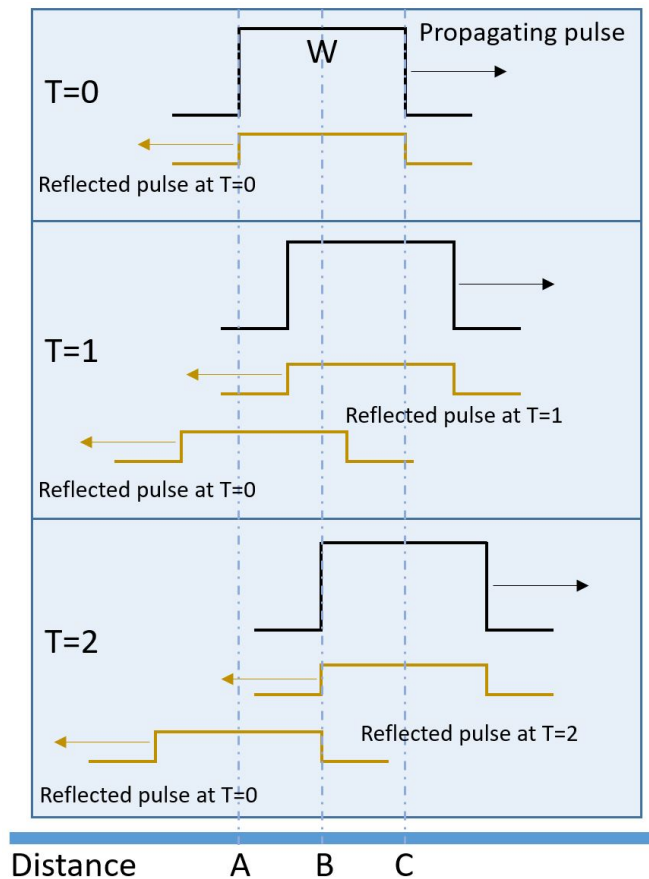


Figure 2.16 – Illustration of OTDR spatial resolution.

The incident pulse, with a duration of W , generates at time $T=0$ a reflected pulse that will propagate backwards at the same speed. The same incident pulse continues its propagation and generates a new reflected pulse afterwards, at time $T=1$, which will be partially overlapped with the previous reflected pulse. The overlap implies that, only at time $T=2$, the first reflected pulse at $T=0$ is totally spatially separated from the incident pulse and it can be perfectly discriminated. Therefore, the time difference between the two independent events should be always higher than $W/2$.

The pulse width has a direct influence on the spatial resolution. The shorter the pulse, the shorter the spatial resolution, however, shorter pulses also reduce the pulse energy, reducing also the Signal-to-noise Ratio (SNR). Consequently, due to the natural losses in the optical

fibre, the sensing length is also reduced. A trade-off between spatial resolution and sensing range should be found in any OTDR setup.

Chirped-pulse Phase-sensitive OTDR

If the probe pulse has a linear frequency variation along the pulse width, the system is called CP- ϕ -OTDR, which is, nowadays, a fast, powerful and highly sensitive refractive index sensor for Distributed Acoustic Sensing (DAS) [64].

The CP- ϕ -OTDR interrogator technique relies on the same working principle of ϕ -OTDR but instead of sweeping the laser frequencies, it produces a linear chirp with different frequencies that generates the same trace pattern for the same fibre. The method achieves spatial resolutions in the centimetre range, with a increasing SNR by several orders of magnitude with respect to the conventional ϕ -OTDR technique [65, 66]. Typically, a picosecond probe optical pulse is amplified and time stretched before launching it into the FUT.

Assuming that the frequency profile of the linear chirped pulse is given by:

$$\nu(t) = \nu_0 + \left(\delta\nu/2 - \frac{\delta\nu}{W} t \right) \quad (2.27)$$

where ν_0 is the central frequency, $\delta\nu$ is the spectral width, and $\delta\nu/W$ the frequency chirp rate. Substituting Equation 2.27 in Equation 2.26, the phase change induced by external temperature or strain is given by:

$$\Delta\phi_{ab} = -\frac{2\pi \sum_{i=a}^b n(i) \Delta z}{c} \left(\frac{\delta\nu}{W} \right) \Delta t \quad (2.28)$$

CP- ϕ -OTDR avoids the need of rigorous acoustic and thermal stabilization, because the measurements are based on a single-shot pulse rather than a large laser frequency sweeping. At the same time, it does not need a laser source with a large linewidth and eliminates the fading problems generated when the scattering of a single position is extremely low. The Rayleigh scattering is formed by the superposition of the waves generated by the random photons in each section and if the input light pulses have always the same power, as it happens in a traditional ϕ -OTDR, statistically the scattering random pattern has significant fluctuations in the power that may have some values near zero fading the signal [67]. However, when using probe pulses whose power is varying over its width, the modulation instability-induced by the signal fading is significantly reduced [68]. On the other side, the spatial resolution is limited to the metre range because of the weak Rayleigh intensity traces and the bandwidth required at the receiver is the same as the coherent detection, limiting the maximum measurements

range.

Generally, one disadvantage of the OTDR techniques is the dead-zone in which the interrogator is momentarily blind to measuring reflected energy. This dead-zone is caused by the initial peak reflection in the fibre connector that saturates momentarily the photodetector. Dead-zones are typically in the order of metres, making the OTDR unsuitable for low length applications where a high spatial resolution is required. To overcome this limitation either a relatively broadband light can be implemented or use multiple interrogation frequencies.

Optical Frequency-domain Reflectometry

A distributed fibre optic sensor can be realized also in the frequency domain and an Optical Frequency-domain Reflectometry (OFDR) system has similar purposes as an OTDR. An OFDR system, which was firstly introduced by Eickhoff and Ulrich, can have a sub-millimetre spatial resolution but limited to some metres of sensing range [69]. In this case, the monochromatic light source frequency is linearly changed, by changing the input current of the laser, and the frequency response of the fibre is converted into the time/spatial domain by computing the Fast Fourier Transform (FFT). This technique requires a coherent detection scheme that limits the sensing range to the coherence length of the interrogation light. The spatial resolution of an OFDR system depends on the frequency tuning range of the interrogation light rather than on the detector bandwidth, as it happens in an OTDR setup.

The input laser is used as a reference and it is combined with the backscattered light, creating an interference signal. The beat frequency of this interference corresponds to the path length difference of the Rayleigh scattered light. The spatial resolution, Δz , of an OFDR system is given by:

$$\Delta z = \frac{c}{2n_0\Delta F} \quad (2.29)$$

where ΔF is the frequency scanning range, which can be typically few tens of GHz, meaning that the spatial resolution can be in the centimetres scale. That is the main advantage of the OFDR compared with the OTDR. On the other side, the drawback of the OFDR is its limited measurement range of around tens of metres because it requires coherent detection and therefore, the coherence length of the laser source sets a hard limit to the fibre sensing length.

2.2.2 Raman and Brillouin Scattering

Non-linear Brillouin and Raman scattering are due to the inelastic collisions and a shift in the backscattered frequency happens. The cohesive forces between molecules allow two distinct collective vibration modes, the acoustic-like and the optical-like vibration modes.

The acoustic-like vibration is a slow vibration classical wave with high momentum and it is caused by the oscillatory movement of the entire molecular chain. It causes a small spectral shift, which is defined as Brillouin Scattering, of about 10 GHz or 0.07 nm at $\lambda_0 = 1550$ nm in SiO₂. The optical-like vibration is the vibrational mode inside the molecular chain caused by the high-energy phonons^{III} with low momentum. This component is stress insensitive and the spectral shift, named as Raman Scattering, is around 12 THz or 97 nm at $\lambda_0 = 1550$ nm in SiO₂. Figure 2.17 shows the difference between the acoustic-like vibrations, in the left, and the optical-like vibration in the right.



Figure 2.17 – Differences between the acoustic-like vibration in the left and the optical-like vibrations in the right.

The inelastic scattering, which is thermally activated and generated by thermal phonons, has two possible components: Stokes and anti-Stokes. The frequency shift of the Stokes and anti-Stokes components are usually described using a quantum-mechanical approach explained in Figure 2.18.

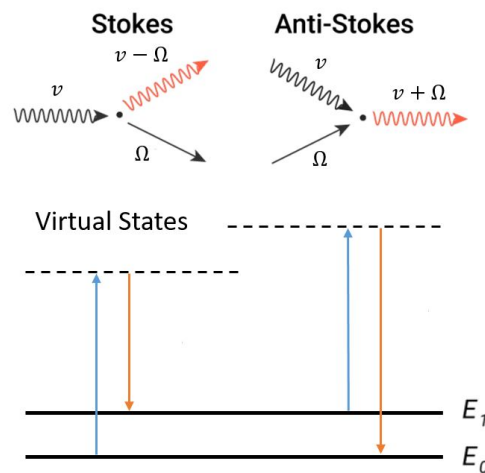


Figure 2.18 – Energy diagram of Stokes and Anti-Stokes components.

Stokes scattering happens when a molecule is in the ground state, E_0 , and absorbs a pump photon (ν). The electron jumps from its energy level to a virtual state of higher energy and to keep the energy equilibrium, a lower frequency photon, $(\nu - \Omega)$, is emitted causing a red-shift in the scattered wavelengths. Anti-Stokes scattering happens if the molecule is already in a

^{III}Quantum mechanical description of an elementary vibration state.

vibrational state, E_1 , and, after the interaction with some energy available in the medium, a photon of higher energy, $(\nu + \Omega)$, is generated causing a blue-shift in the wavelengths.

In summary, Figure 2.19 groups the three main scattering mechanisms in the same plot.

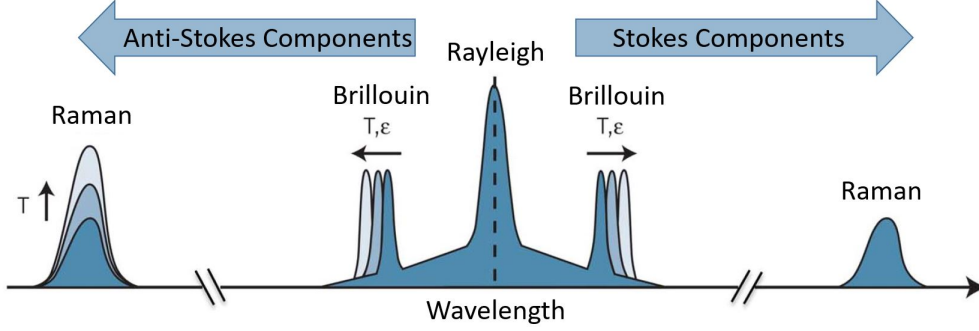


Figure 2.19 – Spectrum of the light spontaneously scattered in optical fibres [70].

Raman Scattering

Raman scattering was first observed by C. Raman in 1928 and is caused by the vibrational transitions at the molecular level [71]. The Raman frequency shift (ν_R) is function of the frequency of the scattered photon that depends on the angular frequency of the thermal vibration $\omega \pm \Omega_A$, where ω is the frequency of the incident photon.

$$\nu_R = \frac{\Omega_A}{2\pi} \quad (2.30)$$

The average number of the phonons thermally activated N_{ave} , following the Bose-Einstein distribution is expressed in Equation 2.31 and represents the strength of the anti-Stokes component because a phonon and a incident photon are annihilated to generate a new photon [23]. On the other side, the strength of the Stokes is proportional to $N_{\text{ave}} + 1$ due to the annihilation of the incident photon to generate a new phonon and a new photon.

$$N_{\text{ave}} = \frac{1}{\exp\left(\frac{h\nu_R}{K_B T}\right) - 1} \quad (2.31)$$

where K_B and T are the Boltzmann constant and the absolute temperature in Kelvin, respectively, and h is the Planck constant.

At room temperatures, N_{ave} is approximately 0.13 while $N_{\text{ave}} + 1$ is approximately 1.13. Due to this difference in the transitions rate, the anti-Stokes sensitivity to temperature is much

higher than the Stokes sensitivity (0.8% to 0.1% at 300K) and the ratio between both is the basic principle of a Raman Distributed Temperature Sensor (DTS) [72]. The Stokes and anti-Stokes will propagate in the fibre with different attenuation and the power ratio between both gives the temperature changes.

$$S_R = \frac{N_{\text{ave}}}{N_{\text{ave}} + 1} = \exp\left(-\frac{h\nu_R}{K_B T}\right). \quad (2.32)$$

The main advantage of a Raman DTS is its insensitivity to strain [73] and it can be found in several commercial thermometry applications [74]. On the other side, the main disadvantage of a Raman distributed sensor is that the amount of the backscattered light is low and for that reason, it requires the use of multimode fibres to increase the recaptured power. The use of multimode fibres limits the maximum sensing range due to the inter-modal light dispersion.

Brillouin Scattering

The last scattering mechanics explained in this chapter is Brillouin scattering [75]. It results from the interaction between the light and the density fluctuations induced by the propagation of acoustic waves in the fibre [23].

Acoustic photons carry a momentum that grows proportionally with the phonon frequency, and the proportional factor is given by the acoustic velocity V_a in the medium. Since energy and momentum must be conserved during the interaction, the Brillouin effect observation involves 3 waves: the incident ν , the scattered ν' and the acoustic wave Ω .

Equation 2.33 represents the energy conservation while the momentum conservation is given by Equation 2.34.

$$h\nu = h\nu' + h\Omega \quad (2.33)$$

$$\hbar \vec{k} = \hbar \vec{k}' + \hbar \vec{q} \quad (2.34)$$

where \vec{k} , \vec{k}' and \vec{q} are the respective wave vectors of the incident, scattered and the acoustic waves.

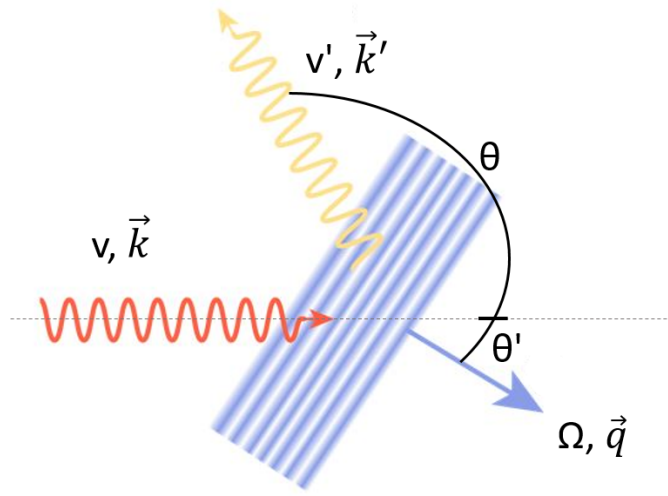


Figure 2.20 – Illustration of Brillouin scattering.

Coupling the previous equations and projecting each components as Figure 2.20 demonstrates, one can conclude that:

$$\begin{cases} k' \sin \theta = q \sin \theta' \\ k = k' \cos \theta + q \cos \theta' \end{cases} \quad (2.35)$$

After squaring and summing the coupled equations and using the relationships between frequencies and wavenumbers, $\nu = kc/2\pi$, $\nu' = k'c/2\pi$ and $\Omega = qV_a/2\pi$, the general Brillouin relation is given by :

$$4V_a^2 \nu(\nu - \Omega) \sin^2 \frac{\theta}{2} = (c^2 - V_a^2) \Omega^2 \quad (2.36)$$

Solving for Ω yields:

$$\Omega = 2 \frac{V_a}{c} \nu \sin \frac{\theta}{2} \sqrt{1 - \left(\frac{V_a}{c}\right)^2 \cos^2 \frac{\theta}{2}} - 2 \left(\frac{V_a}{c}\right)^2 \nu \quad (2.37)$$

Considering $V_a \ll c$:^{IV}

$$\Omega = 2 \frac{V_a}{c} v \sin \frac{\theta}{2} = 2n \frac{V_a}{\lambda_0} \sin \frac{\theta}{2} \quad (2.38)$$

where λ_0 represents the wavelength of the incident light.

In optical fibres, light propagation is constrained to the optical axis, so the scattering angle can either be fully forward (0) or fully backward (π), since light is guided. The simplified Brillouin Frequency Shift (BFS) is given by:

$$\nu_B = \frac{2V_a}{c} v = \frac{2nV_a}{\lambda} \quad (2.39)$$

The BFS depends on multiple parameters such as the presence of dopant in the core as well as the fabrication process and it is usually between 9 and 11 GHz. Although the effective refractive index (n) also affects the Brillouin frequency changes via temperature and strain, the main effect exploited in a Brillouin sensor is the change of the acoustic velocity due to these quantities. Typically the temperature coefficient in a Brillouin system is 1 MHz/K and the strain coefficient is 50 kHz/ $\mu\epsilon$.

Some examples of distributed sensing techniques exploring Brillouin scattering are the Brillouin Optical Time-domain Reflectometry (BOTDR) and Brillouin Optical Time-domain Analyser (BOTDA).

The working principle of a BOTDR is similar to the traditional OTDR but the backscattered effect analysed is the spontaneous Brillouin rather than the Rayleigh. The wavelength and the intensity of the spontaneous Brillouin backscattered are used to map the temperature and strain along the fibre, however, as the intensity is very weak, one needs to average over a large number of measurements to have a good SNR factor. Its sensing distance can reach tens of kilometres by accessing only one end of the fibre, and as in the OTDR, the spatial resolution is determined by the probe pulse width [76].

However, increasing the pump laser intensity, the electrostriction process in the molecular structure increases, and the Brillouin scattering will be optically stimulated. The technique is called Stimulated Brillouin Scattering (SBS) and it is illustrated in Figure 2.21.

^{IV}The acoustic velocity is approximately 5900 m/s in silica while the light velocity in the medium is 200000000 m/s.

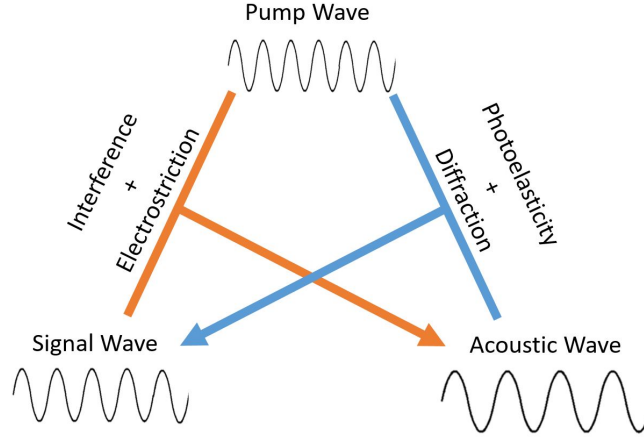


Figure 2.21 – Illustration of the Stimulated Brillouin scattering.

It is based on a positive feedback loop involving two complementary physical effects: photoelasticity, which refers to the variation of the refractive index by density changes, and electrostriction, which leads to an increase of material density in a dielectric when the latter experiences an intense electric field [77].

In the SBS technique, an optical pump wave (with frequency ν_p) interferes with a counter-propagating signal wave (with frequency ν_s). The resulting beat wave (with frequency $\nu_p - \nu_s$) produces, through electrostriction, an acoustic wave with the same frequency that travels at the acoustic velocity. The propagation of this acoustic wave creates a moving grating through photoelasticity that scatters back the pump wave. When the difference between the pump and the signal matches the Brillouin shift, the energy is transferred from pump to signal with the maximum efficiency [63]. As consequence, the increased signal will amplify the intensity of the beat wave and at the same time, the amplitude of the acoustics wave. Both the scattered light and the moving grating are enhanced with this positive feedback process. The amplitude of the three waves can be described by [78]:

$$\begin{cases} \frac{\partial E_P}{\partial z} - \frac{n_1}{c} \frac{\partial E_P}{\partial t} = E_A E_S \\ \frac{\partial E_S}{\partial z} + \frac{n_1}{c} \frac{\partial E_S}{\partial t} = E_A^* E_P \\ \frac{\partial E_A}{\partial z} + \Gamma_d E_A = \frac{1}{2} g_B E_P E_A^* \end{cases} \quad (2.40)$$

where E_P , E_S and E_A are the amplitude of the pump, signal and acoustic wave, respectively. $\Gamma_d = \Gamma_B + i2\pi\delta\nu_B$ is the damping factor that is related to the photon life time $1/\Gamma_B$ and the

detuning factor $\delta \nu_B$. The Brillouin gain factor is given by:

$$g_B = \frac{2\pi n^7 p_{12}^2 K_P}{c \lambda^2 \rho V_A \nu_B} \frac{P_P}{A_{\text{eff}}} \quad (2.41)$$

where K_P is a factor varying from 0 to 1, that describes the alignment between the polarization states of pump and signal, P_P and λ are the power and wavelength of the pump, respectively, and A_{eff} is the effective core area.

One distributed fibre sensing technique that makes use of SBS is the BOTDA. In this method, two different counter-propagating waves (an optical pulse and continuous wave) are sent into the two opposite ends of the fibre and the interaction between both creates a propagating refractive index grating, which amplifies the intensity of the Brillouin backscattered light. The Continuous Wave (CW) light should be tuned to be in resonance with the Brillouin scattering and the maximum amplification for the pump/probe waves is reached. If the temperature or strain changes, the Brillouin resonance will be frequency shifted. As the stimulated Brillouin scattering is more intense, this system does not need long average times to have a reasonable SNR and can reach longer distances.

2.2.3 Distributed Fibre Optic Sensors for RH sensing

The measurement of relative humidity has significant importance in physical, chemical and biological processes in a large range of industrial applications and, in 1995, A. Kharaz and B. Jones developed a multi-point distributed humidity fibre optic sensing system [79]. At the sensing point along the fibre, the cladding was removed over 50 mm and replaced by the cobalt chloride-gelatine thin film with a refractive index greater than that of the fibre core. This way, practically all light launched through the fibre will traverse through the coating thus interacting with the changes in the atmospheric moisture. The authors used OTDR technique based on two pulsed laser diodes operating at 670 nm and 850 nm to analyse the response of HCS (Hard Clad Silica) optical fibres at different levels of RH from 20% to 80%. The sensor is based on the calorimetric interaction of water molecules and the coating of cobalt chloride, which results in a change of the light absorption properties that affects the attenuation experienced by the optical signal. More than 10 sensors can be placed on the same fibre that can have up to a kilometres of length.

In 2008, Galindez et al. studied the RH effect on the Brillouin frequency shift using a Brillouin distributed sensor with 10 metres of spatial resolution [80, 81]. In this study, three different types of single-mode fibres (SMF) with a 250 μm acrylate coating, with 1 kilometre of length, were exposed to different levels of RH (from 40% to 98%) at constant temperatures (25°C and 30°C). The authors concluded that changes of humidity affect non-linearly the Brillouin frequency shift, with a variation from 0.4 up to 2.8 MHz. Those RH variations, if

not considered and compensated accordingly, can induce an error from 0.4 up to 2.8°C in a temperature distributed fibre sensor based on Brillouin scattering. The main conclusion is that the optical fibre should be isolated from the humidity in order to have a correct measurement of temperature.

Lately, Liehr et al. developed a method for distributed humidity sensing using PolyMethyl MethAcrylate (PMMA) Polymer Optical Fibres (POF) [82]. Using a dual-wavelength photon-counting OTDR (ν -OTDR by Luciol Instruments), an analysis of the Rayleigh backscattering and the respective attenuation characteristics at 500 nm and 650 nm wavelengths was performed. The measurements were carried out at different RH values of 30%, 60% and 90% with a spatial resolution of about 10 cm. As expected, the authors found that the tested fibres present a relevant cross-sensitivity between temperature and humidity, but, at the same time, the RH sensitivities when analysing different wavelengths are different. If only the 500 nm backscatter traces are evaluated, a variation of 10°C can induce an error of about 12%, but, combining the transmission change effect at 650 nm, the temperature and RH changes in the fibre can be distinguished and unambiguously identified. The calculated RH resolution measurement is in the order of 1-2% of RH over an extended sensor length of up to 200 metres.

In 2017, P. J. Thomas and J. O. Hellevan presented a study about the characteristics of a 64 metres long distributed relative humidity sensor with centimetre spatial resolution [83]. In this study, the setup is composed of different kinds of fibres with different polyimide coating thicknesses and the strain variation alongside the fibre is measured using an Optical Backscattered Reflectometer (OBR) 4600 interrogator, from Luna Technologies, which is based on the OFDR technique. The tests were performed varying the humidity from 15 to 92% of RH and the system could resolve relative humidity changes of 0.1% with a near linear sensitivity of $1.3 \mu\epsilon/\%RH$ across the entire range of humidity tested. The response time of the sensor was found to be strongly dependent on temperature and the fibres measurements show low hysteresis. Using a temperature reference, the system was able to accurately measure RH distributions on a centimetre spatial scale.

More recently, in 2020, R. Wright et al. developed a fully distributed optical fibre sensor for humidity monitoring at high temperatures using an off-the-shelf single mode fibre connected to an OBR interrogator [84]. OBR is based on the OFDR technique and the target application was the water condensation detection along the natural gas transmission pipelines. The authors also used a uncoated optical fibre as temperature reference and study the response of both fibre samples at different relative humidity levels, from 0% to 100% and different temperatures, from 21°C to 50°C. The main conclusions were that the uncoated optical fibre can be used as temperature reference and increase of temperature decreases the sensitivity to RH and the temperature sensitivity is approximately 10 times higher than the RH sensitivity.

The main challenge ahead in all thermo-hygrometer sensors is the decoupling of the temperature and humidity effect, specially in fibre optic sensors where the temperature sensitivity is usually much higher than the RH sensitivity. Different decoupling techniques

can be implemented, such as using two parallel sensing fibres with different temperature and RH sensitivities, or using a completely stripped fibre for temperature reference [85]. One last technique is to isolate completely one fibre with a metallic shield, to block the humidity absorption by the fibre coating, and turn it into a pure temperature reference. The first solution takes advantage from both fibres experiencing the same environmental conditions (ΔT and ΔRH) and it is based on a dual equation matrix system (Equation 2.42):

$$\begin{bmatrix} \nu^1 \\ \nu^2 \end{bmatrix} = \begin{bmatrix} \alpha_T^{(1)} & \alpha_{RH}^{(1)} \\ \alpha_T^{(2)} & \alpha_{RH}^{(2)} \end{bmatrix} \begin{bmatrix} \Delta T \\ \Delta RH \end{bmatrix} \quad (2.42)$$

where the upper index denotes one of the two sensing fibres, ν is the frequency shift measured by each fibre, α_T and α_{RH} the temperature and the RH sensitivity respectively. The measurement resolution increases with increasing the RH sensitivities ratio between the two fibres and, if the difference between the RH sensitivities of the selected fibres is minor, the system ends up having an intrinsically poor resolution, which is always limited by the less RH sensitive fibre. The second decoupling solution using a stripped fibre, which essentially solves the resolution limitation, because the reference fibre is completely RH insensitive, but another relevant issue arises that is the fragility of the fibre. Using a stripped fibre only works in extremely controlled environments, which is impossible for field applications, and is also very difficult to achieve because it requires manual stripping. The third technique that uses a humidity shielded fibre reduces the ease of handling and increases significantly the cost of the fibre, mostly because it increases the manufacturing complexity. Ideally, a RH insensitive coated fibre should be found.

2.3 Conclusions

Some distributed fibre sensors are installed at CERN in different areas such as radiation dosimetry [86] or structural health monitoring [87], but there is no application using a RH distributed fibre sensor. At the same time, to the best of our knowledge, there is no evidence of a commercial solution to monitor RH over large distances using optical fibres. Considering the above mentioned, the main objective of this dissertation is the development of a new interrogation technique fully capable of measuring and decoupling temperature and RH over kilometres of sensing range using optical fibres. After analysing carefully the scattering processes and the DFOS technology fundamentals, the ϕ -OTDR technique seems to be the best candidate for three main reasons:

- Ultra high sensitivity and capacity of measuring kilometres of sensing range;
- Simple and requires access to only one optical fibre end;
- Rayleigh scattering is the strongest of all scattering phenomena.

3 Acrylate- and Polyimide-coated Fibres

As explained in Chapter 1, monitoring RH is a vital task for the good operation of the CERN LHC machine and should be performed over a large number of sensing points. The harsh environment requires the use of FOS and apart from their advantages of being small and radiation-resistant, they represent a unique solution for multiplexing a large number of measurements points. Before the installation, at the first stage, the developed RH-FOS should be intensively studied and their responses should be characterized under the same temperature and RH conditions as the target areas in the LHC detectors. At the second stage, the sensors should be characterized under the same radiation environments. The radiation studies are not explored in this dissertation and will be included in future works.

The content of this chapter is divided into 3 sections. The first section presents the first proof of concept of a highly sensitive RH distributed fibre sensor using a ϕ -OTDR setup with 10 kilometres of sensing range. The system interrogated several acrylate- and polyimide-coated optical fibres from different manufacturers at 25°C¹ with 70 centimetres of spatial resolution. The choice of polyimide-coated optical fibres was based on the well-known behaviour stability of polyimide at different temperatures [88], but also in the good and continuous response of the polyimide-coated FBGs 7 years after the installation in CMS [36]. At the same time, as the acrylate-coated fibres are the most standard and used optical fibres in the sensing applications, their responses under different levels of temperature and RH should also be investigated. The results were presented at the 7th European Workshop on Optical Fibre Sensors (EWOFS) [89]. The second section explores the effect of RH in the same coated optical fibres but in a larger range of temperature from -20°C to 50°C. The results were obtained using a CP- ϕ -OTDR with 6 metres of spatial resolution and were published at the 27th International Conference on Optical Fibre Sensors (OFS) [90]. The last section presents the mathematical model built to validate the experimental results of polyimide-coated fibres under a RH test at constant temperature and a temperature test at constant RH.

¹In this dissertation, the temperature values written in the text to describe the conditions of a test are the preset values of the temperature controller. These values differ slightly from the temperature measured by the additional electronic references.

3.1 A Kilometre-Range Distributed Relative Humidity Sensor

The main objective of this study was the validation of the RH-DFOS concept, already demonstrated in some state of the art references [82, 83, 85], but using, for the first time, a ϕ -OTDR interrogation setup. An additional objective was to find the most suitable coated optical fibre to be implemented as a RH sensor, as well as the one that can be used as temperature reference.

3.1.1 Experimental Setup

The setup is composed of 9 different appended optical fibres rearranged in a single FUT installed in stress-free holders, as seen in Figure 3.1.

A sample of a bare fibre, i.e., with the coating completely stripped ^{II}, was also added to the FUT to be the temperature reference. The FUT was tested in a climatic chamber (Binder 720L) equipped with temperature and RH electronic references sensors (PT100 and HIH4000) installed individually in each fibre spools holders. The electronic sensors signals were acquired with a Arduino-based acquisition unit controlled by a Python visual interface.

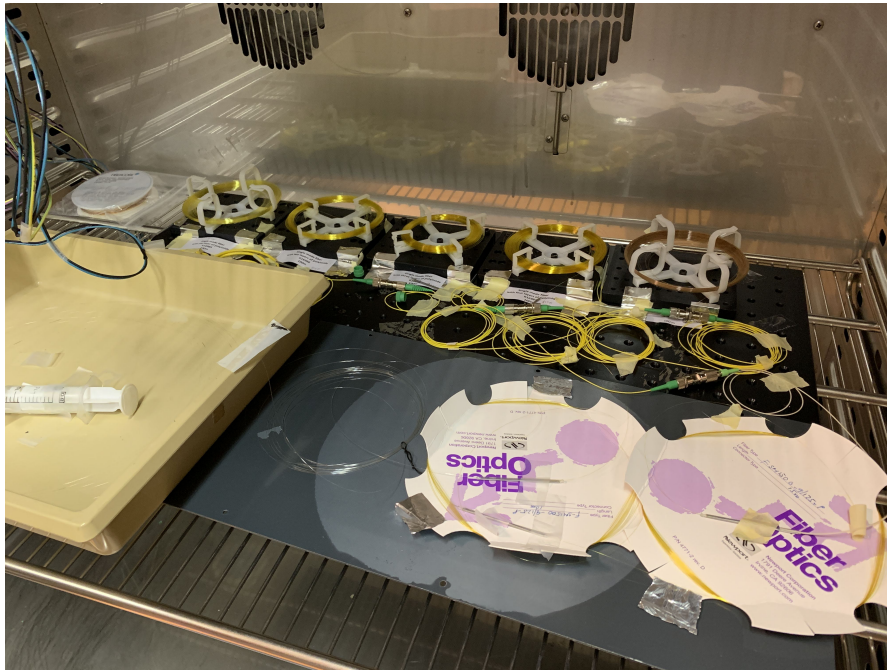


Figure 3.1 – Optical fibres coiled in a stress-free configuration inside the climatic chamber.

The list of FUT with their respective characteristics is listed in Table 3.1.

^{II} A standard acrylate-coated fibre was manually stripped with a fibre optic stripper.

Table 3.1 – List of FUT and respective coating characteristics and lengths.

Manufacturer	Product Number	Coating Thickness (μm)	Number of Coating Layers	Length (m)
Polyimide-coating				
RISE ^o	-	4	1	100
	-	8	2	100
	-	12	3	100
	-	16	4	100
Nufern	S1310-P	12.5	*	100
FiberCore ⁺	SM1500(9/125)P	*	1	20
	-	15	*	15
Stripped-coating				
Bare"	OS2 / G.652.D	-	-	10
Acrylate-coating				
Dätwyler	OS2 / G.652.D	62.5	2	20

^o The RISE optical fibres were specially produced for this research work

⁺ The FiberCore with 1 coating layer is a special sample

* Data not provided by the manufacturers

- Not applicable

" The bare fibre is a uncoated sample of Dätwyler acrylate-coated fibre

Optical Interrogator

The home-made optical interrogator used in this test is a 70-centimetres spatial resolution ϕ -OTDR and its schematic is presented in Figure 3.2.

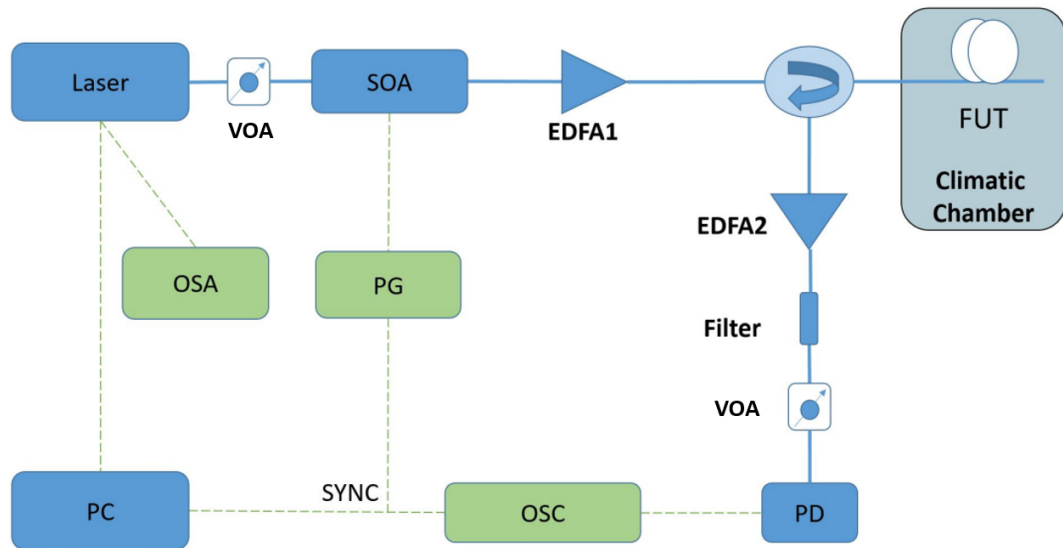


Figure 3.2 – Full schematic of the ϕ -OTDR setup. VOA - Variable Optical Attenuator; SOA - Semiconductor Optical Amplifier; EDFA - Erbium-Doped Fibre Amplifier; PD - PhotoDetector; OSA - Optical Spectrum Analyser; PG - Pulse Generator; OSC - Oscilloscope.

A Distributed FeedBack (DFB) laser with 1 MHz linewidth is employed as a laser source. Then, a Semiconductor Optical Amplifier (SOA) driven by a Pulse Generator (PG) is used to shape the continuous laser light into a coherent pulse. After the pulse shaping, an Erbium-Doped Fibre Amplifier (EDFA) is used to amplify the pulse before launching it to the fibre under test through a circulator. The output of the circulator is connected to another EDFA, which amplifies the Rayleigh backscattered signal and then, a tunable filter (1550 nm) is connected to filter out the EDFA amplified spontaneous emission before photo-detection. The PhotoDetector (PD) is then connected to a fast oscilloscope for data acquisition. An Optical Spectrum Analyser (OSA) is used to tune the filter to match the laser wavelength. A LabVIEW Visual Interface (VI) controls the laser current sweeping and acquires all the traces measured by the Oscilloscope (OSC). Two Variable Optical Attenuators (VOA) are placed before the SOA and the PD, the first to prevent non-linear effects caused by a too intense optical pulse and the second to avoid the PD power saturation.

3.1.2 Experimental Results

As the environment in the climatic chamber is uniform, the results of each optical fibre are the average value over the entire length. Due to the hydrophobic properties of silica, it is expected that the bare fibre is insensitive to RH [34]. For that reason, it can provide the temperature reference for the coated optical fibres, in view of correcting for the temperature/RH cross-sensitivity. To validate that approach, the traces of the bare fibre and the temperature measured by the electronic reference during a RH test are plotted together in Figure 3.3.

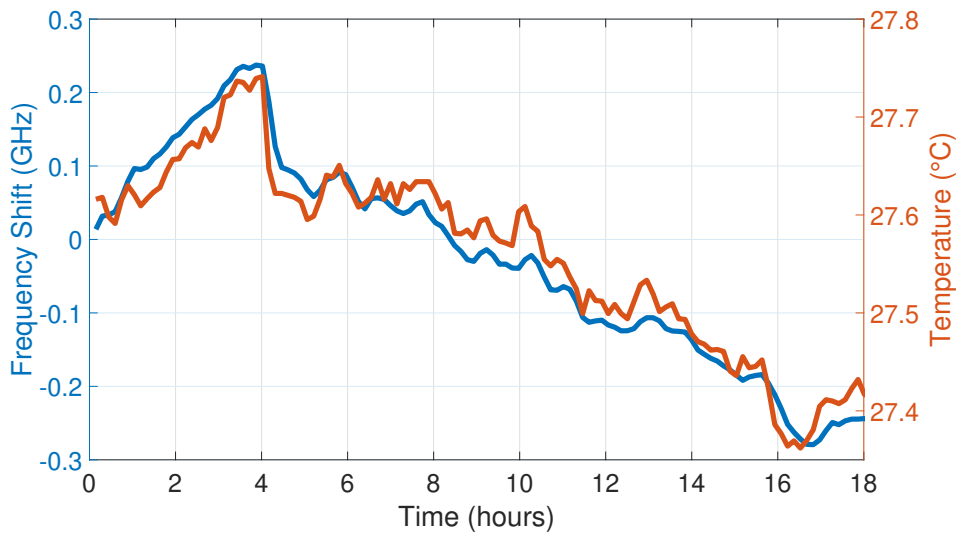


Figure 3.3 – Comparison between the electronic temperature reference, in orange, and the bare fibre signal, in blue.

The results demonstrate the agreement between the responses of reference sensor and bare fibre, meaning that the bare fibre is a pure temperature sensor and the temperature

compensation method is valid. The climatic chamber conditions during the RH test are plotted in Figure 3.4.

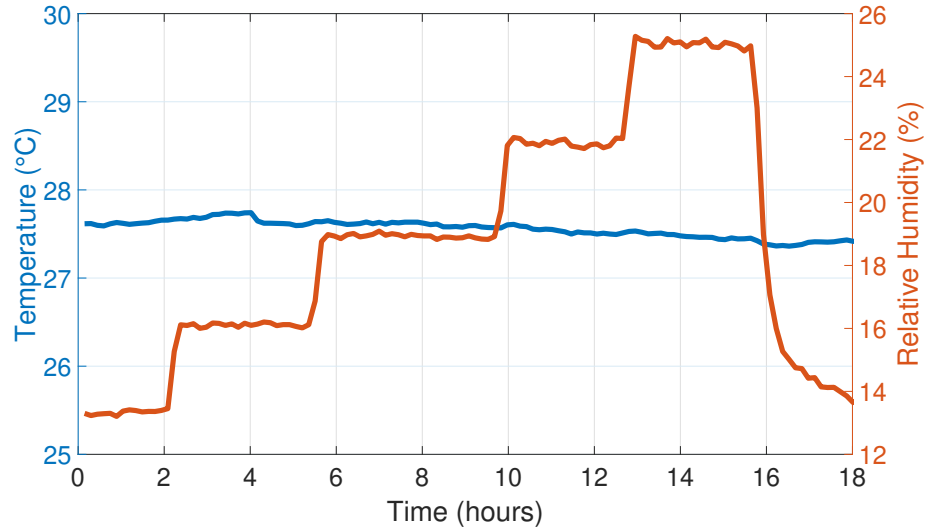


Figure 3.4 – Climatic chamber conditions during the RH test at constant temperature.

Figure 3.5 shows the frequency shift map as function of the distance at different RH stable steps, already temperature compensated with the bare fibre. As the optical fibres are all spliced, the distance corresponds to the sum of the consecutive individual lengths. For example, the first 100 metres correspond to the first fibre listed in Table 3.1 ^{III}.

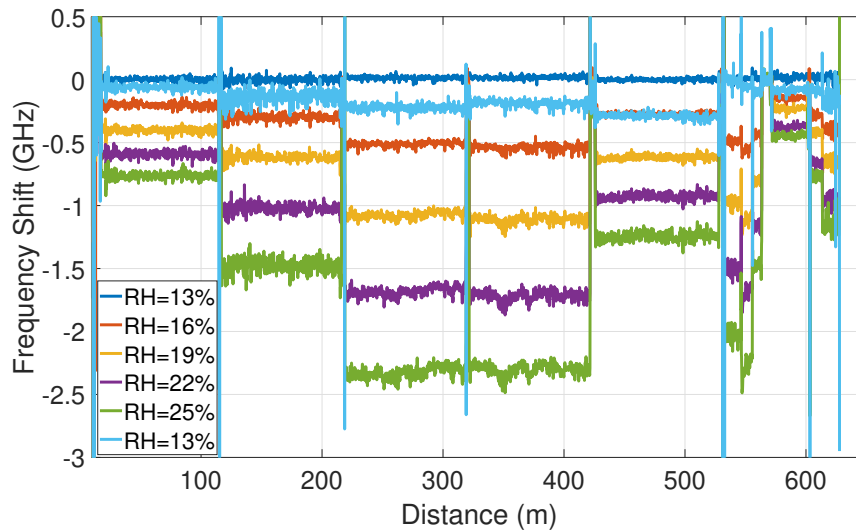


Figure 3.5 – Full ϕ -OTDR frequency shift of the FUT during the RH test at constant temperature.

^{III} The reason why the sum of the lengths in Table 3.1 is not the same of the total distance in Figure 3.5 is because some fibres were not considered in the data analysis due to their extremely unstable behaviour.

As expected, different fibres show different sensitivities, which can be attributed to the different coatings thicknesses and materials. Figure 3.6 shows the temporal variation of the polyimide-coated fibres.

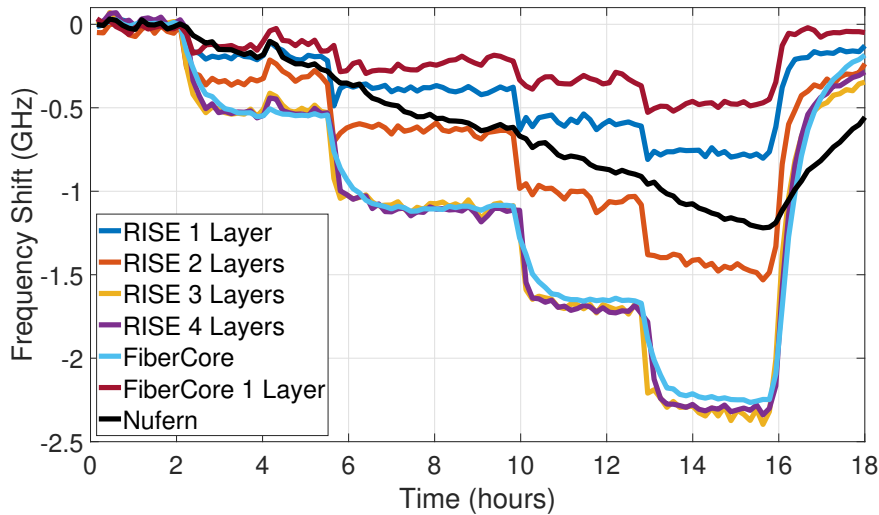


Figure 3.6 – Comparison of polyimide-coated fibres responses during the RH test at constant temperature.

Stacking layers of polyimide coating increases the fibre RH sensitivity, but the difference between 3 and 4 layers of coating in the RISE fibres is marginal. Then, the response of the commercial FiberCore fibre is extremely similar to the RISE with 3 and 4 layers due to the similar coating thickness. FiberCore fibre show an excellent behaviour in terms of stability and sensitivity, but show a slower response than the RISE fibres, expressed by the lowest slope in the transient moments. On the other hand, no hysteresis was noticed for the FiberCore fibres, while the RISE fibres showed some hysteresis. The pure silica fibre from Nufern is significantly slower and as it was not possible to achieve stabilization after reasonable waiting times, possibly due to an extra layer of coating that is not specified by the manufacturer. Its results will not be considered in the analysis.

In order to find the RH sensitivity of each fibre, the frequency shift is plotted as a function of the RH measured by the electronic sensors. The slope of the linear regression gives the RH sensitivity. Figure 3.7 presents the respective RH calibration plot of the polyimide-coated fibres and Table 3.2 summaries the RH sensitivities with the respective standard errors and coefficient of determination (R^2).

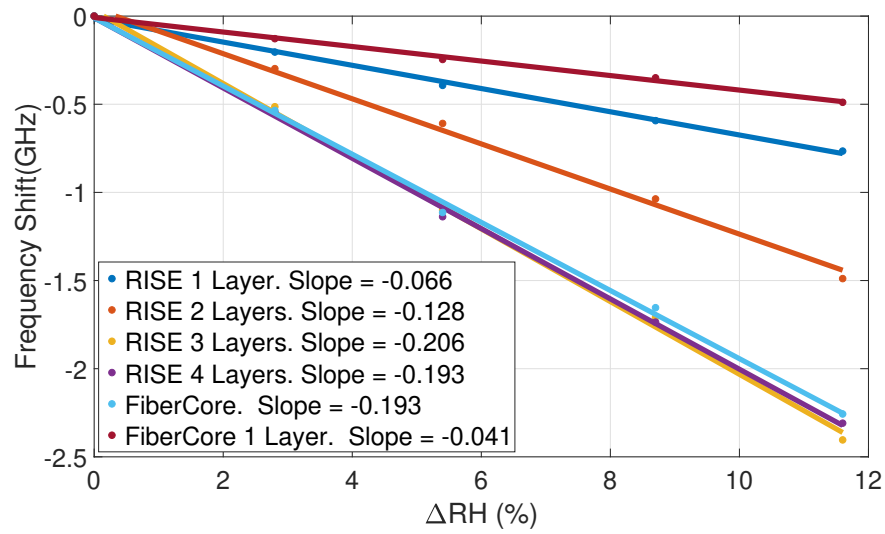


Figure 3.7 – RH calibrations of polyimide-coated fibres.

Table 3.2 – RH sensitivities comparison with the respective standard errors and R^2 .

Fibre	S_{RH} (MHz/%RH)	R^2
RISE 1 Layer	66 ± 2	0.9987
RISE 2 Layers	128 ± 5	0.9949
RISE 3 Layers	206 ± 5	0.9980
RISE 4 Layers	199 ± 4	0.9999
FiberCore	193 ± 5	0.9983
FiberCore 1 Layer	41 ± 2	0.9958

All the tested fibres present linear behaviour, with standard errors in the order of few MHz and R^2 always higher than 0.99. The difference between the RH sensitivity of the RISE optical fibre with 3 and 4 layers of coating may indicate that there is an estimation error either in the number of layers or in the thickness of each layer. This issue will be addressed in the next section.

The second part of the analysis is devoted to the response of the acrylate-coated fibre and Figure 3.8 shows its temporal response during the RH test at constant temperature. Figure 3.9 shows the respective RH calibration.

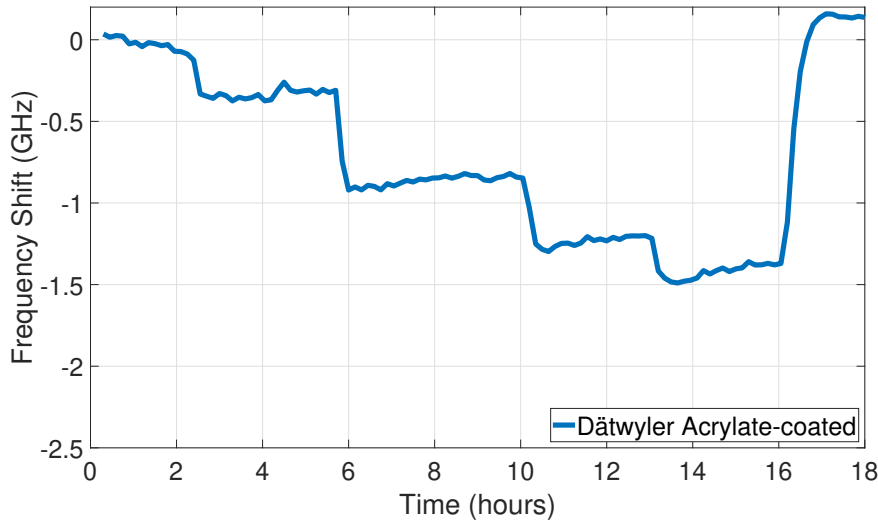


Figure 3.8 – Acrylate-coated fibres response during the RH test at constant temperature.

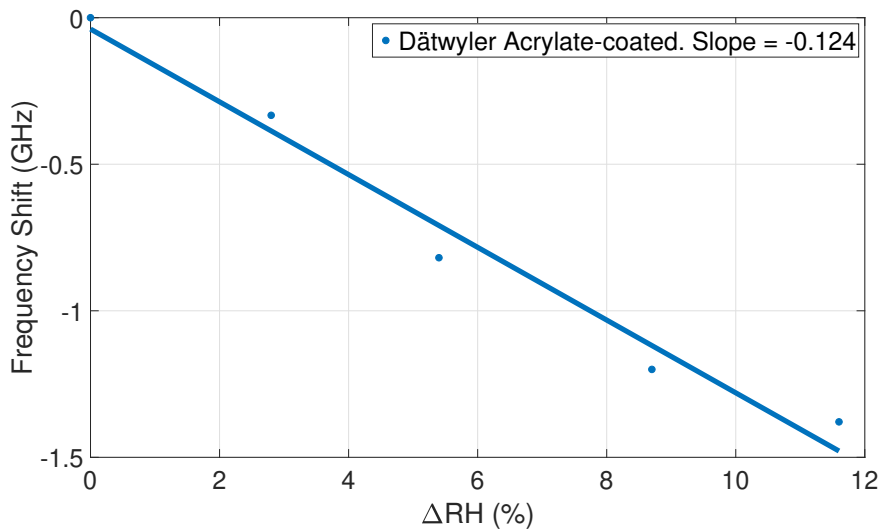


Figure 3.9 – RH calibration of the acrylate-coated fibre.

The Dätwyler acrylate-coated fibre response is significantly sensitive to RH, with a RH sensitivity of 124 ± 11 MHz/%RH, and, at the same time, is the fastest to respond but with a unstable behaviour.

Due to the climatic chamber limitation of changing RH less than 1%, the measurement resolution is estimated from the standard deviation. If the humidity variation is higher than the double of the standard deviation, it is assumed that this system can resolve it. The RH resolution is different from fibre to fibre but, generally, the system can resolve from 0.1% RH, with the more RH sensitive optical fibres such as the RISE with 3 and 4 layers or the FiberCore, to 1% RH, with the less RH sensitive optical fibre as the RISE or FiberCore with 1 layer.

Finally, a piece of 100 metres of polyimide-coated fibre (RISE 1 Layer) was spliced to a 10 kilometres standard acrylate-coated fibre spool, the latter being placed outside the climatic chamber, and a simple one-step RH test was carried out. The long fibre was placed outside the chamber purposely to make it subject to conditions different to the fibre test sample. Figure 3.10 shows the frequency shift as function of the distance during the one-step RH test and Figure 3.11 zooms onto the last part of the plot, i.e. the distance in excess of 10 kilometres.

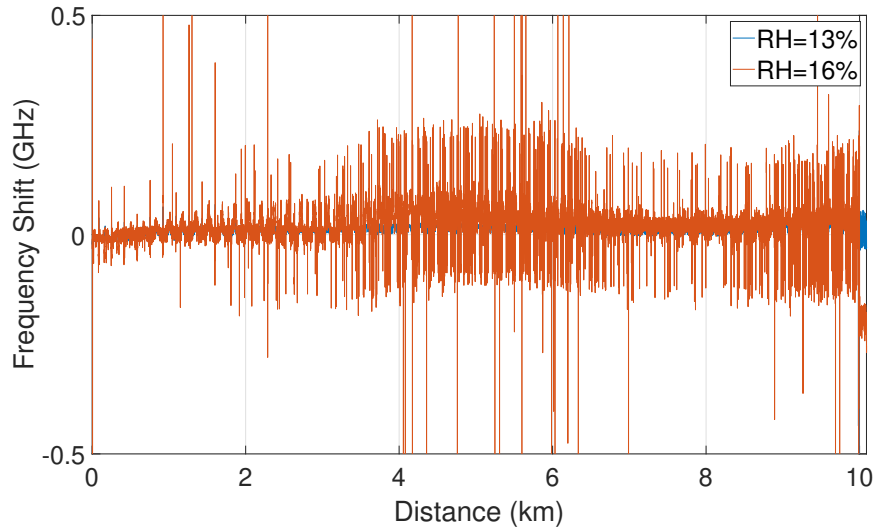


Figure 3.10 – Frequency shift of the 10 kilometres fibre spliced with 100 metres of polyimide-coated fibre.

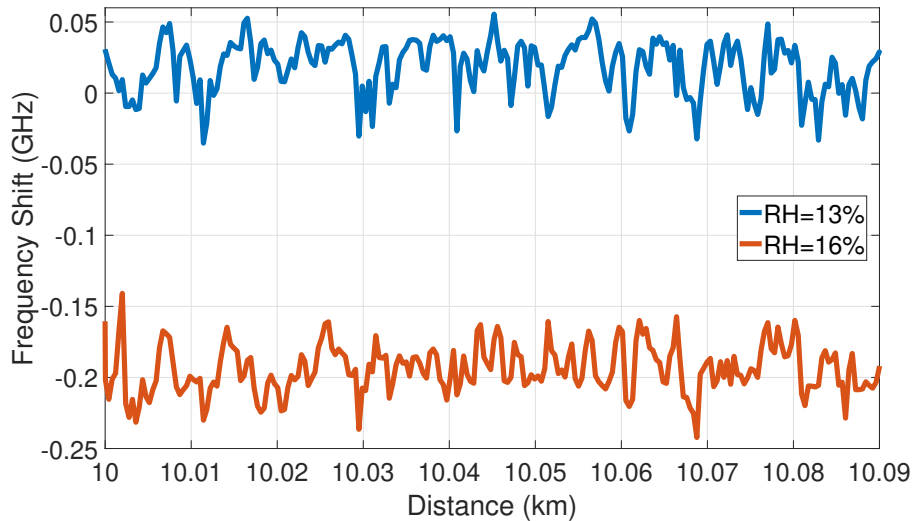


Figure 3.11 – Zoom of the last part of the frequency shift plot after 10 kilometres.

The random and noisy variations in Figure 3.10 are likely due to the uncontrolled environment of the 10 kilometres fibre spool. The response of the polyimide-coated fibre is clearly

shifted when the RH passed from 13% to 16%, meaning that the system is still able to detect this RH variation without significant penalty after 10 kilometres length.

3.1.3 Conclusions

The first conclusion of this section is that the proof-of-concept of a highly sensitive RH distributed fibre sensor using a ϕ -OTDR setup with kilometres of sensing range was successfully achieved. The developed system can monitor fibres up to 10 kilometres with 70 centimetres of spatial resolution with a measurement resolution of 0.1% of RH if using one of the more RH sensitive optical fibres such as RISE with 3 and 4 layers or FiberCore. This configuration is highly compatible with a systematic study of different coatings under identical conditions by appending different fibre segments and interrogating them simultaneously in a single acquisition. Second, after comparing different optical fibre coatings, the conclusion is that if the requirements are a fast response time and short settling time at room temperature, the standard acrylate-coated fibres are the best candidates. However, if the requirements are high sensitivity with low hysteresis the polyimide-coated fibres offer advantages.

These results obtained at 25°C motivated the next test with the same kinds of coated optical fibres but in a larger range of temperatures, including temperatures lower than 0°C, as the LHC requires.

3.2 Humidity Effect on Acrylate- and Polyimide-Coated Fibres

The objective of this study is to investigate precisely and in-depth the RH effect on acrylate- and polyimide-coated fibres at different temperatures, and to quantify the cross-sensitivity to RH and temperature in different environmental conditions. Several RH tests with compressed dry air were performed at different temperatures from -20°C to 50°C and a temperature and a RH test were also performed in a saturated Carbon Dioxide (CO₂) environment.

The objective of testing the fibres in two different environments is justified because one possible location to install the developed RH distributed fibre sensor is inside the silicon trackers of the main LHC detectors, ATLAS and CMS. Both detectors are cooled-down with a CO₂ refrigerating system that includes several metres of tubes and capillaries spread inside the detectors [91]. The distributed RH sensor will be close to some of those capillaries and its temperature and RH sensitivities should also be evaluated in a CO₂ environment to understand its behaviour in case of a CO₂ leak.

3.2.1 Experimental Setup

The new set of tests was performed in a climatic chamber developed at CERN and specially prepared to work at very low RH with a resolution of 0.1% of RH. The range of temperatures varies from -20°C to 50°C. A photo of the climatic chamber setup can be seen in Figure 3.12.

Figure 3.13 shows the full schematic of the climatic chamber.

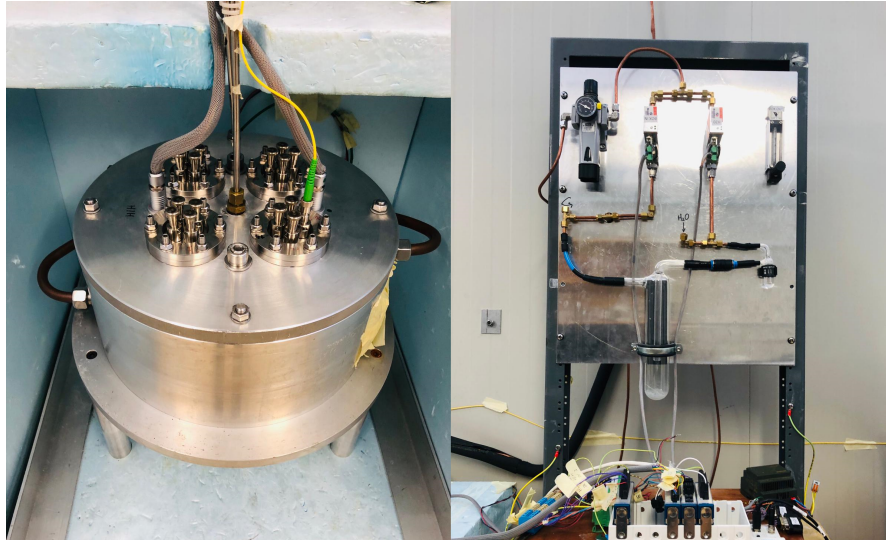


Figure 3.12 – Photos of climatic chamber and pneumatic circuit.

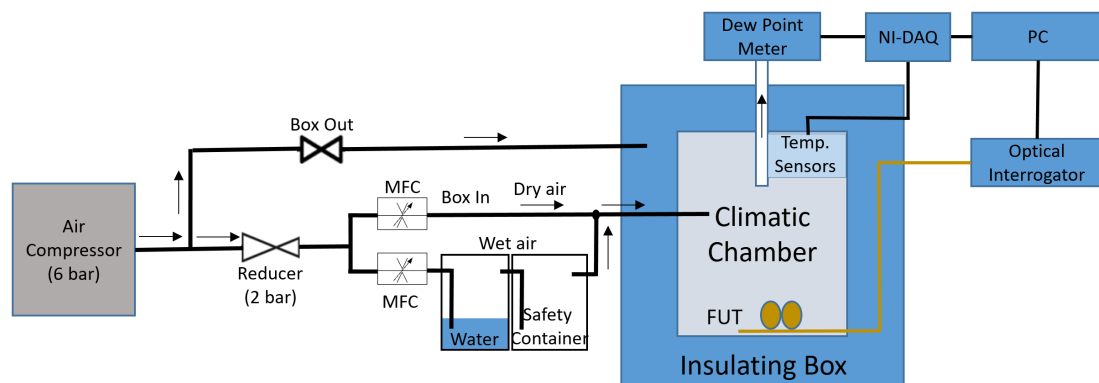


Figure 3.13 – Schematic of the climatic chamber including the pneumatic circuit and the electronic data acquisition system. MFC - Mass Flow Controller.

The temperature control is performed with a refrigerated-heating circulator (Julabo FP-50), while the RH control is ensured by a pneumatic circuit that mixes dry and wet air flows. Different combinations of both flows create different levels of humidity and they are controlled by two electronic Mass Flow Controllers (MFC) (Bronkhorst El-Flow). The connection with the exterior is done through high-vacuum feedthrough connectors for both optical fibres and copper wires, which enables a stable control over the humidity level in the chamber below a dew point of -60°C . The climatic chamber allows precisely controlling the RH from 0 up to 90% and can be monitored and controlled remotely. As reference RH sensor, a Chilled Mirror Dew Point Hygrometer (EdgeTech DewMaster) was used, while three calibrated resistance thermometers (PT100) were used for temperature reference. LabVIEW software makes the

interface between the National Instruments Data Acquisition Module (NI-DAQ), where all the reference sensors are connected, and the PC.

Optical Interrogator

At the time of the test, the home-made ϕ -OTDR used in the previous study was not available at CERN. Therefore, a compact and easily transportable CP- ϕ -OTDR interrogator^{IV} was used in the new tests. The fundamentals of the CP- ϕ -OTDR interrogator are explained in Section 2.2.1. Figure 3.14 shows the full schematic and a detailed description can be found in [65].

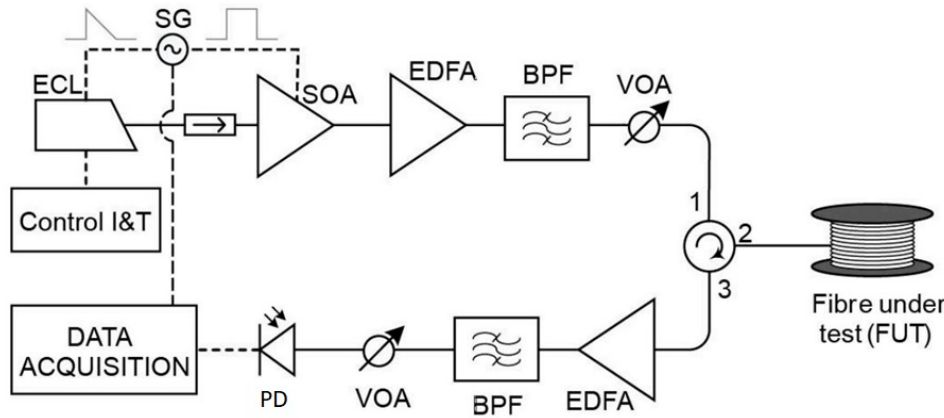


Figure 3.14 – Schematic of a CP- ϕ -OTDR interrogator [65]. ECL - External Cavity Laser. SG - Signal Generator. SOA - Semiconductor Optical Amplifier. EDFA - Erbium-Doped Fibre Amplifier. BPF - Band Pass Filters. VOA - Variable Optical Attenuator. PD - PhotoDetector.

An External Cavity Laser (ECL) emits monochromatic CW light that is shaped into an optical pulse by an SOA. The SOA is synchronized with the ECL driver and the output signal power is amplified by an EDFA. The resulting probe is injected into the FUT through an optical circulator and the backscattering signal is amplified before the PD. Two VOAs are placed before the FUT and before the PD, the first to prevent non-linear effects caused by an intense optical pulse and the second to avoid the PD power saturation limit. Two Band Pass Filters (BPF) are used to reduce the EDFA spontaneous emission. For this test, the spatial resolution was set to 6 metres and the sensitivity is below 1 MHz, which corresponds to approximately 1 mK of temperature shift. Using this configuration, the setup monitored the FUTs listed in Table 3.3.

Standard acrylate coated optical fibres are the most widely used optical fibres in the telecommunications industry, but also in sensing applications. In this section, two samples from different manufacturers were studied. Fibre AC1 is a Dätwyler acrylate-coated drawn in the 2000's while AC2 is a Cabloptic acrylate-coated drawn in the 1990's. All of these fibres have

^{IV} Provided by Dpto. de Electrónica, Universidad de Alcalá, Madrid, Spain

been spliced and arranged on a single FUT, and are coiled in stress-free holder, as shown in Figure 3.15. The FUT was subject to a temperature test at constant RH and six RH tests at constant pre-set temperatures. The first set of tests was performed with normal compressed dry air, while the second was carried out with CO₂.

Table 3.3 – List of FUT and respective coating characteristics and lengths.

Fibre	Coating	Coating Thickness (μm)	Length (m)
AC1	Acrylate	62.5	800
AC2	Acrylate	62.5	300
PI	Polyimide	15	25
Bare	-	-	40

- Not applicable

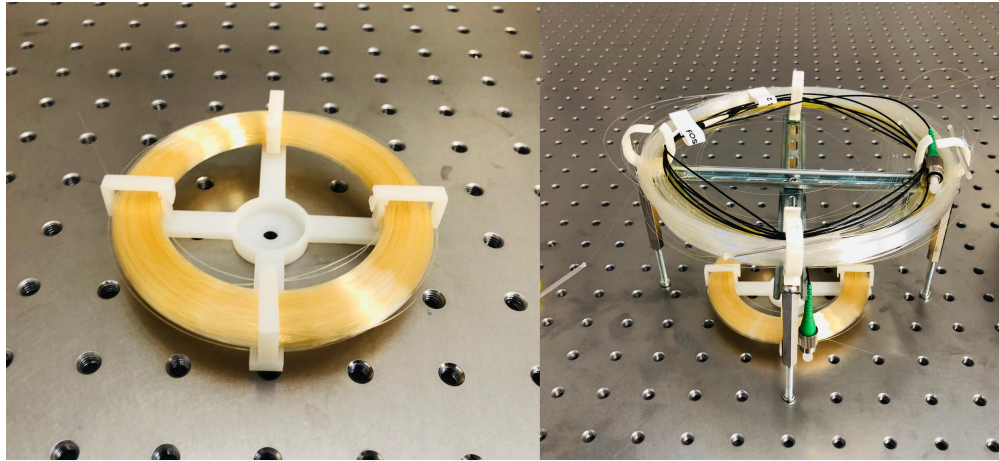


Figure 3.15 – Optical fibres rolled in the strain-free holders.

3.2.2 Experimental Results

Temperature characterization with compressed air

The experimental procedure started with a temperature characterization from -20°C to 25°C at approximately constant RH ($\approx 32\%$), as shown in Figure 3.16. The temperature reference is the average of the three temperature reference sensors. The frequency shifts of all fibres during the temperature test are grouped in Figure 3.17 and the respective temperature calibrations are represented in Figure 3.18.

Analysing the results, the temperature sensitivity (S_T) of both acrylate-coated fibres is constant to a very good approximation in the observed temperature range and nearly the same, of 1.55 and 1.52 GHz/K respectively, but it is significantly higher than the polyimide-coated fibre showing 1.29 GHz/K. These differences are related to the thermal expansion coefficient of the specific coatings and their thickness. The acrylate-coated fibres have a

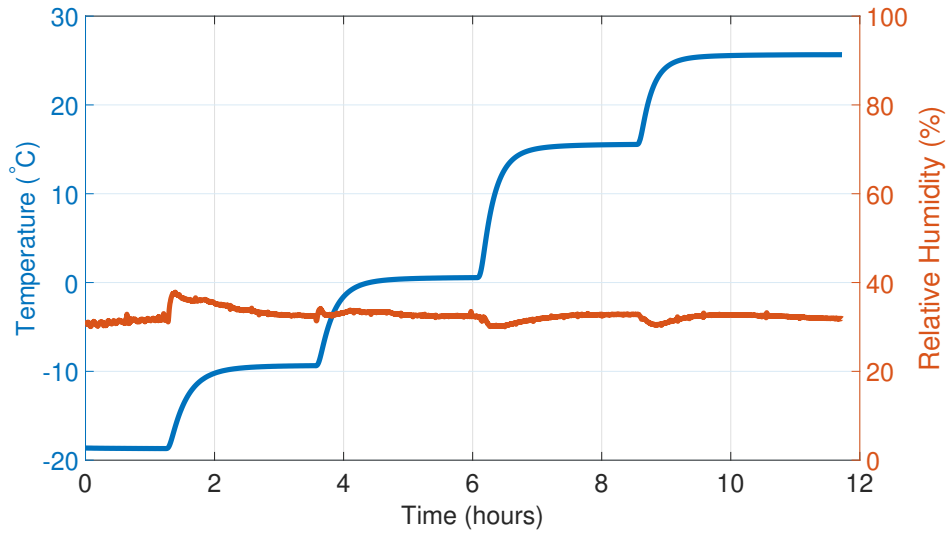


Figure 3.16 – Climatic chamber conditions during the temperature test at constant RH.

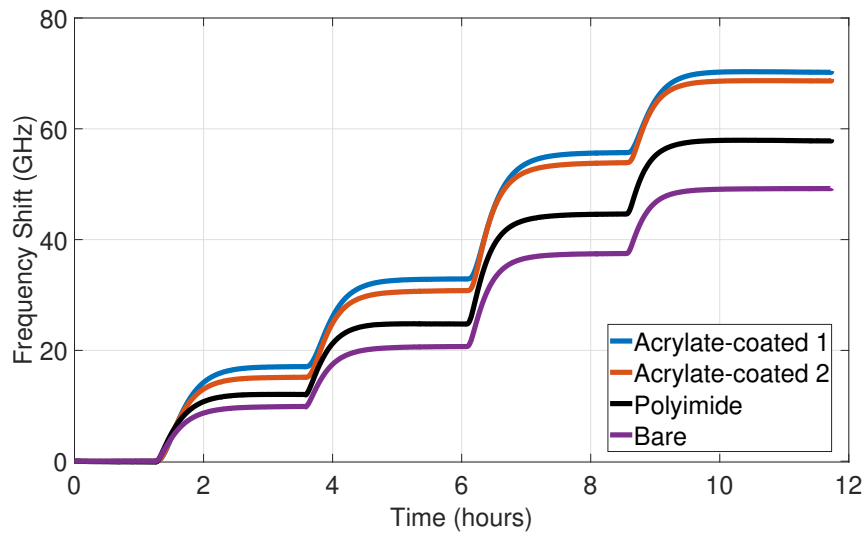


Figure 3.17 – Frequency shift of all fibres during the temperature test at constant RH.

coating diameter of $\approx 60 \mu\text{m}$, while the polyimide coating is thinner down to $\approx 15 \mu\text{m}$.

The bare fibre shows the lowest temperature sensitivity of 1.091 GHz/K and this can be considered as the plain response of silica. Table 3.4 summarizes the temperature sensitivities and the respective standard errors and coefficients of determination (R^2).

The acrylate-coated fibres show higher sensitivity errors with a slight deviation from the perfect linear behaviour, expressed by the lower R^2 . Nevertheless, they can be considered linear and the sensitivity errors of the coated fibres are of the order of tens of MHz/K , while

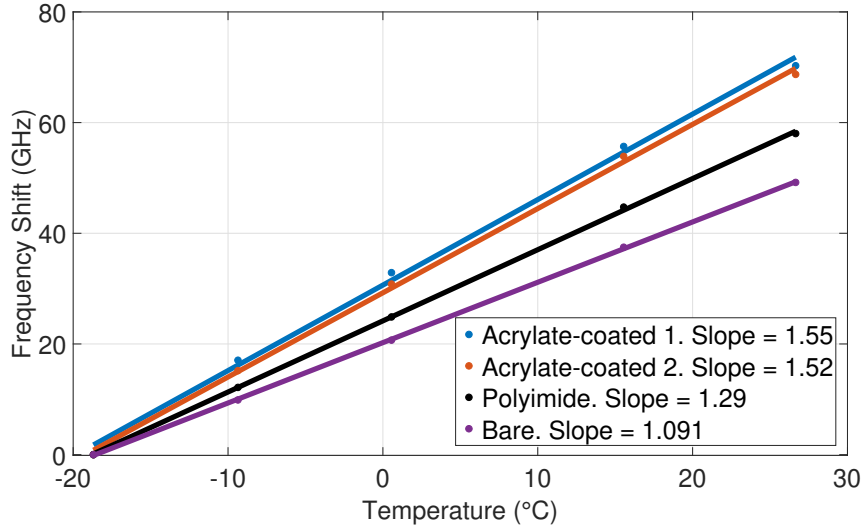


Figure 3.18 – Temperature calibration fittings of all fibres.

Table 3.4 – Temperature sensitivities comparison.

Fibre	S_T (GHz/K)	R^2
AC1	1.55 ± 0.05	0.9971
AC2	1.52 ± 0.03	0.9989
PI	1.29 ± 0.01	0.9998
Bare	1.091 ± 0.006	0.9999

the bare fibre shows one order of magnitude lower, in the order of few MHz/K.

After the temperature calibration at constant RH, a RH test at six preset constant temperatures (-20°C, -10°C, 0°C, 15°C, 25°C and 50°C) was carried out.

Temperature compensation method

The RH calibration is performed after applying a temperature compensation method to remove the residual temperature variation inside the climatic chamber. The total frequency shift (ΔF_{total}) measured for each fibre has a RH (ΔF_{RH}) and a temperature (ΔF_T) dependence.

$$\Delta F_{total} = \Delta F_{RH} + \Delta F_T \quad (3.1)$$

The temperature reference is given by the bare fibre (ΔF_{bare}), which is only sensitive to temperature but, as demonstrated in the previous test, the temperature sensitivity of the coated fibres is not the same as the bare fibre. For that reason, on top of the bare fibre

frequency shift, a corrective factor should be applied to correct the temperature compensation method. All fibres have linear temperature sensitivities, which means that a ratio between the 2 temperature sensitivities is enough to correct the measurement.

$$\Delta F_{RH} = \Delta F_{total} - \left(\frac{S_{T_{fibre}}}{S_{T_{bare}}} \times \Delta F_{bare} \right) \quad (3.2)$$

where $S_{T_{fibre}}$ and $S_{T_{bare}}$ are the temperature sensitivities of the selected fibre and bare fibre respectively. An example of this compensation method is given in Figure 3.19 that shows the response of an acrylate-coated fibre during a RH test.

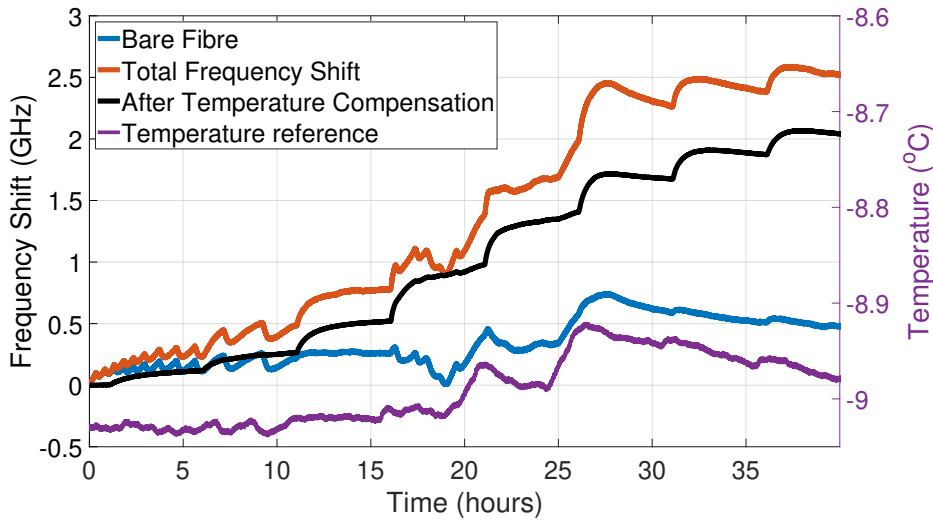


Figure 3.19 – Example of the temperature compensation method. The fibre total frequency shift is plotted in orange, the reference bare fibre in blue and the compensated trace in black. The temperature reference is plotted in purple.

At the beginning of the test, there was an intense fluctuation measured by the acrylate-coated and bare fibres. That is clearly a temperature fluctuation in the climatic chamber, as seen in the temperature reference plot, and it is visible that after applying the compensation method, the compensated signal is completely immune to these temperature variations, proving that the compensation method is valid.

RH characterization with compressed air

Figure 3.20 shows the climatic chamber conditions during the RH test at 25°C and Figure 3.21 illustrates the frequency shift of all tested fibres already temperature compensated.

Analysing Figure 3.21, where the temporal response of each fibre at 25°C is represented, the

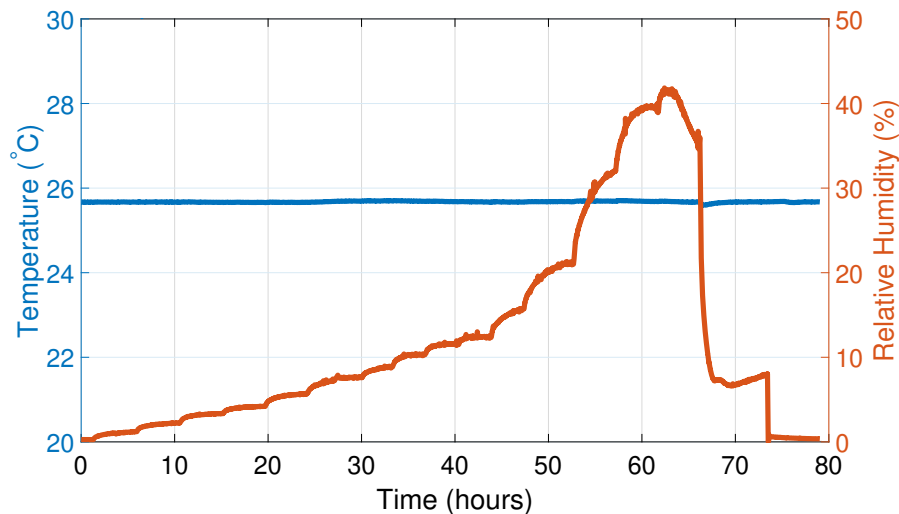


Figure 3.20 – Climatic chamber conditions during the RH test at 25°C.

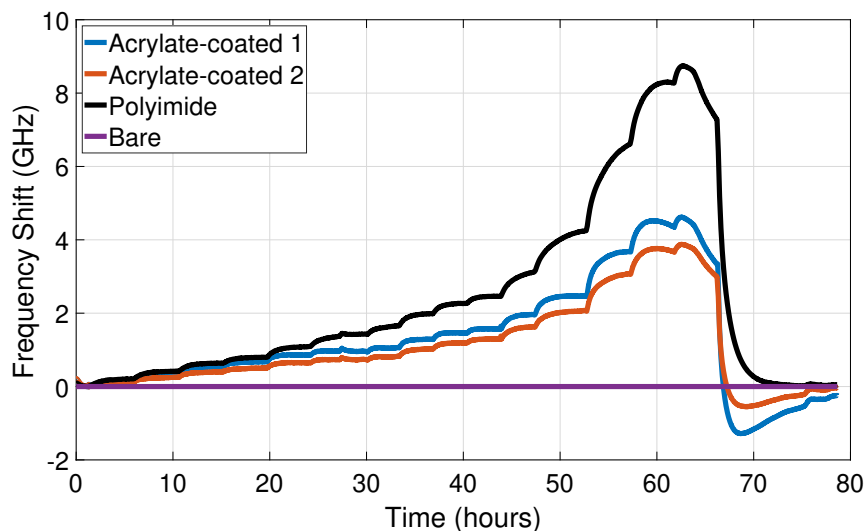


Figure 3.21 – Fibres frequency shift during a RH test at 25°C.

main observation is that all tested fibres follow perfectly the RH variation inside the climatic chamber, but showing different sensitivities. Figure 3.22 shows the RH calibration curves and the first observation is that the polyimide-coated fibre presents higher sensitivity to RH than the acrylate-coated fibres, as obtained in the previous Section 3.1. As observed in the temperature test, the differences are again due to the nature and thickness of the coating. The polyimide coating, even if thinner than the acrylate coating, shows higher RH sensitivity due to its higher hygroscopic capacity.

Table 3.5 summarizes the RH sensitivities of the acrylate-coated fibres at different tempera-

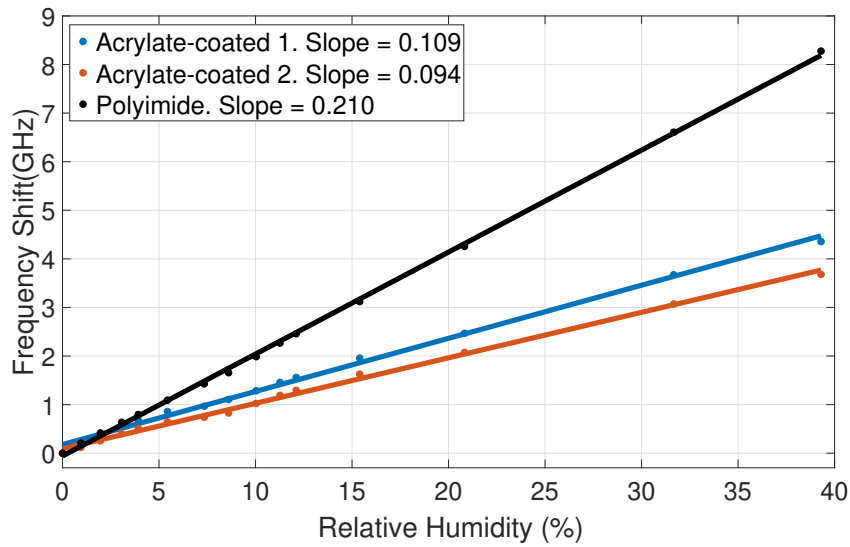


Figure 3.22 – RH calibration fittings of all fibres at 25°C.

tures while Table 3.6 shows the results of the polyimide-coated fibre. Figure 3.23 summarizes all the results in a single plot.

Table 3.5 – RH sensitivities of acrylate-coated fibres at different temperatures.

T (°C)	AC1		AC2	
	S_{RH} (MHz/%RH)	R^2	S_{RH} (MHz/%RH)	R^2
-20°C	217 ± 2	0.9991	130 ± 1	0.9994
-10°C	240 ± 6	0.9927	140 ± 11	0.9311
0°C	219 ± 4	0.9963	178 ± 2	0.9973
15°C	148 ± 2	0.9981	128 ± 1	0.9987
25°C	109 ± 2	0.9960	94 ± 1	0.9969
50°C	31 ± 6	0.9016	–	–

Table 3.6 – RH sensitivities of polyimide-coated fibre at different temperatures.

T (°C)	S_{RH} (MHz/%RH)	R^2
-20°C	194 ± 2	0.9987
-10°C	212 ± 2	0.9992
0°C	230 ± 2	0.9994
15°C	230 ± 1	0.9999
25°C	210 ± 1	0.9994
50°C	219 ± 5	0.9983

The first point to raise is the drastic temperature dependence of RH sensitivity for acrylate-coated fibres, probably as a result of a significant change of plasticity, while the RH sensitivity of polyimide-coated fibers does not vary more than 15% over the range of temperatures tested. Polyimide polymers are known for their stability over a large range of temperatures [88] and

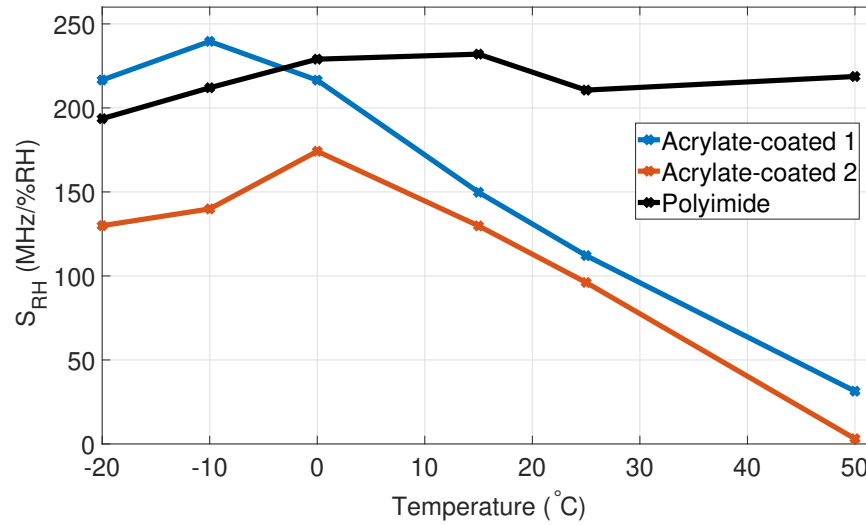


Figure 3.23 – RH Sensitivity at different temperatures of the acrylate- and polyimide-coated fibres.

this fact is confirmed in this study.

Considering for instance AC1 from 25°C to -20°C, the response varies by a factor of 2 and reaches its maximum sensitivity at -10°C. At 50°C, the RH sensitivity of AC1 is strongly decreased to $\approx 13\%$ of the RH sensitivity at -10°C and, at the same time, the linear behaviour is extremely affected by the acrylate thermal instability. On the other hand, at -10°C, its sensitivity is even higher than the maximum sensitivity of a polyimide-coated fibre. AC2 also shows similar behaviour to AC1 but the maximum is reached at 0°C. At 50°C, the RH sensitivity of this fibre is negligible and impossible to calibrate, while at -10°C it shows a higher sensitivity error mostly due to the long stabilization time. The sensitivity errors are all in the order of a few MHz/%RH.

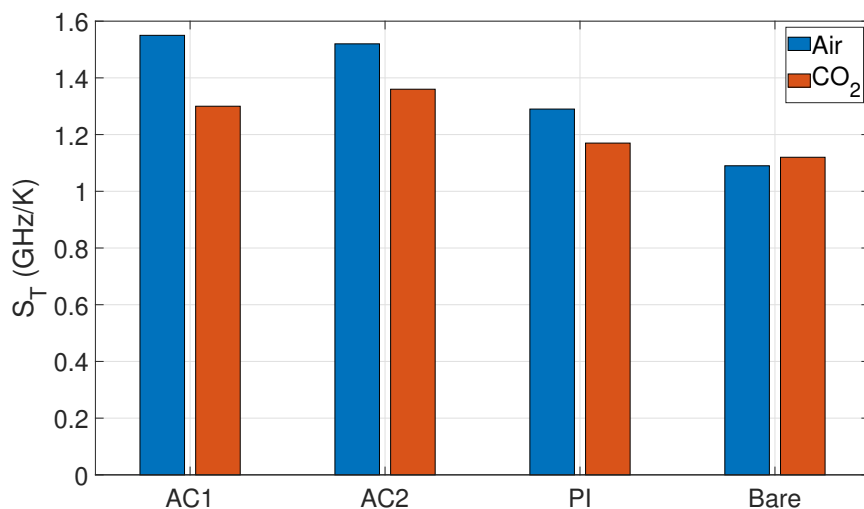
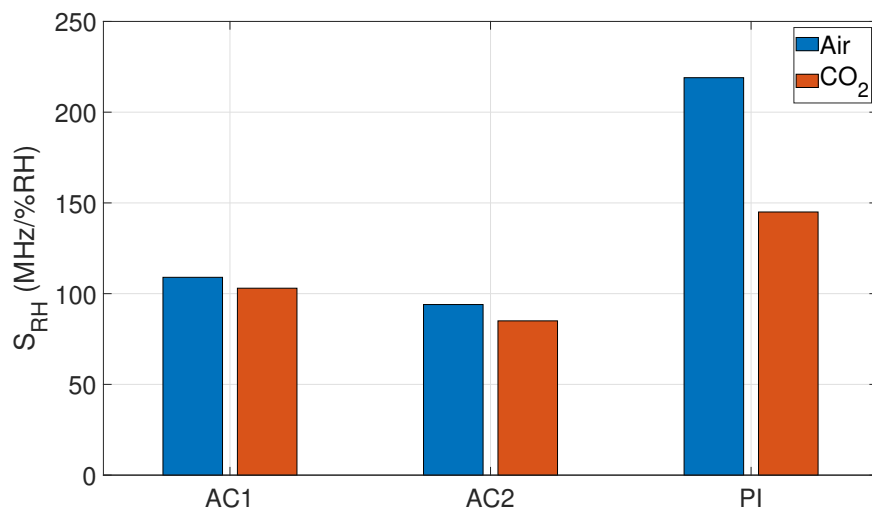
The interesting feature of acrylate-coated fibres is that the difference between two distinct commercial fibres is significant. The difference may indicate that the coatings may have different materials in its composition that are not specified by the manufacturer. For some given temperatures, for instance at -20°C, the AC1 shows a RH sensitivity 1.67 times higher than the AC2, which means that the RH sensitivities should be addressed individually and can not be considered similar to all standard acrylate-coated fibres.

Temperature and RH characterization with carbon dioxide

A temperature test from -20°C to 25°C at approximately constant RH ($\approx 30\%$) and then a RH test from 0% to 50% at 25°C were performed under pure CO₂ atmosphere. The results are summarized in Table 3.7. Figures 3.24 shows the differences in the temperature sensitivities while Figure 3.25 the differences in RH sensitivities under both environments.

Table 3.7 – Temperature and RH sensitivities under pure CO₂ atmosphere.

Fibre	S_T (GHz/K)	R^2	S_{RH} (MHz/%RH)	R^2
AC1	1.30 ± 0.01	0.9997	103 ± 2	0.9974
AC2	1.36 ± 0.01	0.9997	85 ± 2	0.9952
PI	1.17 ± 0.01	0.9997	145 ± 4	0.9933
Bare	1.12 ± 0.01	0.9998	–	–

Figure 3.24 – Comparison between the temperature sensitivities in air and CO₂.Figure 3.25 – Comparison between the RH sensitivities in air and CO₂.

The main observation is that the sensitivity of the bare fibre is not affected in a significant way from air to CO₂ due to the absence of coating, in contrast with the coated fibres. For the

coated fibres, the main conclusion is that the temperature sensitivity is significantly lowered by $\approx 16\%$, $\approx 11\%$ and $\approx 10\%$ for AC1, AC2 and PI, respectively. Regarding the RH sensitivities of the acrylate-coated fibres, the RH sensitivity decrease is $\approx 6\%$ and $\approx 10\%$ for AC1 and AC2 respectively, while the polyimide-coated fibre shows an even higher loss of sensitivity of $\approx 34\%$ with respect to the dry air tests. The significant attenuation in the polyimide-coated can indicate that this kind of polymer exhibits a high CO_2 permeability probably due to its very good gas transport properties [92].

The test carried out using pure CO_2 actually demonstrated that, depending on the composition of the surrounding atmosphere, the different equilibrium of water absorption in the coating can impact the response in a non-negligible way.

3.2.3 Sensitivities Comparison of Polyimide-coated Fibres

The last study of this section was divided in two parts. The first part was projected to analyse the influence of the number of coating layers in the temperature sensitivity of the RISE polyimide-coated fibres with 1, 2, 3 and 4 layers. The second part was based on the study of the stability of the polyimide-coated fibres RH sensitivity in the temperature range from -20 to 50°C . A CP- ϕ -OTDR interrogator was used in both analysis.

Temperature Sensitivity

A temperature characterization test from -20 to 25°C was performed at constant RH, as shown in Figure 3.16, and the variation of the temperature sensitivity of the RISE polyimide-coated fibres as function of the number of coating layers is presented in Figure 3.26.

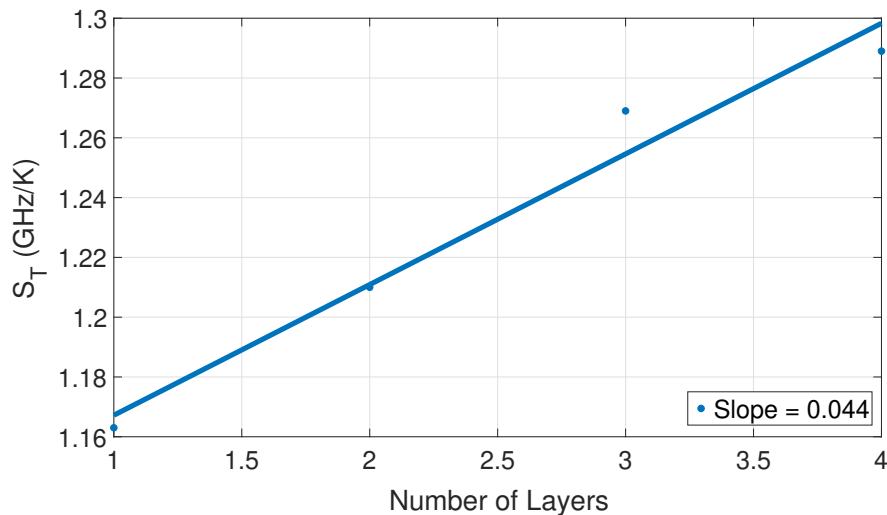


Figure 3.26 – Temperature sensitivity of polyimide-coated fibres as function of the number of layers.

The temperature sensitivity increases with the number of layers, in an almost linear approximation, with a variation of 44 ± 6 MHz/°C per number of coating layers. Nevertheless, it is clear that there is a deviation from a linear behaviour, expressed by the lower R^2 of 0.9683. Possibly, there is an estimation error of the coating layers thickness and, either the total thickness of the fibre with 3 layers is underestimated or the thickness of the fibre with 4 layers is overestimated.

Relative Humidity Sensitivity

The FUT, including the FiberCore polyimide-coated fibres, was afterwards submitted to RH tests at 6 preset temperatures (-20, -10, 0, 15, 25 and 50°C) and Figure 3.27 summarizes the RH sensitivities of all fibres at those preset temperatures.

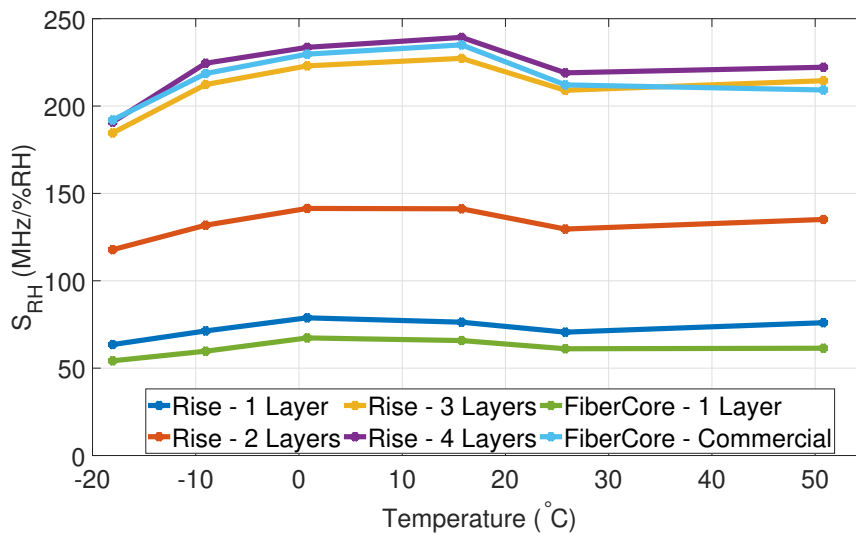


Figure 3.27 – Comparison between the RH sensitivities of all polyimide-coated fibres.

The first observation is that the RH sensitivity of all polyimide-coated fibres does not change significantly in the range of temperatures between -20 and 50°C. For the fibres with only 1 coating layer, this variation is even less significant and the RH sensitivity can be considered constant in the full range of temperature. One important note is that the difference between 3 and 4 layers of polyimide coating is not significant and can indicate, again, that there is an error in the coating thicknesses estimation for one of the two fibres. The results of the FiberCore commercial polyimide fibre are in between the fibre with 3 and 4 layers, which indicates that the commercial fibres have practically the same RH sensitivity and may have the same number of coating layers.

The main conclusion of this study is the confirmation that the polyimide-coated fibres are the best candidates for the RH sensing fibre showing a good and stable RH sensitivity in a large range of temperatures.

3.3 Mathematical Model

The last section of this chapter presents the mathematical model used to validate the experimental results of the polyimide-coated fibres.

A coated optical fibre can be modelled as a infinite sequence of coated FBGs that, at the same time, can be modelled as a infinitely long bi-material rod in which the two materials (coating and silica optical fibre) adhere perfectly. In an equilibrium status, the axial stress forces (σ) in the materials are balanced and the axial deformations of the fibre, ΔL_f , and coating, ΔL_c , are equal [28]:

$$\sigma_f A_f + \sigma_c A_c = 0 \quad (3.3)$$

where A_f and A_c are the cross-sectional areas of the fibre and coating, respectively.

$$\Delta L_f = \Delta L_c \quad (3.4)$$

For this study, we consider the polyimide-coated fibres because the material properties are better known than the acrylate coating. Assuming that the polyimide and silica are linear, elastic and isotropic, the strain (ϵ_z) in the materials is given by:

$$\epsilon_z = \sigma_c / E_c \quad (3.5)$$

$$\epsilon_z = \sigma_f / E_f \quad (3.6)$$

where E_c and E_f are the Young's modulus of the coating and fibre respectively. From now, the parameters A_c and E_c will be designated A_p and E_p , where p means polyimide. Assuming all the conditions previously mentioned, the strain induced into the fibre's core by RH and temperature is given by [93, 94]:

$$\epsilon_{RH} = \frac{A_p E_p}{A_p E_p + A_f E_f} (\beta_p - \beta_f) \times \Delta RH \quad (3.7)$$

$$\varepsilon_T = \frac{A_p E_p}{A_p E_p + A_f E_f} (\alpha_p - \alpha_f) \times \Delta T \quad (3.8)$$

where β_p and β_f are the constant coefficients of hygroscopic expansion of the polyimide coating and of the fibre, respectively. α_p and α_f are the Coefficient of Thermal Expansion (CTE) of the polyimide and fibre, respectively. The physical parameters of both materials can be found in [95] but the most important are summarized in Table 3.8.

Table 3.8 – Physical parameters of polyimide and silica optical fibres.

Parameter	Silica	Polyimide
Young's modulus, E (GPa)	73	2.5
Moisture expansion coefficient β (%RH ⁻¹)	0	7.0E-5
Temperature expansion coefficient, α (K ⁻¹)	5.5E-7	4.0E-5

The model built in this section will be applied to the polyimide-coated fibres with 1, 2, 3 and 4 layers of coating manufactured by RISE. According to the manufacturer, each layer has 4 μm of thickness. The coating layers were deposited on top of a standard 9/125 μm core/cladding silica optical fibre.

3.3.1 Relative Humidity Model

The first thing to take into consideration is that the precise values of the parameters are unknown and not provided by the manufacturers. Additionally, the Young's modulus of silica fibres can be affected by the dopant concentration, and that is one more unknown parameter [96]. Therefore, based on those uncertainties, Table 3.9 presents the range of values in which each parameter can vary^V.

Table 3.9 – Range of parameters values for polyimide-coated optical fibres.

Parameter	Minimum	Maximum
Young's modulus of fibre, E_f (GPa)	70	75
Young's modulus of polyimide, E_p (GPa)	2.5	3.5
Moisture expansion coefficient of polyimide, β_p (%RH ⁻¹)	7.0E-7	8.0E-7

In order to find the correct parameters for this specific polyimide-coated fibre, a new algorithm was built to compute the previous equations for different parameters combinations. The results give the range of possible theoretical values. Comparing these results with the response of the polyimide-coated fibre with 1 layer of coating in a general RH test at constant temperature, as shown in Figure 3.28, one can predict the real parameters by finding which theoretical value is closer to the experimental data.

^VThe choice of the range was based on the different values found in literature.

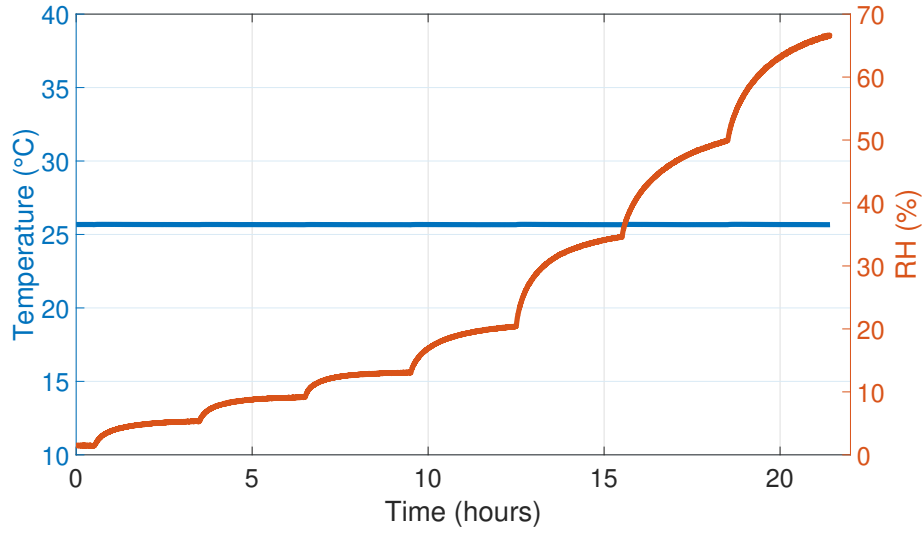


Figure 3.28 – RH and temperature in the climatic chamber during the test.

The experimental results in GHz can be converted into strain, ϵ , using the RH sensitivity ($1.3 \mu\epsilon/\%RH$) found in literature for a polyimide-coated fibre with $15 \mu m$ of thickness [97, 27]. Additionally, the experimental results can also be directly converted into strain units, by dividing the frequency shift measured in the fibre by the results obtained by the model.

The closest theoretical set of parameters is evaluated using the Mean Squared Error (MSE) equation that calculates point by point the difference between the experimental and the theoretical data.

$$MSE = \frac{1}{n} \sum_{i=1}^n (y_i - \tilde{y}_i)^2 \quad (3.9)$$

where n is the number of evaluated points and y_i and \tilde{y}_i the theoretical and experimental values, respectively.

Figure 3.29 shows the parameters' range together with the experimental data of polyimide-coated fibre with 1 layer of coating and best theoretical expected. Table 3.10 presents the best parameters that will be used further in the RH model.

Table 3.10 – Best parameters for modelling the polyimide-coated fibres.

Parameter	Best
Young's modulus of fibre, E_f (GPa)	71
Young's modulus of polyimide, E_p (GPa)	3.5
Moisture expansion coefficient of polyimide, $\beta_p(\%RH^{-1})$	$8.0E-7$

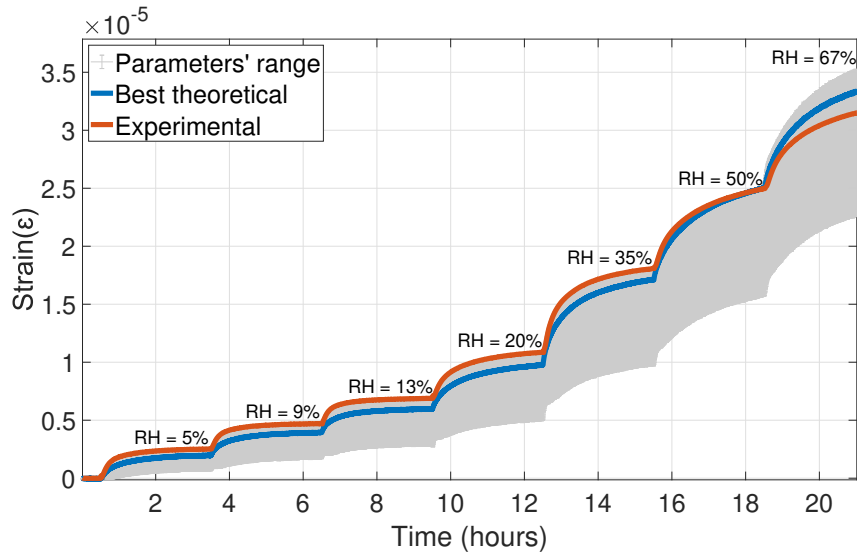


Figure 3.29 – Comparison between the experimental data of polyimide-coated fibre with 1 layer of coating and the range of theoretical expected data.

The comparison between the experimental and the theoretical should be analysed carefully. Even if the experimental data fits inside the error margin, there are factors to take into consideration. First of all, the imperfect adhesion between the polyimide coating and the silica fibre can induce some differences because part of the absorbed humidity will not have the same effect in the fibre's core as if the adhesion was perfect. The silica Young's modulus also changes significantly when a coating is applied [98]. Then, the structure of the polyimide coating is not perfectly homogeneous and will have oscillations in the concentration and thickness. Finally, the water absorption capacity of the polyimide, but also its Young's modulus, can change with a temperature or RH variation [99].

All those factors are not considered in the model and can explain some errors in the comparison between the experimental and the theoretical data. Nevertheless, the experimental results for the fibre with 1 layer of polyimide coating fit the theoretical calculations.

Using the set of parameters listed in Table 3.10, the model was afterwards applied to the fibres with 2, 3 and 4 layers of polyimide coating. Figure 3.30 shows the results for the polyimide-coated fibre with 2 layers of coating.

The first observation is that the experimental data match well with the theoretical data up to approximately 35% of RH. After that, the experimental values are slightly lower than the theoretical ones. This can be explained by the fact that stacking layers of polyimide does not produce the same effect as only one layer with a thickness equal to the sum of the individuals [100]. There will be some imperfections between the layers and some water molecules will be trapped in the structure gaps and will not have the same effect on the optical fibre as if it were a perfect diffusion process. At the same time, the polymer starts to lose some

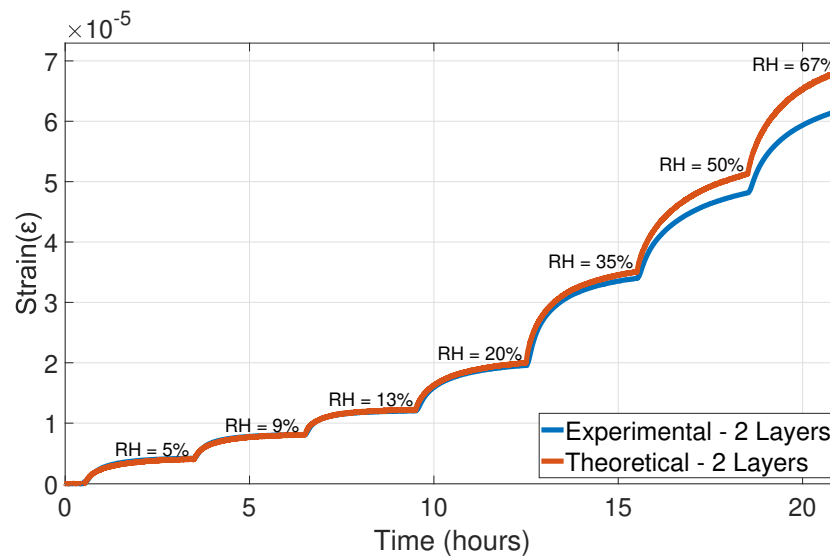


Figure 3.30 – Comparison between the RH experimental data of 2 layers of polyimide and the theoretical expected data.

absorption capability at higher RH values because it is closer to the saturation level. In this situation, the absorption is reduced and the experimental data is naturally lower than the ideal conditions.

The optical fibre with 3 layers of polyimide coating presents similar results, as shown in Figure 3.31.

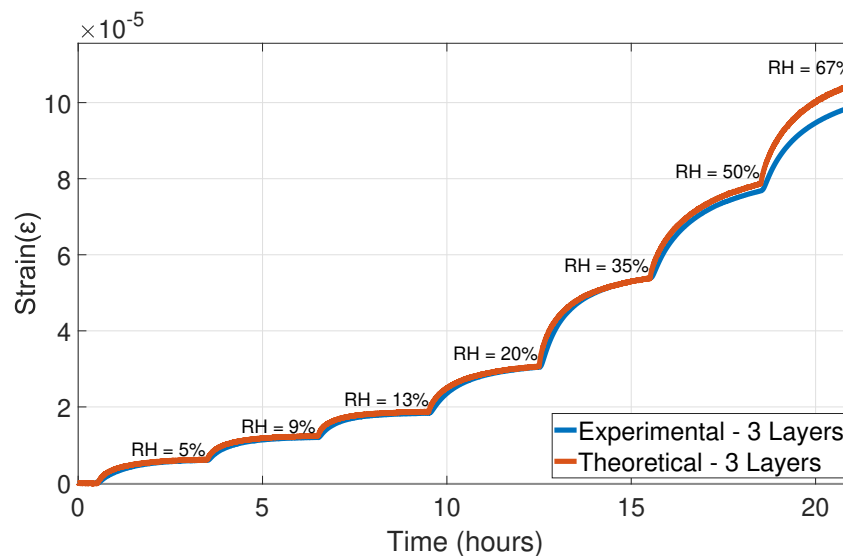


Figure 3.31 – Comparison between the experimental data of 3 layers of polyimide and the theoretical expected data.

There is an good prediction up to 50% of RH and a slight difference at higher RH values.

Finally, the model for the polyimide-coated fibre with 4 layers of coating has significant differences, as seen in Figure 3.32.

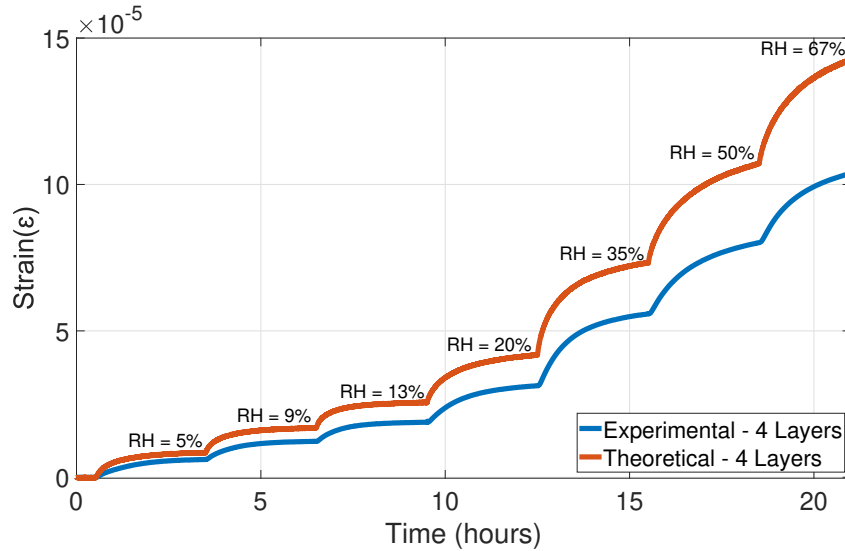


Figure 3.32 – Comparison between the experimental data of 4 layers of polyimide and the theoretical expected data.

The experimental results are significantly lower, specially at high RH values, than the theoretical model and this can be explained by a possible error in the coating thickness calculation, as it was indicated in the previous Section 3.2.3. The RH sensitivity of the fibre with 2 layers of coating is 80% higher than the RH sensitivity of 1 layer, while the sensitivity of the 3 layers is 60% higher than the sensitivity of 2 layers. On the other hand, the difference between the sensitivities of the fibres with 3 and of 4 layers of coating is extremely low, in the order of 5%. This indicates clearly that the coating thickness of the fibre with 4 layers is probably lower than what is specified by the manufacturer.

3.3.2 Temperature Model

After modelling the RH impact on polyimide-coated fibres at constant temperature, the next study is to model the temperature effect at constant RH. The RH measured in the climatic chamber during the test is plotted in Figure 3.33.

The temperature model uses the same parameters for the polyimide-coated fibres obtained in the previous section but two more should be taken into consideration: the temperature expansion coefficient of the polyimide and of the fibre [101]. A similar exercise was performed to determine the best parameters for this fibre, and the range of values is expressed in Table 3.11.

After running the algorithm, Figure 3.34 shows the data from the fibre with 1 layer of polyimide coating, the theoretical data and the uncertainty range.

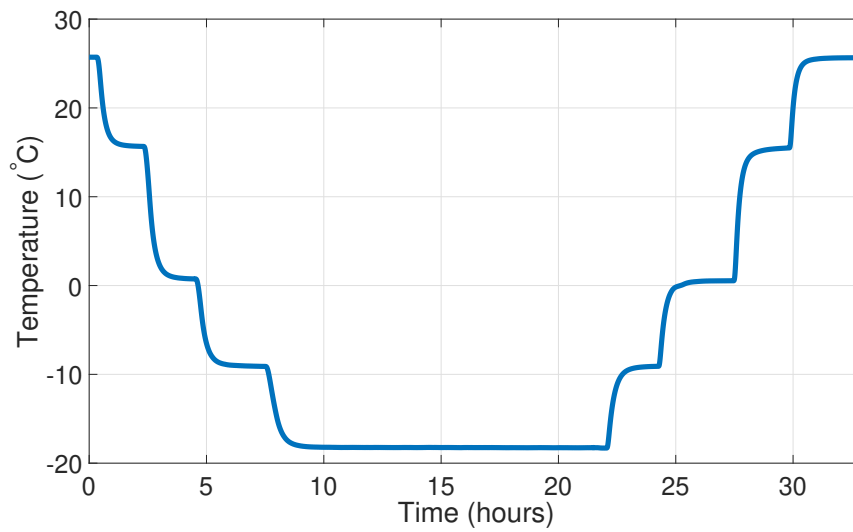


Figure 3.33 – Temperature in the climatic chamber during the test.

Table 3.11 – Polyimide parameters for temperature modelling.

Parameter	Minimum	Maximum
Thermal expansion coefficient of fibre, $\alpha_F(K^{-1})$	5E-7	6E-7
Thermal expansion coefficient of polyimide, $\alpha_P(K^{-1})$	3E-5	4E-5

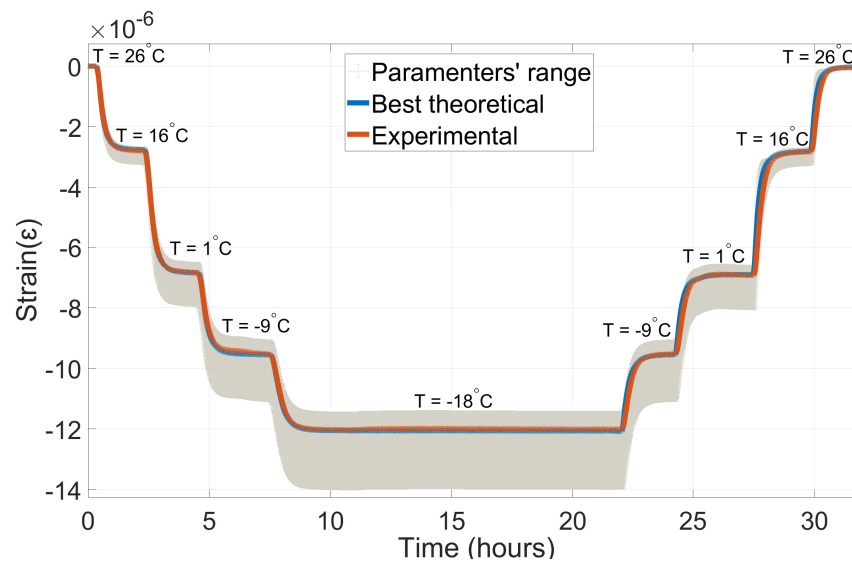


Figure 3.34 – Comparison between the temperature experimental data and the range of theoretical expected data

The best parameters are presented in Table 3.12 and the first observation is that there is a perfect match between the closest theoretical data and the experimental results of the 1 layer of polyimide coating.

Table 3.12 – Temperature expansion coefficients for modelling.

Parameter	Best
Thermal expansion coefficient of fibre, α_F	6.0E-7
Thermal expansion coefficient of polyimide, α_P	4.3E-5

For the remaining fibres with 2, 3 and 4 layers of polyimide coating, due to significant differences between the theoretical model and the experimental data, the theoretical data should be divided by a corrective factor. This corrective factor is exactly the number of layers (N) and it can indicate that there are significant thermal losses between the coating layers due to the imperfect adhesion.

After the correction, the results for the fibre with 2 layers of coating are plotted in Figure 3.35. Figure 3.36 and Figure 3.37 shows the results of the fibres with 3 and 4 layers of polyimide, respectively.

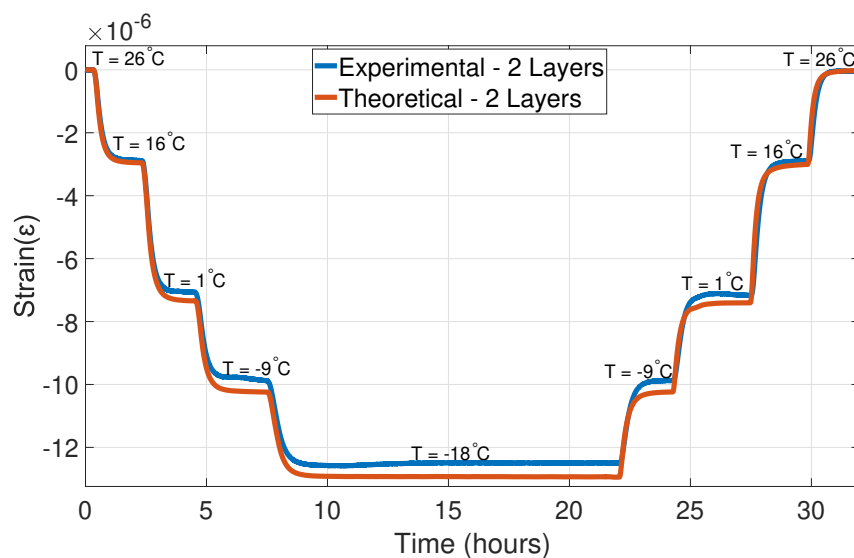


Figure 3.35 – Comparison between the theoretical model and the experimental data of the fibre with 2 layers of polyimide coating.

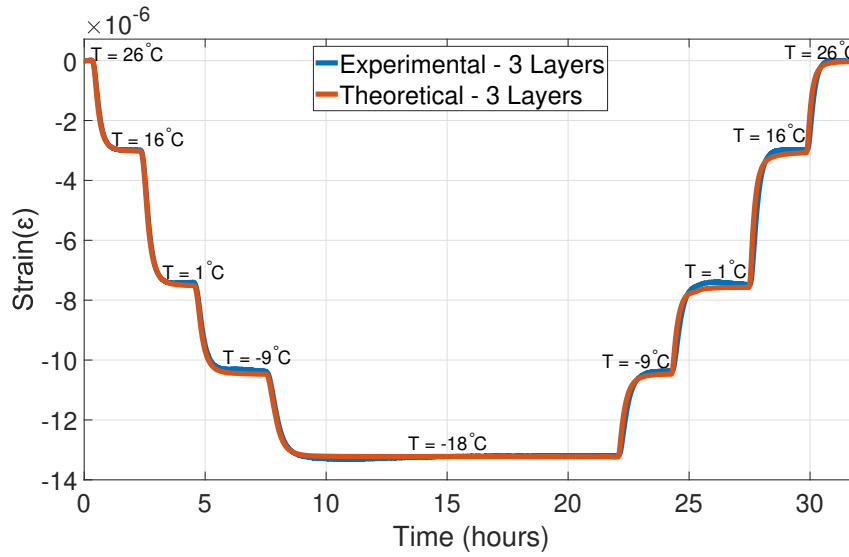


Figure 3.36 – Comparison between the theoretical model and the experimental data of the fibre with 3 layers of polyimide coating.

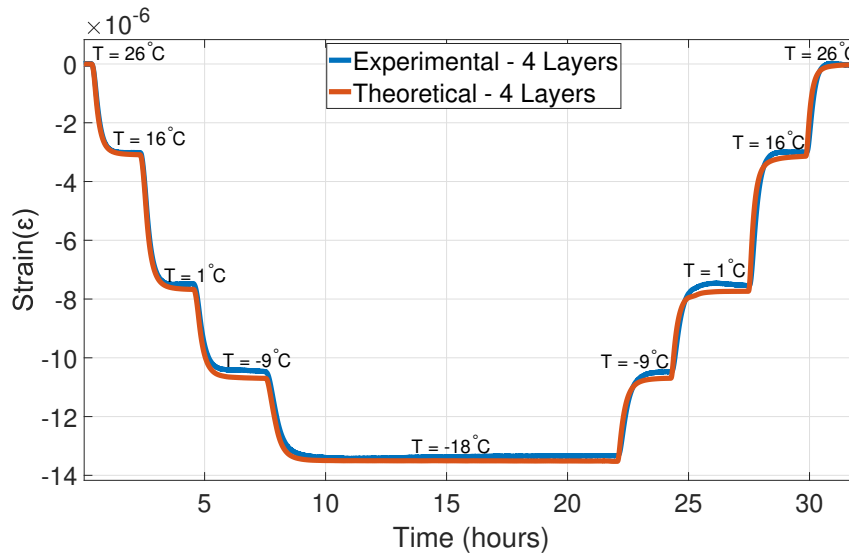


Figure 3.37 – Comparison between the theoretical model and the experimental data of the fibre with 4 layers of polyimide coating.

The results of the theoretical model fit with a good approximation the experimental data. While the model fits perfectly the results for 3 and 4 layers of polyimide coating, for the fibre with 2 layers of polyimide coating, the errors are slightly higher, which could be due to an imperfect adhesion or to an estimation error of the coating thickness. Overall and in spite of the uncertainties on the parameters and the possible imperfections in the fabrication of the fibres, the model agrees well with the experimental data for these polyimide-coated fibres with different number of coating layers.

3.4 Conclusions

The conclusions of this chapter can be summarized as follows:

- The concept of a distributed RH fibre sensor was fully validated at a large range of temperatures and, for the first time, a sensing range of kilometres was achieved using a ϕ -OTDR setup.
- Polyimide-coated fibres are better candidates than acrylate-coated fibres for humidity sensing and offer advantages on several aspects such as RH sensitivity and thermal stability in a large range of temperatures.
- The RH sensitivity of the acrylate-coated fibres is not negligible and, surprisingly, it increases significantly at lower temperatures and vanishes almost entirely at high temperatures (50°C). Even if fibres are prepared using the same type of acrylate in their coating composition, the RH sensitivities may be entirely different and should be individually evaluated.
- RH should be carefully controlled when doing distributed temperature or strain measurements using acrylate-coated commercial fibres since on a typical temperature range a small variation of 10% of RH can induce an error of $\approx 1.5^\circ\text{C}$. This value can be even higher in the case of polyimide-coated fibres due to their higher RH sensitivity.
- The test carried out using pure CO_2 demonstrated that, depending on the composition of the surrounding atmosphere, the impact of humidity in the coating can change in a non-negligible way.
- All the tested coated-fibres are RH sensitive and none of them can be used as temperature reference due to the cross-sensitivity between humidity and temperature. In laboratory environments, a bare fibre can be used, but it is impossible in a real-scenario application. Ideally, a RH insensitive fibre should be found.
- The response of the polyimide-coated fibres under variations of RH and temperature can be modeled with a reasonable match between experimental data and the theoretical expected values. The built model also identified the unknown parameters of the polyimide coating and of the silica fibre.

4 Relative Humidity Insensitive Optical Fibre

One of the main conclusions of the previous chapter is that a RH insensitive optical fibre should be found to avoid issues with the RH-temperature cross-sensitivity. Such optical fibre should be coated, to be resistant in a in-field application, and would be used as a temperature reference in a thermo-hygrometer distributed fibre sensor.

This chapter presents two innovative solutions for solving the cross-sensitivity issue. The first is based on an novel optical fibre with a single layer of an acrylate coating, the Desolite DS3471-3-14. The choice of this polymer coating is due to its low Dynamic Water Sensitivity (DWS) [102]. Several desolite-coated fibres with different coating thicknesses were produced in order to fully investigate the RH effect at different temperatures from -20°C to 50°C, using a CP- ϕ -OTDR interrogator. The second presents a new kind of silicone-coated optical fibres that was chosen based on the high capacity of water repellency and good releasability of the silicone material [103]. Seven samples of one metre each were produced and tested at different temperatures from -20°C to 55°C using a ϕ -OTDR interrogator [104, 105, 106]^I.

4.1 Desolite-coated Optical Fibres

4.1.1 Experimental Setup

Desolite DS3471-3-14 is a multi-functional acrylate coating that combines the properties of the soft and hard coating, usually applied on standard acrylate fibres. With this coating, which allows increasing fibre drawing speed and offers improved humidity resistance, the optical fibre is resistant to micro-bending and, at the same time, is mechanically protected.

All the desolite-coated fibres used for this study were entirely fabricated at FiberTech Lille (IRCICA-Université de Lille) by drawing Modified Chemical Vapor Deposition (MCVD) silica glass preform doped with germanium and phosphorus oxide. The resulting SMF-type fibre had a core-to-cladding diameter ratio of 8/125 with a refractive index difference of about

^IIn the moment of this dissertation submission, the publications were under review.

6×10^{-3} between core and cladding. The attenuation coefficient was 0.5 dB/km at 1550 nm, as measured using OTDR. A 4 μm core diameter fiber equipped with a Desolite coating was also manufactured.

To have a well-known RH reference in the test, a polyimide-coated optical fibre was also part of the tested fibres. The temperature reference is given by a stripped coated fibre (Bare) and all of these fibres have been spliced and arranged to form a single FUT, mounted strain-free in special plastic holder, as shown in Figure 4.1 that also shows a micrograph of one sample.

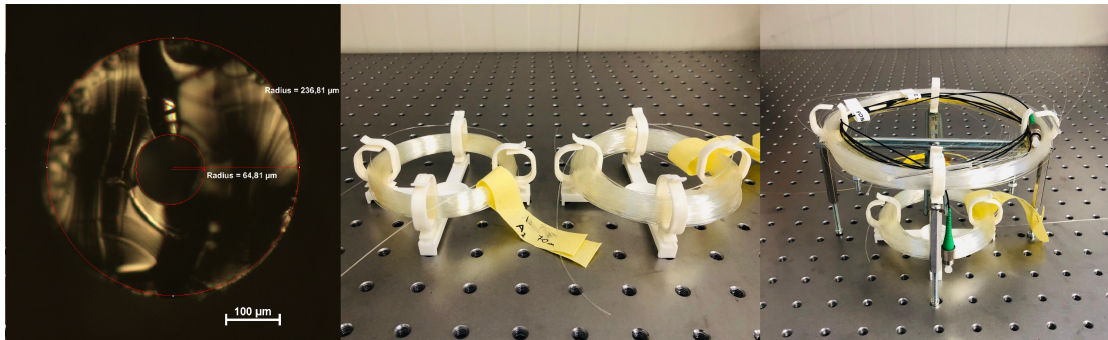


Figure 4.1 – Micrograph of a DeSolite-coated fibre and stress-free fibre holders.

In summary, the FUT was around 770 metres long and made of: 6 pieces of desolite-coated fibres^{II} with different thicknesses (from 26.5 μm to 93.5 μm); 1 piece of desolite-coated fibre with the same coating but with a 4 μm core diameter; 1 piece of polyimide-coated commercial fibres; and 1 piece metres of bare silica fibre. The full list of FUT is given in Table 4.4:

Table 4.1 – List of FUT with their respective coating and core characteristics.

Fibre	Coating Type	Coating Thickness(μm)	Core Diameter(μm)
A	DS3471-3-14	27.5	4
E1	DS3471-3-14	26.5	8
C1	DS3471-3-14	55.5	8
A1	DS3471-3-14	57.5	8
B1	DS3471-3-14	63.5	8
F1	DS3471-3-14	85.0	8
G1	DS3471-3-14	93.5	8
PI	Polyimide	15	9
B	Bare	0	9

The FUT was analysed with the CP- ϕ -OTDR interrogator described in Figure 3.14.

^{II}The fibres designations are provided by the manufacturer.

4.1.2 Experimental Results

The experimental procedure started with a temperature characterization followed by 6 RH tests at different constant temperatures (-20°C, -10°C, 0°C, 15°C, 25°C and 50°C).

Temperature Characterization

The temperature was gradually changed from 25°C to -20°C at a constant level of RH (7.3% \pm 0.5%) to avoid cross-sensitivities. The temperature and RH measured by the reference electronic sensors are plotted in Figure 4.2.

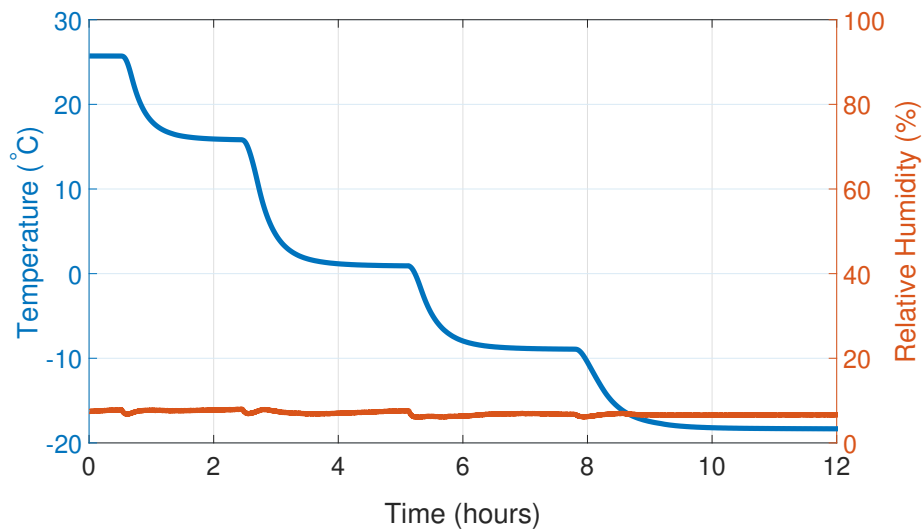


Figure 4.2 – Climatic chamber conditions during the temperature characterization test. Temperature in blue and RH in orange.

The fibres frequency shift are grouped in Figure 4.3 and the respective temperature calibrations are represented in Figure 4.4.

The first observation is that all fibres show linear temperature dependence, with a coefficient of determination (R^2) always higher than 0.99. The polyimide-coated and the bare fibre results confirm what was obtained in the previous chapter, with a temperature sensitivity of 1.31 GHz/K and 1.12 GHz/K respectively.

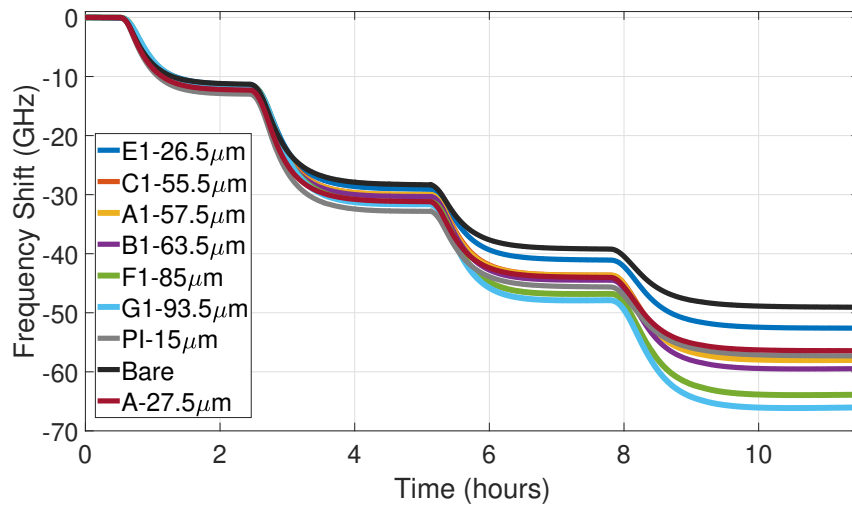


Figure 4.3 – Grouped plot of all fibres frequency shift during the temperature characterization test.

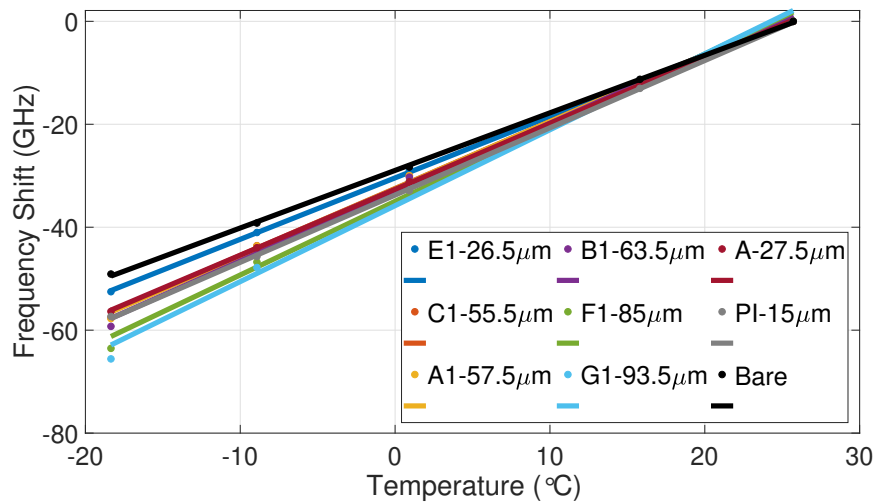


Figure 4.4 – Temperature calibrations plot of all fibres.

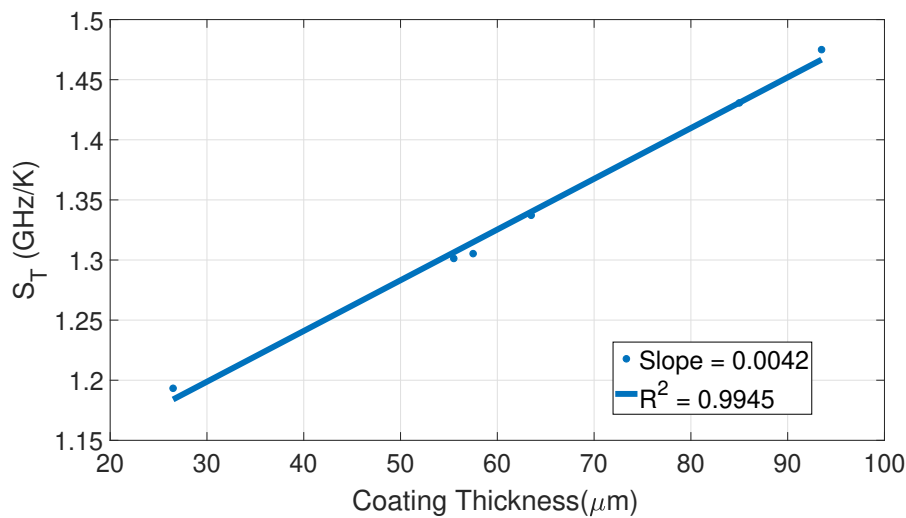
All temperature sensitivities are summarized in Table 4.2.

As expected, the bare fibre shows the lowest temperature sensitivity, due to the absence of coating and the temperature sensitivity of the desolite-coated fibres increases linearly with the coating thickness, as demonstrated in Figure 4.5. The uncertainty of the temperature sensitivity also increases with the coating thickness as expressed by the lower R^2 . Fibres with a thinner coating show a better linear fitting because the stress induced by the coating is negligible compared with the stress induced by the thermal expansion of the silica glass. The

Table 4.2 – List of FUT with respective thicknesses and temperature sensitivities.

Fibre	Coating Thickness (μm)	S_T (GHz/K)	R^2
A	27.5	1.279 ± 0.008	0.9999
E1	26.5	1.193 ± 0.008	0.9999
C1	55.5	1.30 ± 0.03	0.9979
A1	57.5	1.31 ± 0.04	0.9978
B1	63.5	1.34 ± 0.04	0.9968
F1	85.0	1.43 ± 0.06	0.9939
G1	93.5	1.48 ± 0.08	0.9922
PI	15	1.31 ± 0.01	0.9998
B	0	1.12 ± 0.01	0.9998

stress induced by the coating increases with its thickness. Overall, the uncertainty on the temperature sensitivity is of the order of tens of MHz/K.

Figure 4.5 – Variation of the temperature sensitivity, S_T , with the coating diameter.

Due to its small core diameter, the loss in fibre A was significantly higher and its temperature sensitivity was not considered in Figure 4.5. However fibre A shows linear behaviour and temperature sensitivity (1.279 GHz/K). Up to 93.5 μm of coating diameter, the temperature sensitivity of the desolite-coated fibres increases linearly at a rate of 4.2 MHz/K/ μm .

Relative Humidity Characterization

A relative humidity test was performed afterwards at 50°C, 25°C, 15°C, 0°C, -10°C and -20°C and the first test presented is at 25°C. Figure 4.6 shows the temperature and RH dynamics during the test, monitored by the setup reference instrumentation, in which the RH was sequentially changed from 0.2% to around 80%. The responses of all fibres under test, already temperature compensated as explained in the Section 3.2.2, are compared in Figure 4.7.

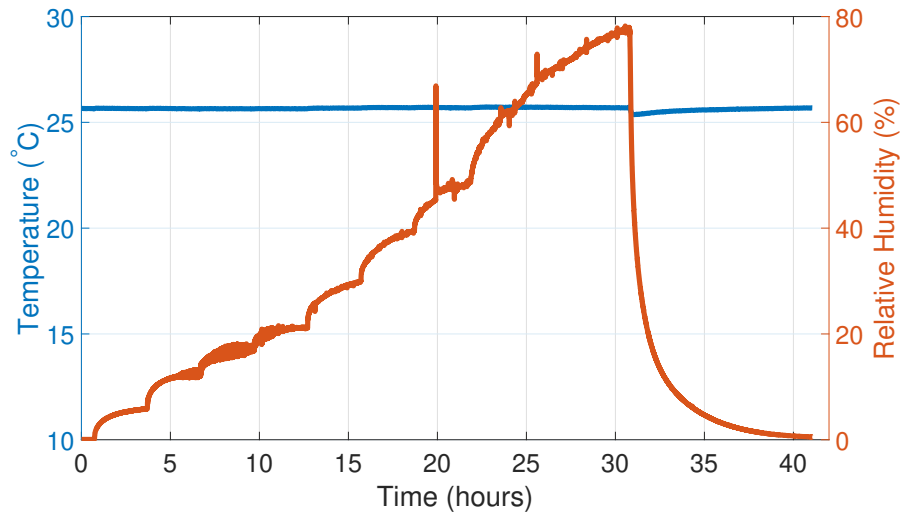


Figure 4.6 – Climatic chamber conditions during the RH characterization test. Temperature in blue and RH in orange.

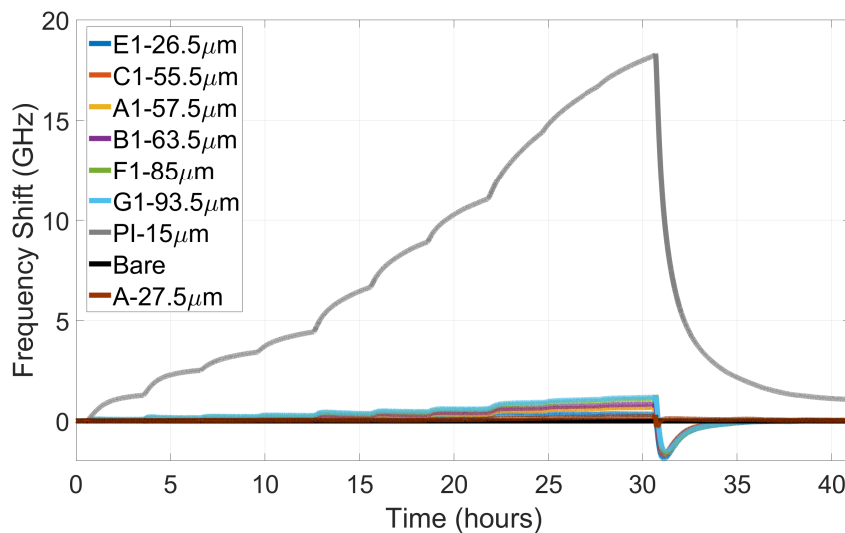


Figure 4.7 – Grouped plot of the frequency shifts of all fibres during the RH characterization test.

The first observation is that all fibres have a completely negligible response to RH when compared with the polyimide-coated fibre. This RH insensitivity might be explained by the different DWS of polymer coatings [102]. The parameter DWS depends on the ability of porous material, therefore polymers, to absorb water molecules, and it is indeed smaller for the polymer desolite DS 3471-3-14 than for other kinds of secondary coatings ^{III}.

Analysing only the desolite-coated fibres, one can conclude that at 25°C their responses are closer to the temperature reference, given by the bare fibre, than to the RH variations and Figure 4.8 shows the comparison with the bare fibre.

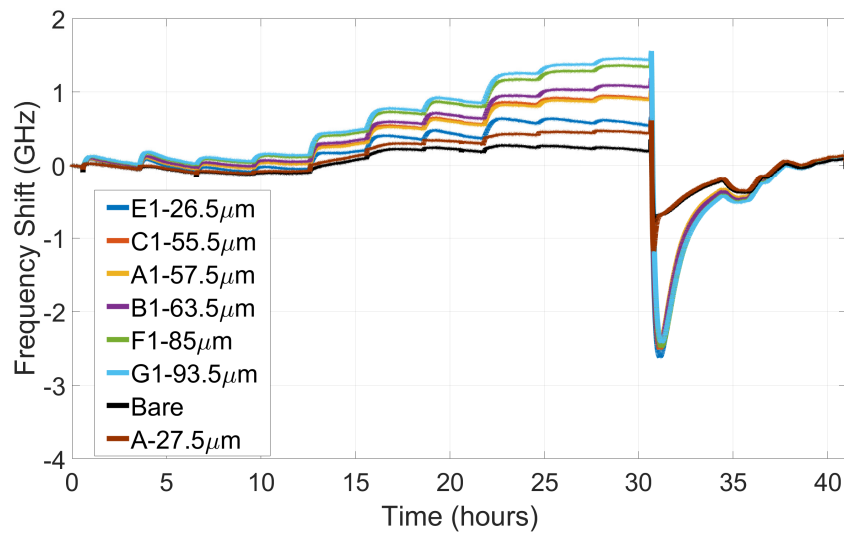


Figure 4.8 – Grouped plot of the frequency shift of all desolite-coated fibres together with the bare fibre.

Analysing Figure 4.8, it is clear that, even if the desolite-coated fibres can be considered insensitive to RH and be used as a temperature reference at 25°C, their behaviour differ slightly from the bare fibre. Except for fibres A and E1, whose responses are extremely close to the bare fibre, the responses of the thicker coated fibres at high RH values allow for a RH calibration even if the magnitude is negligible. The temperature sensitivity is around 1.3 GHz/K while the RH sensitivity is a few MHz/%RH. Figure 4.9 shows the RH calibrations of 5 fibres C1, A1, B1, F1 and G1.

In this case, the RH sensitivity calibration curve is not linear. The best-fitting equation is a polynomial of 2nd order and consequently, the RH sensitivity is a linear function of the RH itself. This non-linear behaviour is explained by the non-linear variation of the Young's Modulus, which is a mechanical property that measures the stiffness of a solid material. Young's Modulus, especially of the acrylate polymers, decreases linearly with increasing humidity and decreasing logarithm of the strain rate [107]. The combined effects of these parameters, humidity and strain rate, results in a non-linear RH response. At the same time, the temperature has a

^{III}Information provided by the manufacturer - on 150 µm films: weight change – 2%; extractable – 1%.

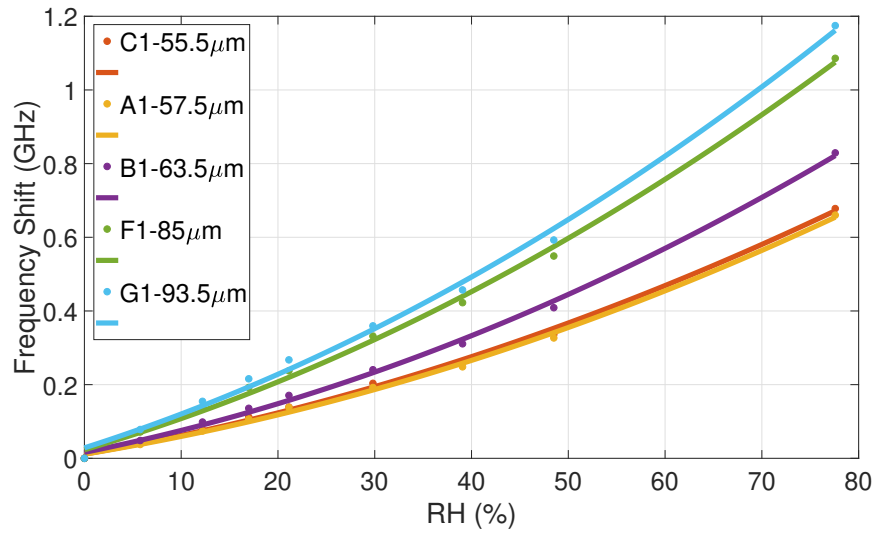


Figure 4.9 – RH calibration of 5 desolite-coated fibres.

significant impact on the Young's Modulus of this kind of DS3471 coating. It varies from 2.2 MPa at 20°C to 520 MPa at -60°C [108]. Consequently, it is expected that a fibre with this kind of coating changes drastically its behaviour at different temperatures. On the other hand, this effect is not evident in the PI-coated fibres because the variation of Young's modulus in the tested temperature range is not significant (3.2 ± 0.1 GPa) [109].

A RH test at 50°C was performed afterwards. Figure 4.10 shows the climatic chamber dynamics during the test and due to limitations in the test setup, it was not possible to go beyond 20% RH at 50°C.

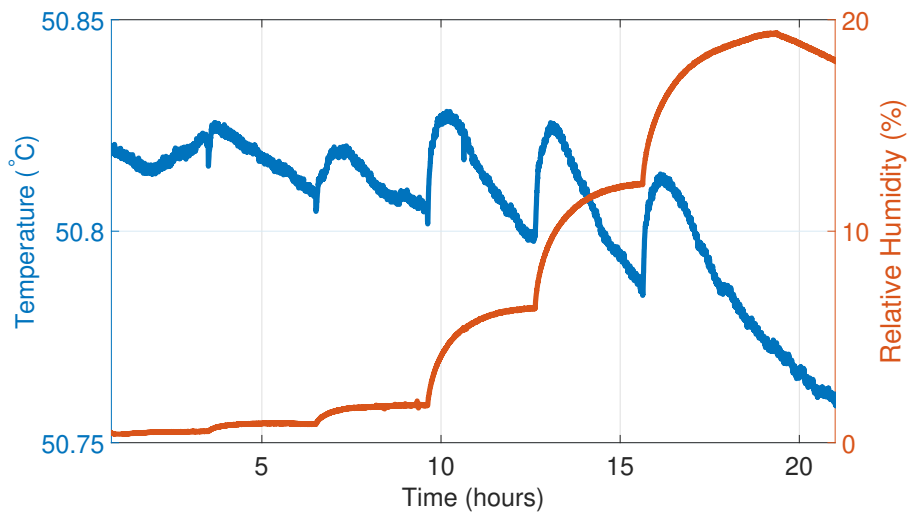


Figure 4.10 – Climatic chamber conditions during the RH at 50°C.

Figure 4.11 groups the frequency shift of all the tested fibres. Comparing the desolite-coated fibres with the PI fibre response, after applying the temperature compensation method, it is clear that the desolite-coated fibre signals are negligible, confirming that these fibres can also be used as temperature reference in an RH distributed sensor prototype operating at high temperatures.

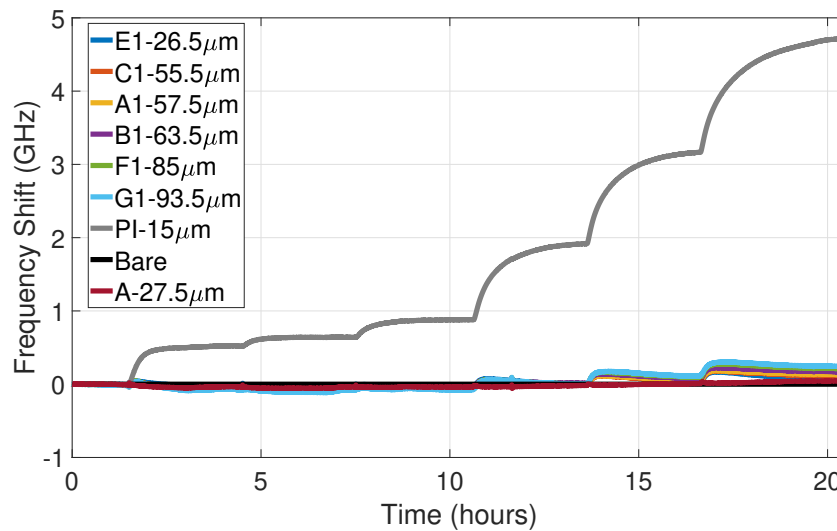


Figure 4.11 – Grouped plot of all fibres frequency shift during the RH test at 50°C.

Figure 4.12 groups only the desolite-coated and bare fibres responses.

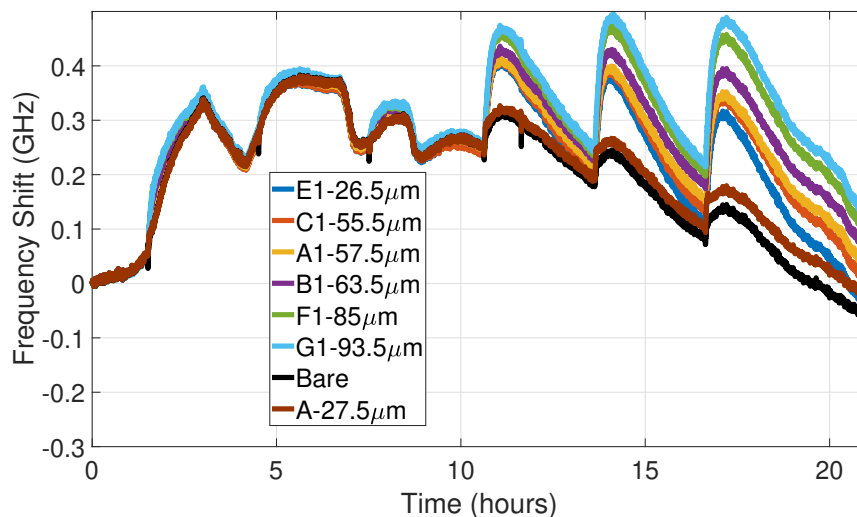


Figure 4.12 – Grouped plot of desolite-coated fibres frequency shift during the RH test at 50°C.

Figure 4.12 shows that the responses of the desolite-coated fibres are similar to the bare fibre (black line) that, at the same time, is similar to the temperature variations measured by

the electronic reference temperature sensors, as seen in Figure 4.10. All fibres have a similar behaviour up to around 10 hours of test, but it is visible that in the latest RH steps, the thicker fibres show RH sensitivity. Nevertheless, the RH sensitivity is attenuated after a couple of hours and, it is predictable that waiting more time, the difference between the fibres signals and the bare fibre would be completely vanished. At 50°C, all desolite-coated fibres show RH insensitivity.

As the desolite-coated fibres show a non-linear RH response, the RH sensitivities comparison is extremely complicated. In this study, in order to compare the RH sensitivities at different temperatures, a simplification was made. For every temperature tested, the minimum and the maximum RH sensitivity were calculated with the minimum and maximum linear slopes in the range of RH explored. An example can be seen in Figure 4.13.

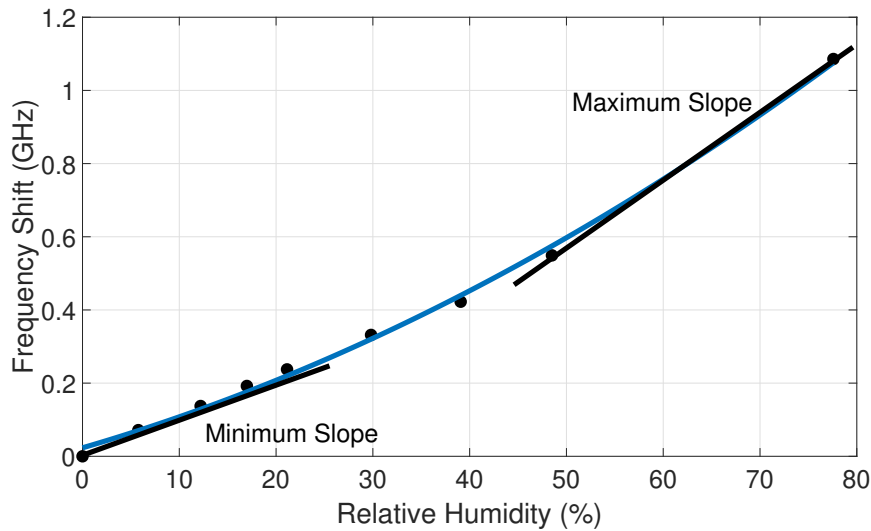


Figure 4.13 – Example of minimum and maximum RH sensitivity.

The minimum and maximum slopes give the minimum and maximum RH sensitivity of each fibre at each temperature in the tested RH range. Then, the mean of both values is calculated, and the difference between the the minimum or maximum values and the mean gives the measurement error.

The results of all the remaining RH tests at different temperatures are grouped in Figure 4.14 and Table 4.3 summarizes all RH sensitivities calculated in this study with the respective errors.

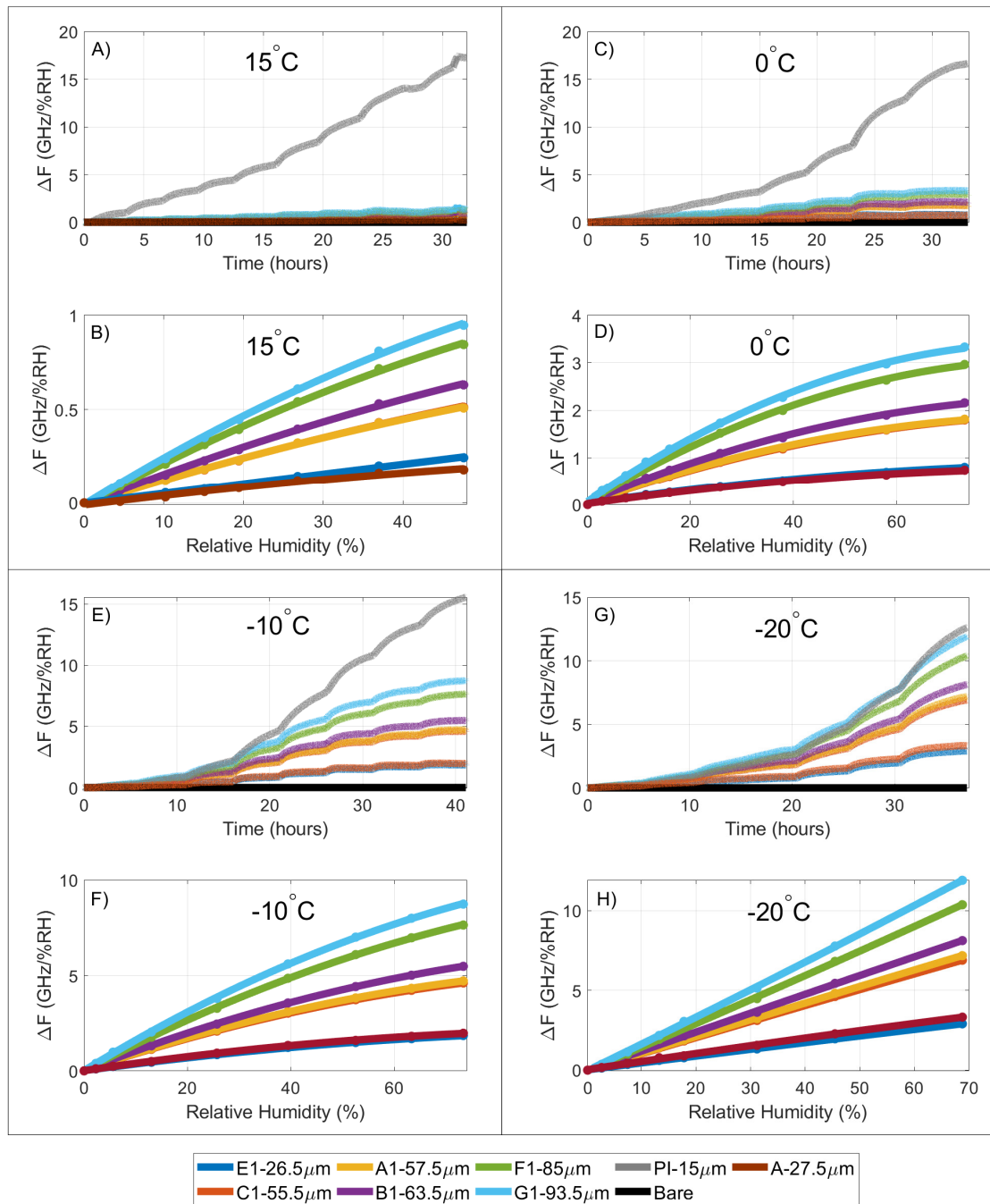


Figure 4.14 – Grouped plot of all fibre frequency shifts at different temperatures. A) Frequency shift at 15°C. B) RH calibrations a 15°C. C) Frequency shift at 0°C. D) RH calibrations a 0°C. E) Frequency shift at -10°C. F) RH calibrations a -10°C. G) Frequency shift at -20°C. H) RH calibrations a -20°C.

Table 4.3 – RH Sensitivities of all fibres in MHz/%RH.

Fibre	Coating Thickness (μm)	50°C	25°C	15°C	0°C	-10°C	-20°C
A	27.5	INSENSITIVE	INSENSITIVE	2.9 ± 1.2	15.4 ± 8.6	32.7 ± 16.6	52.6 ± 7.8
E1	26.5	INSENSITIVE	INSENSITIVE	4.7 ± 0.6	18.0 ± 11.0	31.1 ± 14.7	44.5 ± 4.5
C1	55.5	INSENSITIVE	9.3 ± 2.4	9.2 ± 2.1	36.2 ± 22.2	74.4 ± 36.0	96.4 ± 1.0
A1	57.5	INSENSITIVE	9.0 ± 2.5	9.3 ± 1.9	35.2 ± 20.9	71.9 ± 33.2	100.0 ± 1.2
B1	63.5	INSENSITIVE	11.5 ± 3.1	12.1 ± 2.7	42.3 ± 25.0	84.0 ± 37.3	110.8 ± 4.2
F1	85.0	INSENSITIVE	15.5 ± 3.1	16.0 ± 4.4	53.3 ± 31.5	106.2 ± 39.6	137.1 ± 15.3
G1	93.5	INSENSITIVE	16.65 ± 3.4	18.3 ± 5.4	61.7 ± 38.2	123.6 ± 49.5	156.2 ± 20.6
PI	15	220.9	236.2	229.5	227.6	223.4	184.3

At 15°C, the two less RH sensitive fibres, fibre A and E1 start to react slightly to RH, but with RH sensitivities of the same magnitude order as the optical interrogator error. When comparing the behaviours of these two fibres, it is possible to conclude that fibre E1 reacts to humidity changes but it tends to recover to a lower level, as shown in Figure 4.15. The magnitude of this effect is residual compared with the temperature sensitivity but it can be seen as a small local spike in the temperature signal, which would then almost disappear. On the other hand, fibre E1 tends to recover to a lower level, fibre A tends to slowly increase.

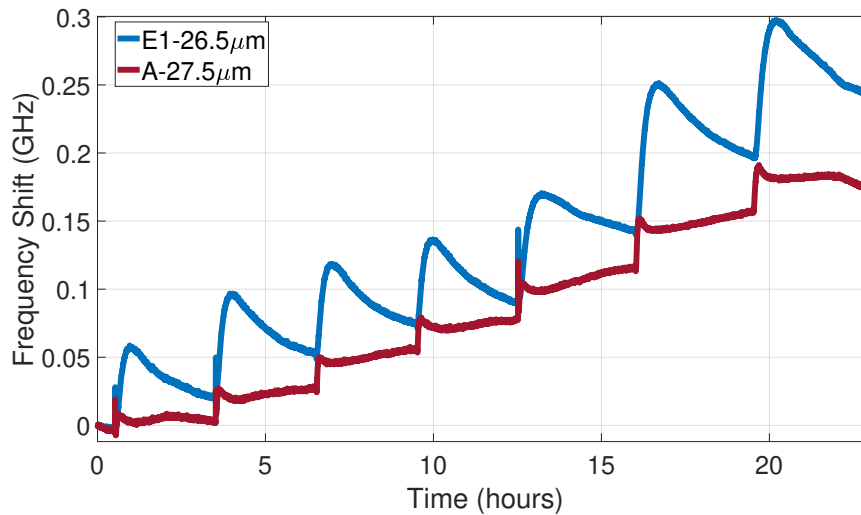


Figure 4.15 – Response of fibre A and E1 in a RH test at 15°C.

The remaining desolite-coated fibres show a higher RH sensitivity but still negligible when compared with the polyimide-coated fibre. Decreasing the temperature, the RH response starts to increase significantly and at 0°C, the RH sensitivity of the thicker fibres can be approximately half of the RH sensitivity of the polyimide-coated fibre. At -10°C, the RH sensitivities continue to increase, getting closer to the polyimide-coated fibre RH sensitivity. At -20°C, the desolite-coated fibres reach a maximum of RH sensitivities, and the thicker fibres have an extremely similar RH sensitivity than the polyimide-coated fibre.

To explore further the RH effect on these fibres, a final 4-step RH test at 25°C was performed.

The test consisted of smaller RH changes but with positive and negative variations to analyse the RH absorption and releasing behaviour differences. The dynamics are represented in Figure 4.16 and the frequency shift of all desolite-coated fibres is presented in Figure 4.17.

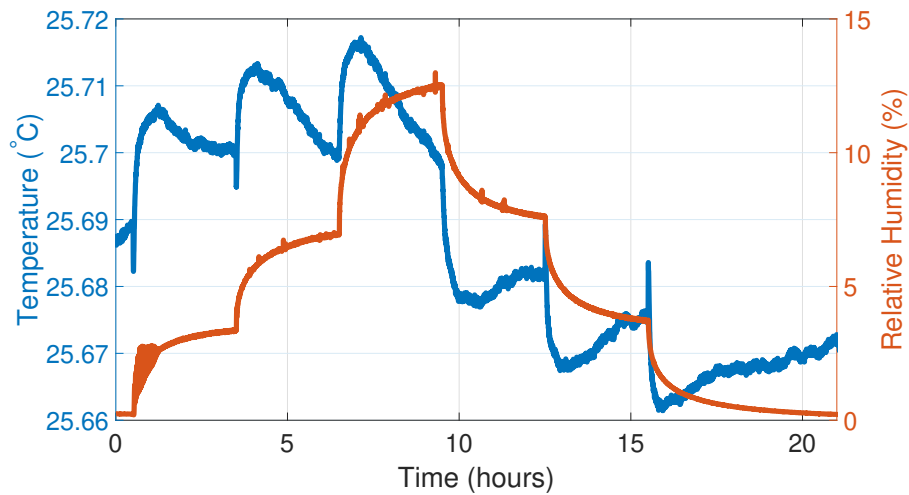


Figure 4.16 – Climatic chamber conditions in the 4-step RH test at 25°C.

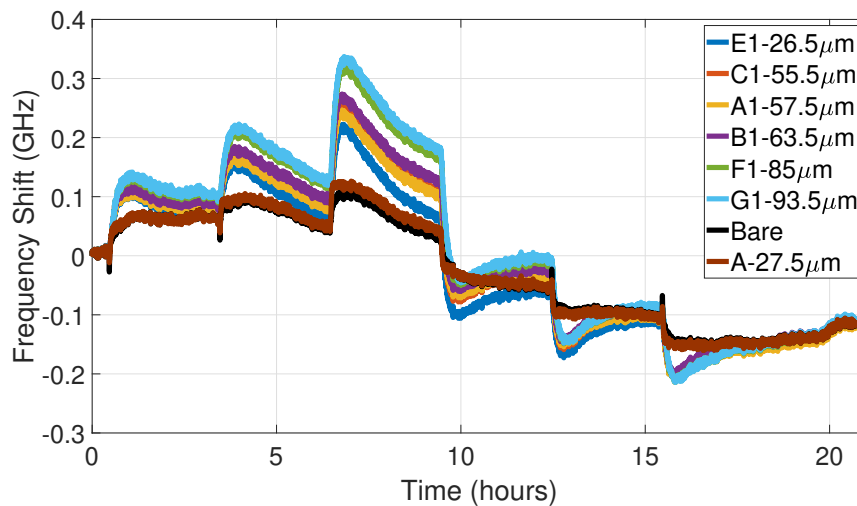


Figure 4.17 – Grouped plot of all desolite-coated fibres during the 4-step RH test at 25°C.

The main observation is that when the RH variation is of the order of 12%, the desolite-coated fibres follow the temperature trend whether the RH increases or decreases. As expected, the thicker fibres show some cumulative frequency shift while fibre A, for example, is completely unaffected by the RH changes at 25°C.

4.1.3 Conclusions

The main conclusion of our work on Desolite-coated optical fibres so far is that they are good candidates to serve as temperature references in an RH distributed sensor, in particular fibres E1 and A. These two fibres can be considered RH insensitive at temperatures above 15°C. Below this temperature, the RH sensitivity can still be considered negligible. All the remaining fibres show an RH insensitivity at 50°C but a significant RH sensitivity at temperatures below 0°C. At temperatures around 15°C, all fibres have an RH sensitivity that is between 1% and 10% of the PI fibre RH sensitivity and for that reason, can be considered negligible. At temperatures above 0°, the fibres temperature sensitivity is a few orders of magnitude higher than the RH sensitivity and, for comparison reasons, even if the RH changes with 100% at 15°C, which is an extreme case, the equivalent change of temperature for fibre A is around 0.3°C. Even down to temperatures of -20°C a significant variation of 20% of RH induces a temperature error around 0.7°C, which is a negligible error for most of the temperature applications. For the G1 fibre, at -20°C, a variation of 10% RH can induce an error of 1°C, which is already a significant variation.

Coupling one of these desolite-coated fibres, especially fibre A and E1, with a polyimide-coated fibre, a distributed thermo-hygrometer to work over temperatures above 15°C avoiding the cross-sensitivities issue can be developed.

4.2 Desolite-coated Optical Fibre for Temperature Applications

The next study is dedicated to the analysis of two desolite-coated fibres with a coating thickness of 280 μm and 322.5 μm . These two desolite-coated fibres were included in the previous FUT and the temperature characterization test is described in Figure 4.2. For comparison reasons, the results of the E1-26.5 μm and G1-93.5 μm fibres, already presented in the previous section, are also included in this analysis.

4.2.1 Experimental Setup

Using the same optical setup, a new FUT was prepared and its constituents are summarized in Table 4.4.

Table 4.4 – List of FUT with their respective coating and core characteristics.

Fibre	Coating Type	Coating Thickness (μm)	Core Diameter (μm)
E1	DS3471-3-14	26.5	8
G1	DS3471-3-14	93.5	8
E2	DS3471-3-14	280	8
F2	DS3471-3-14	322.5	8
B	Bare	–	9

4.2.2 Experimental Results

Figure 4.18 and Figure 4.19 show the total frequency shift of all fibres during the temperature characterization and the temperature calibration plots, respectively.

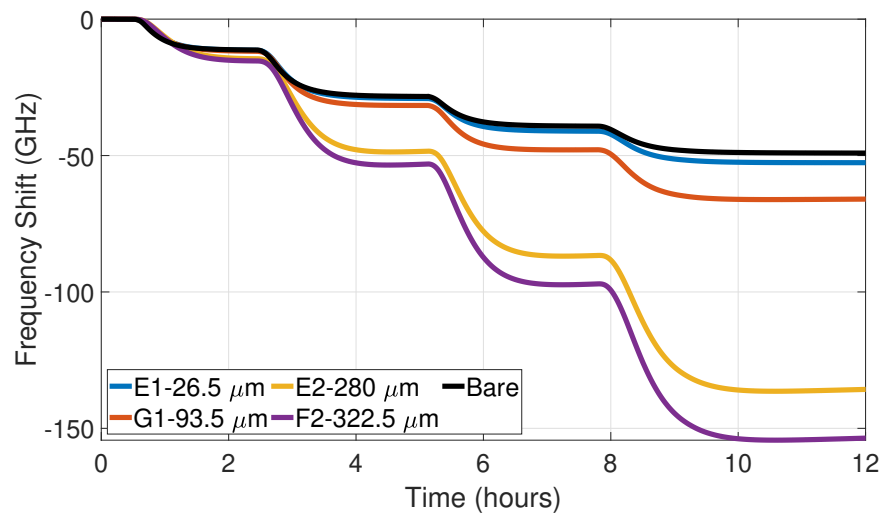


Figure 4.18 – Frequency shift of all fibres grouped during the temperature characterization test.

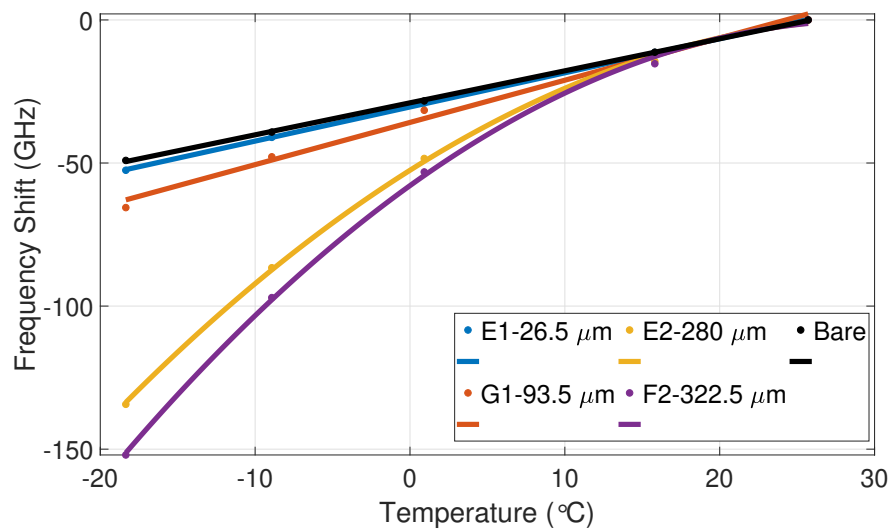


Figure 4.19 – Temperature calibration curves of all the FUT.

Table 4.5 summarizes the temperature sensitivities with the respective coefficient of determination (R^2).

As expected, the bare fibre shows the lowest temperature sensitivity due to the absence of coating and an increment of the coating thickness naturally turns into a higher temperature

Table 4.5 – Comparison between the temperature sensitivities.

Fibre	S_T (GHz/K)	R^2
Bare	1.12 ± 0.01	0.9998
E1	1.193 ± 0.008	0.9999
G1	1.48 ± 0.08	0.9922
E2	$-0.0549 \times (T+273.15) + 3.4127^*$	0.9993
F2	$-0.0654 \times (T+273.15) + 3.8876^*$	0.9993

* T is temperature.

sensitivity. Fibres E1 and G1 show a linear behaviour, with an R^2 higher than 0.99, while fibres E2 and F2 show an extremely increased temperature sensitivity, especially at temperatures lower than 0°C, but a non-linear behaviour.

This loss of linearity can be explained by the significant changes in the acrylate properties at low temperatures, specifically the tensile module, elongation and tensile strength [108]. For the thinner coatings, the dominant effect measured is the strain caused by the linear thermal expansion of the silica fibres components. However, increasing the thickness of the coating, this effect starts to be less relevant compared with the strain caused by the expansion or shrinkage of the acrylate coating. The total frequency shift is then the combination of these two mentioned phenomena and it means that in an optical fibre with a significantly thick coating, the frequency shift is mostly affected by the coating effect rather than the silica thermal effect itself. The result is a significantly amplified but non-linear temperature response as seen in fibres F2 and E2. For these two fibres, the best fitting function to describe the temperature behaviour is a polynomial of second order, which means that the temperature sensitivity of the sensor has a temperature dependence (T). The stabilization response is also affected by the coating thickness, as expected. Fibre E2 and F2 take longer to stabilize due to the higher diffusion time caused by the thick coating.

Analysing separately the temperature sensitivity of fibre E2 and F2 in the range of temperatures between -10°C and -20°C, where they reach the maximum value, it is possible to conclude that the sensitivities are significantly higher compared with the others desolite-coated fibres but also compared with the traditional SMF (typically around 1.5 GHz/K). Table 4.6 shows the comparison between the sensitivities and the measurement resolutions. For the resolution measurement calculation, one should take into consideration the sensitivity of the CP- ϕ -OTDR interrogator, which is lower than 1 MHz.

Table 4.6 – Temperature sensitivities comparison and respective measurement resolution.

Fibre	S_T (GHz/K)	Resolution (mK)
Bare	1.12	0.89
E1	1.20	0.84
G1	1.48	0.68
E2	5.06	0.20
F2	5.83	0.17

Fibres E2 and F2 have a much higher sensitivity to temperature, from -10°C and -20°C, i.e around 5 times more than the pure silica fibre. All the tested fibres have a resolution lower than 1 mK, but fibres E2 and F2 go down to 0.20 and 0.17 mK respectively. These results represent a significant improvement compared with a commercial SMF.

4.2.3 Conclusions

The main conclusion of Section 4.2 is that the temperature sensitivity of the thicker desolite-coated fibres increases significantly at lower temperatures but, also that these fibres show a non-linear response. The thermal expansion and shrinkage of the coating results in an induced strain that enhances significantly the temperature sensitivity. This means that these fibres are good candidates to be used in a highly sensitive temperatures distributed sensor, but special attention should be given to the data analyses.

Selecting the correct coating thickness, a desolite-coated fibre can either be a temperature reference for a RH measurement or an enhanced temperature sensor at temperatures below 0°C, with a temperature resolution in the order of 100 to 200 μ K.

4.3 Silicone-Coated Fibres

Despite the fact that the previous section presents a coated fibre for temperature reference in a thermo-hygrometer at temperature above 15°C, a new RH insensitive fibre that can operate in a broader temperature range should be identified. One candidate is silicone owing to its well-known impermeability to water molecules [103] and several samples of silicone-coated fibre were drawn to address this issue.

4.3.1 Experimental Setup

The home-made optical interrogator used to characterize the silicone-coated fibres is fully described in Section 3.1.1. The FUT was composed of 7 different samples of silicone coated-fibres of 4 μ m of thickness. A bare fibre and a polyimide-coated fibre were added to the fibres under test to be the temperature and RH references during the test. The FUT was completed with a sample of a desolite-coated fibre, fibre A-27.5 μ m.

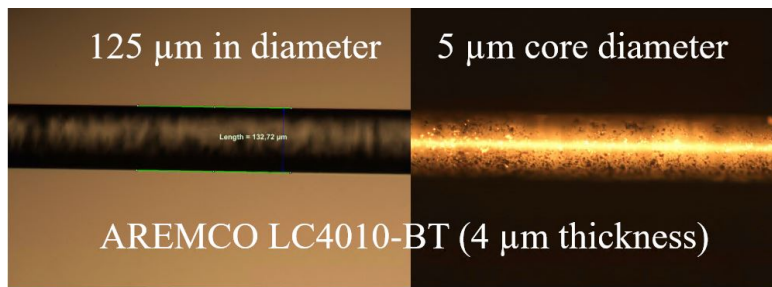


Figure 4.20 – Silicone-coated fibres micrograph.

All fibres were spliced and rearranged as a single fibre and submitted to a temperature test and RH at 4 different temperatures, 25°C, 0°C, -15°C and 55°C.



Figure 4.21 – Silicone-coated fibres in a stress-free holder.

4.3.2 Experimental Results

Temperature Characterization

The objective of the 3-step temperature characterization (25°C, 20°C and 15°C) was to compare the behaviour of these new silicone-coated fibres with the bare fibre. Figure 4.22 shows the climatic chamber dynamics during the test and Figure 4.23 the response of the full FUT.

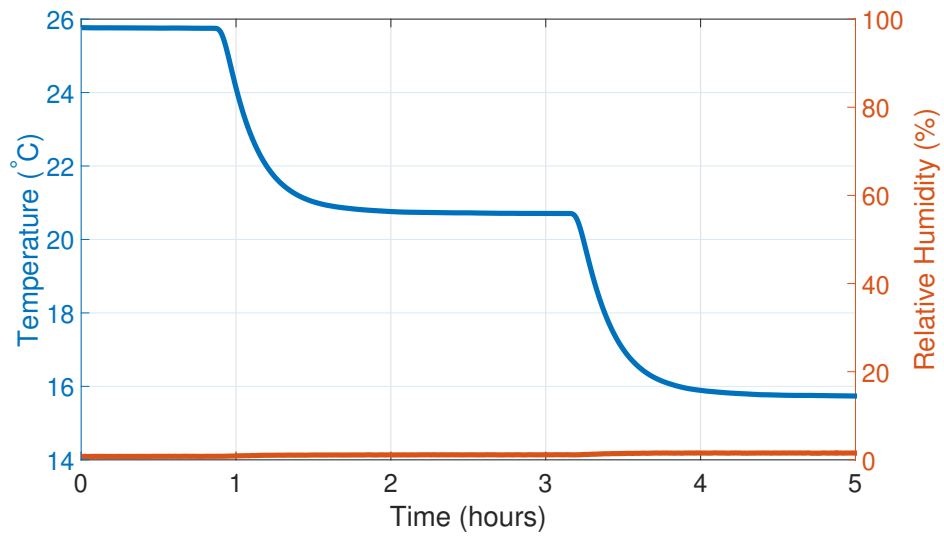


Figure 4.22 – Climatic chamber conditions during the 3-step temperature characterization.

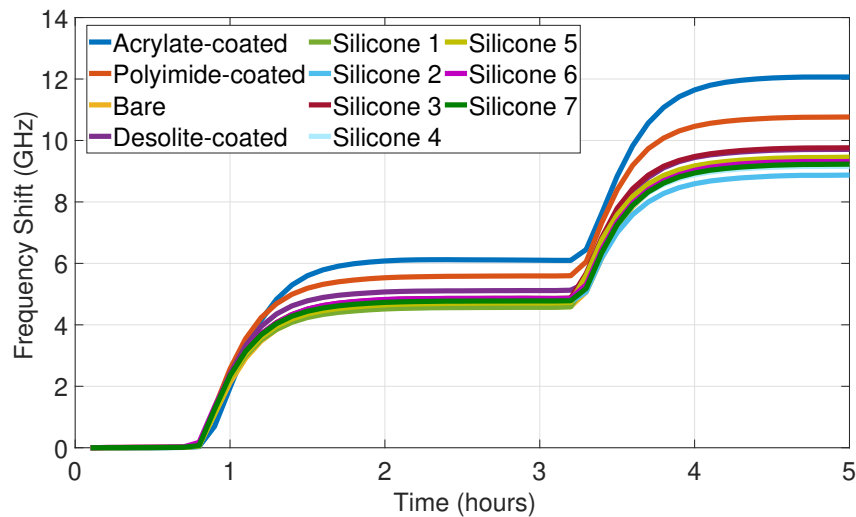


Figure 4.23 – Silicone-coated fibres compared with bare fibre in the temperature test.

As shown in Figure 4.23, the response of the silicone-coated fibres are extremely close to the bare fibre, and also the desolite-coated fibre, which means that the temperature sensitivity is practically the same. The responses of the acrylate- and polyimide-coated fibres are naturally higher, as demonstrated in the previous chapters of this dissertation.

Relative Humidity Characterization

The RH characterization consisted in a RH test at 5 pre-set temperatures, 55°C, 25°C, 0°C and -20°C. The first RH test was performed at 25°C and the dynamics is shown in Figure 4.24.

Figure 4.25 groups all the fibre responses. The results were not temperature compensated to be able to compare them directly with the bare fibre results.

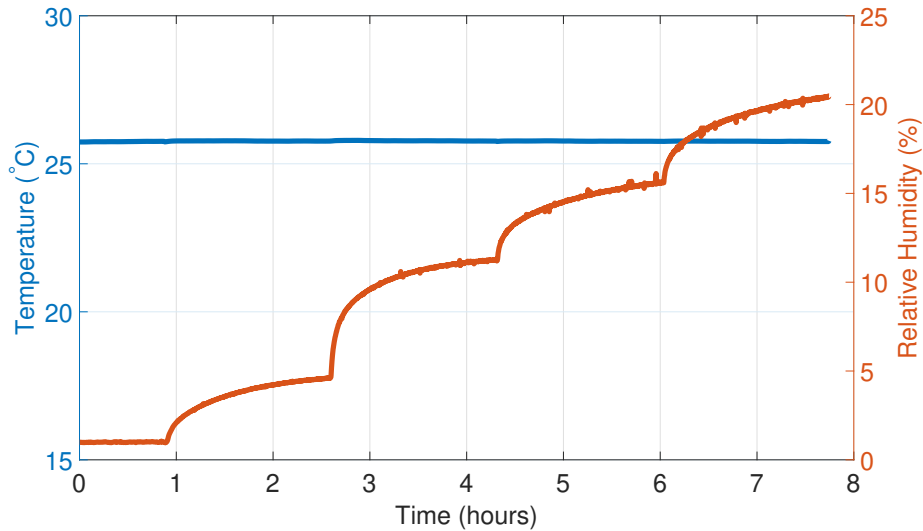


Figure 4.24 – Climatic chamber conditions during RH test at 25°C.

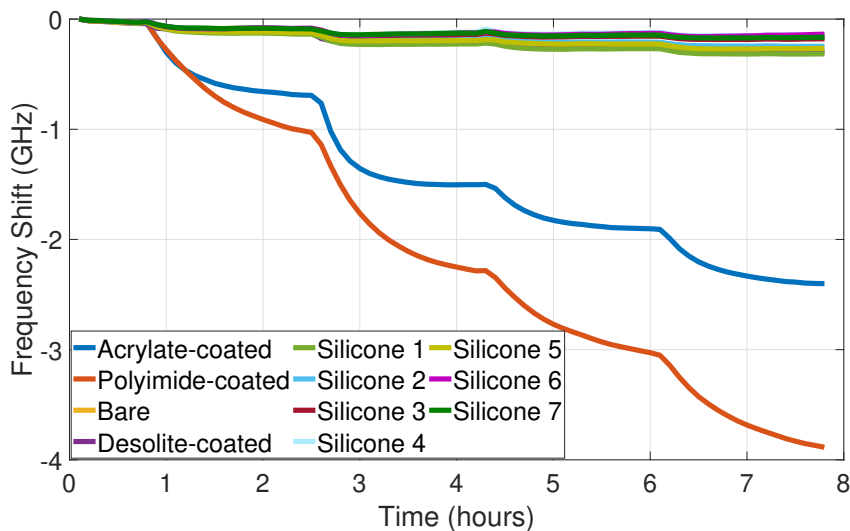


Figure 4.25 – Silicone-coated fibres compared with bare fibre in the RH test at 25°C.

As expected, the responses of the acrylate- and polyimide-coated fibres are higher due to their hygroscopic characteristics. The response of the silicone-coated fibres to RH is clearly negligible and it is again close to the bare fibre, which is measuring only the temperature fluctuation in the climatic chamber. Figure 4.26 shows a comparison between one silicone-coated sample and the bare fibre response.

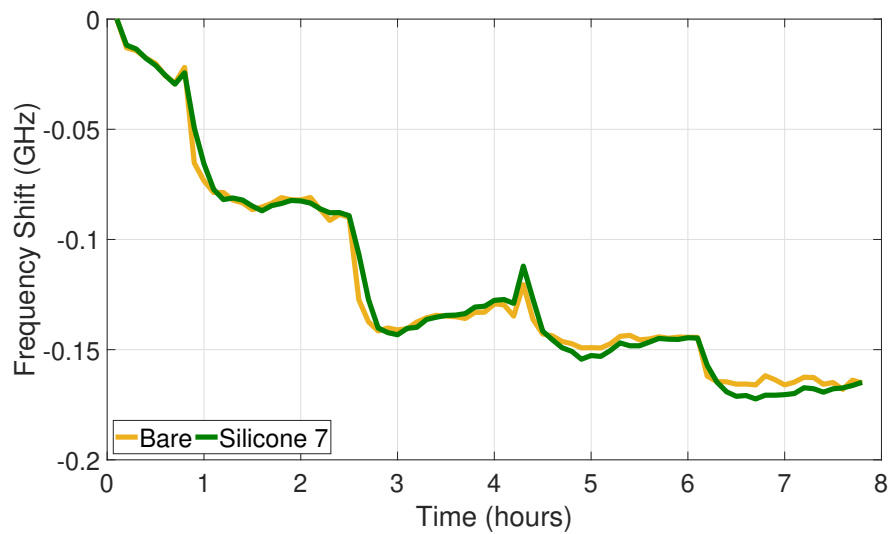


Figure 4.26 – Silicone-coated fibre sample compared with bare fibre in the RH test at 25°C.

A similar RH test was performed at 0°C, and the climatic conditions are shown in Figure 4.27.

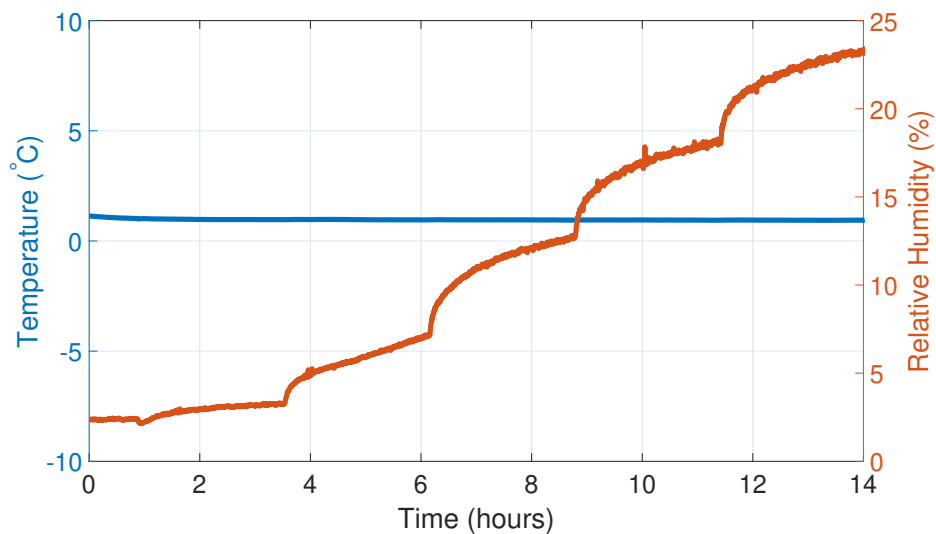


Figure 4.27 – Climatic chamber conditions during the RH test at 0°C.

Figure 4.28 shows the frequency shifts of all fibres during the RH test at 0°C.

At 0°C the behaviours of the silicone-coated fibres and the bare fibre are again similar. At lower temperatures the desolite-coated fibres starts to be RH sensitive, as seen in the previous sections, while the silicone-coated fibres remain completely insensitive to RH. Figure 4.29 shows a detailed comparison between one silicone sample and the bare fibre and demonstrates, again, that at 0°C the silicone-coated fibres remain a perfect temperature sensor.

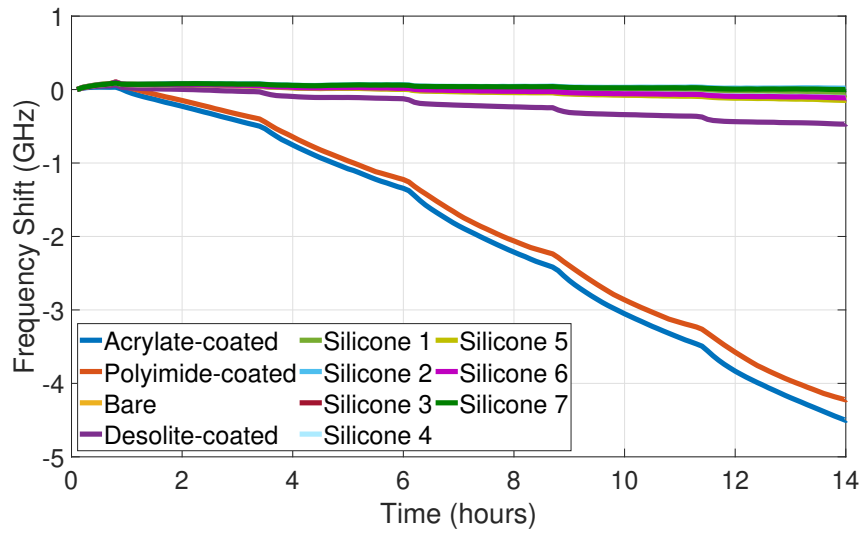


Figure 4.28 – Frequency shifts of all fibres during the RH test at 0°C

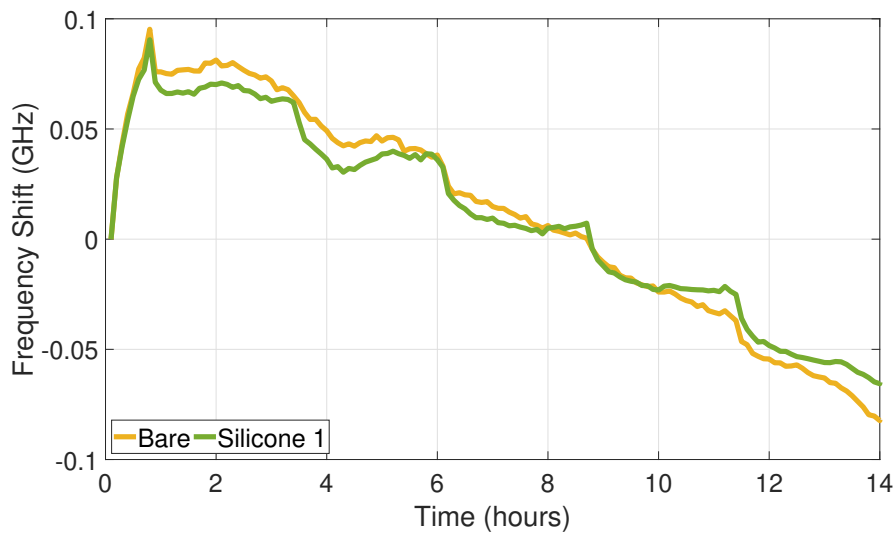


Figure 4.29 – Silicone-coated fibres compared with bare fibre in the RH test.

A similar analysis and similar results were obtained in a RH test at -20°C, presented in Figure 4.30. Figure 4.31 shows the fibre responses during the RH test at -20°C.

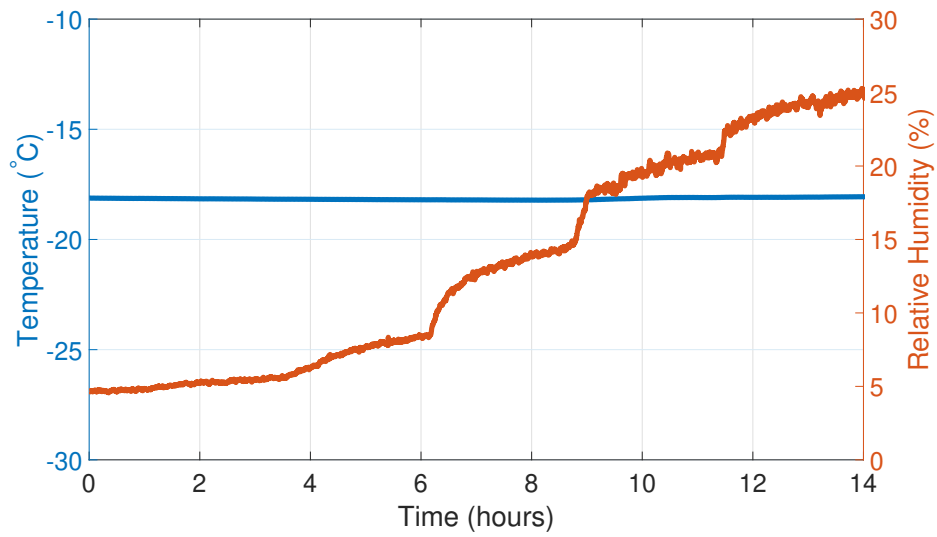


Figure 4.30 – Climatic chamber conditions during the RH test at -20°C.

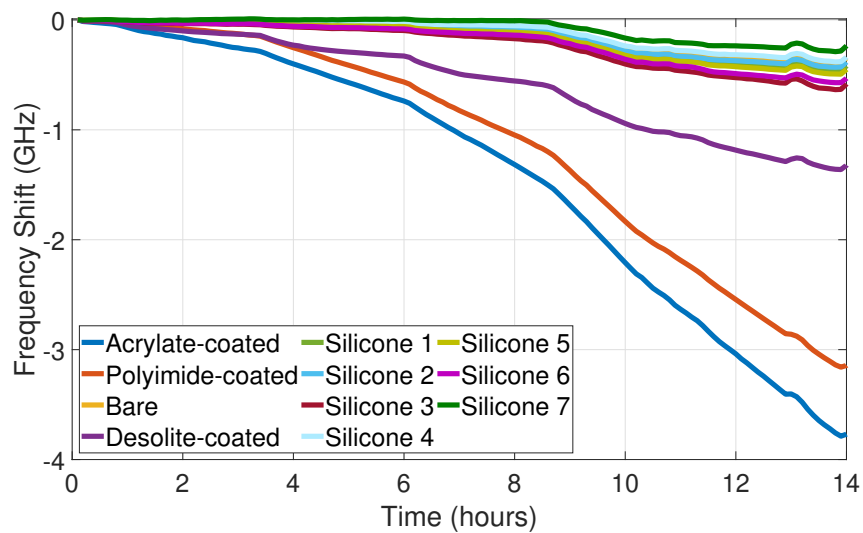


Figure 4.31 – Silicone-coated fibres compared with bare fibre in the RH test at -20°C.

At -20°C, the behaviour of the silicone-coated fibres remains completely insensitive to RH, following perfectly the bare fibre. Analysing individually one of the samples and comparing with the bare fibre, one can conclude that the traces closely coincide, as seen in Figure 4.32.

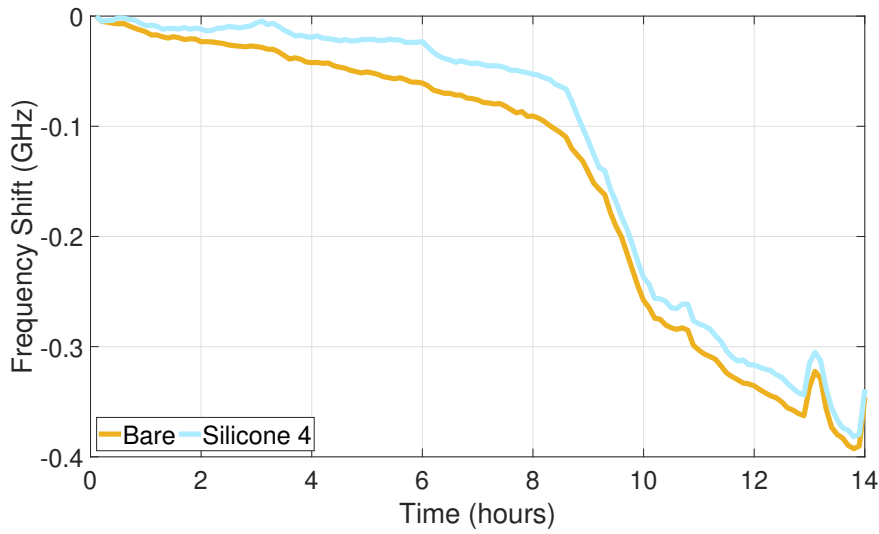


Figure 4.32 – Silicone-coated fibres compared with bare fibre in the RH test at -20°C.

A final RH test at 55°C was also performed to complete the analysis of the silicone-coated fibres at higher temperatures. The climatic chamber conditions are presented in Figure 4.33.

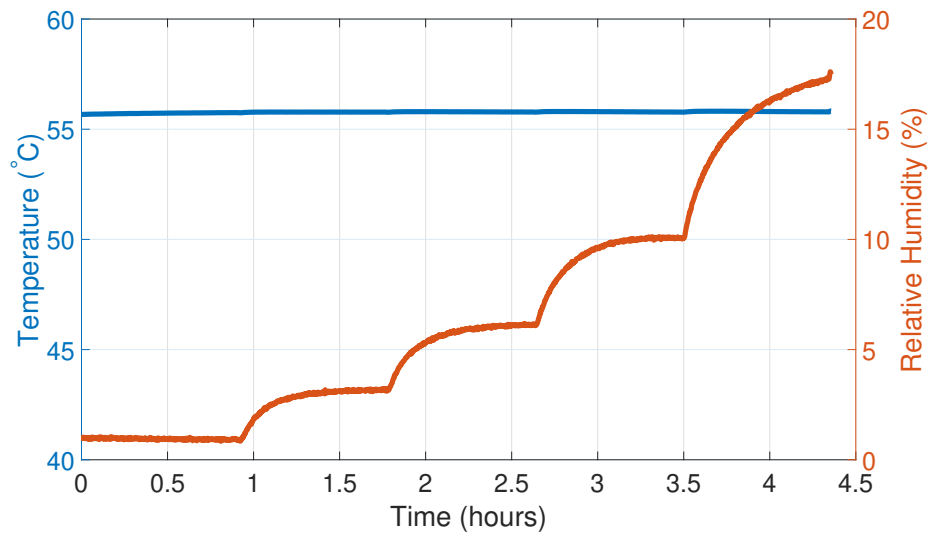


Figure 4.33 – Climatic chamber conditions during the RH at 55°C.

Figure 4.34 and Figure 4.35 show the response of the full FUT during the RH test and the comparison between one silicone-coated sample and bare fibre, respectively. Once more, the silicone-coated fibres appear immune to RH variations at 55°C.

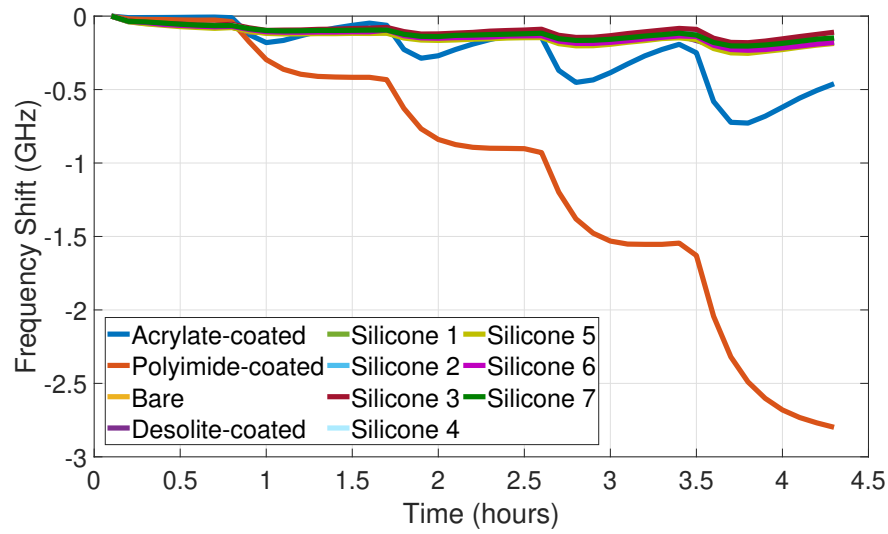


Figure 4.34 – Silicone-coated fibres compared with bare fibre in the RH test at 55°C.

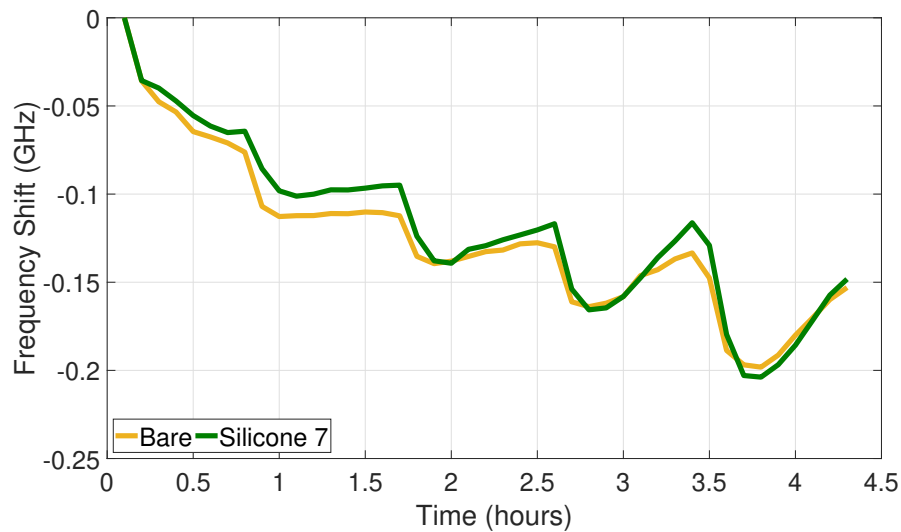


Figure 4.35 – Silicone-coated fibres compared with bare fibre in the RH test at 55°C.

4.3.3 Conclusions

This section proves that the silicone-coated fibres are, among all the coated optical fibres testes in this dissertation, the best candidates to be the temperature reference in the thermo-hygrometer distributed fibre sensors. When coated with a thin layers of silicone, the optical fibre has the same response as a bare optical fibre, in the tested temperature range, whilst being protected with a coating. Silicone-coated fibre is a valid solution to solve the temperature-RH cross-sensitivities issue, as it can be considered a pure temperature distributed fibre sensor.

4.4 Conclusions

The conclusions of this chapter can be summarized as follows:

- The temperature-RH cross-sensitivities issue was solved.
- Desolite-coated fibres are strong candidates to serve as temperature reference, in applications above 15°C. They are easy to manufacture and low cost.
- Using the same desolite coating but with thicker thickness, the temperature sensitivity increases significantly, specially at lower temperatures. The temperature sensitivity is approximately 6 times higher than the temperature sensitivity of the standard SMFs.
- Silicone-coated fibres increase the range of temperatures across which the optical fibres are immune to RH. From -20°C to 55°C they can be considered a pure temperature sensor.

5 Distributed Thermo-hygrometer Fibre Sensor for Concrete Applications

Chapter 5 presents an application case where the developed distributed thermo-hygrometer sensor was installed, tested and validated [110]¹. After selecting a pair of coated optical fibres, the setup monitored temperature and RH simultaneously inside a concrete block from the very first moment of its curing process.

Nowadays, concrete is the second most consumed material on Earth, after water, and is currently present in the large majority of the constructing structures. Most of the European developed countries spend around half of their infrastructure budgets on repairs, maintenance, demolish and the replacement of existing structures, and a large percentage is due to wrong practices in the building techniques used in the past and the present [111]. Most of the problems cannot be completely understood because there is no way to know precisely what is occurring inside concrete structures, as they are opaque, and larger constructions like tunnels or pre-cast panels make it impossible to inspect.

During the lifetime of a concrete structure, parameters such as temperature, humidity or moisture, load, pH, corrosion rate and pressure should be strictly monitored to guarantee the good health of the structure. One of the most important and critical parameters is the moisture content in the concrete pores, which is responsible for most of the degradation processes such as shrinkage and cracking. The concrete mix is a semi-fluid for the first few hours of the curing and the process is an exothermic reaction that generates a lot of heat and expels of moisture. The chemical reaction between water and cement is initialized as soon as water is added to the mix, although its effect may be not apparent for the first few hours.

The full curing process is usually set to 28 days but is severely dependent on concrete constituents, mix proportions and weather conditions [112]. If it takes fewer days, a monitoring solution might offer savings in terms of time and resources, whereas insufficient curing might lead to catastrophic and irreversible damage. During the drying process, which starts from the surface layer, the concrete moves from a saturated to a partially saturated state, which cause capillary tensions in the pore water, and, when these tensions exceed the tensile strength,

¹In the moment of this dissertation submission, the publication was under review.

cracks will naturally grow up [113, 114]. Hydration reactions are very slow during the first 3/4 hours of concrete's life but accelerate over the following 8-12 hours when the concrete changes from the semi-fluid state into a more rigid. In this time frame of 8 to 12 hours, which is the most critical period in the lifetime of concrete structures, lack of moisture has adverse effects and results in shrinking and cracking at a very early age and repeated failures at this period have an irreversible impact on the durability, strength and fire resistance [115]. In fresh consolidated concrete, water occupies the uneven spaces between cement and aggregate particles, and as the magnitude of the shrinkage strain is usually proportional to the amount of moisture lost, a gradient of shrinkage is evident [116].

Windbreaks, fog spraying, and evaporative retarders are some techniques employed to address the loss of moisture but, the easiest one is to irrigate the concrete during the initial stage of curing, keeping it humid enough to avoid cracks. Nevertheless, this technique acts only as blind prevention, and if the concrete is still humid, it has no effect and is a waste of resources and money. On the other hand, if the concrete dries too fast, more water is needed and immediate intervention is required.

Two categories of cracks can appear: immediate cracking that happens after few hours due to internal and external stress gradient; and later cracking caused by the weaknesses left by the early-age shrinkage. Beyond the losses of load capacity, concrete with cracks allows water and other liquid chemical agents to penetrate and weaken the internal structure and, even though it may not affect the structural integrity, aging and durability problems are generally increased and a precise monitoring system is needed [117]. In the case of tunnels, the position where one observes water leaking in concrete does not always correspond to the position of the water source, because the crack is the natural path for the water and not the origin. The misinterpretation of the crack as the origin of the leak can lead to a false positioning of the place to intervene.

During the curing of concrete, a phenomenon called bleeding can be evidenced. Bleeding refers to the process where the settlement of heavier solid particles such as cement, pushes upward some water to the surface. Some bleeding is normal but excessive can be problematic because it turns the structure extremely heterogeneous [118]. Some techniques such as creating holding grids at different levels reduce the negative impact of bleeding in concrete.

The correlation between the concrete moisture and shrinkage strain in small structures was already investigated by a few authors [119, 120] and S. Taheri compile a review on five key sensors for monitoring of concrete structure [121]. For example, in 2014, T. Geernaert et al. presented the first study using Microstructures Optical Fibre Bragg Grating-based (MOFBG) sensors for strain and temperature monitoring inside a concrete buffer of the Belgian supercontainer concept [122]. The use of two MOFBGs, with a temperature compensation mechanism, allows simultaneous measurements of strain and temperature, but only in the location where the sensors are installed. Later, in 2018, L. Pelecanos et al. developed a distributed fibre optic strain sensor for monitoring the actual field behavior of axially loaded piles [123]. The

system is based on a BOTDR, with two optical fibres for temperature compensation, and is able to provide a continuous profile of the induced strain within piles and a clear view of the condition of the whole structure. The profile of the induced strain indicates the localised regions of weakness, inhomogeneity or strain concentration, overcoming the limitation of discrete monitoring systems.

As seen in the previous studies, different authors studied the temperature and strain inside concrete, however, as of today, although there are only a few solutions to measure punctually moisture [124] or temperature [125] inside concrete, there is no evidence of a solution offering simultaneous and distributed measurement of temperature and RH for large concrete structures with kilometres of sensing range.

In this study, we present a novel technique, based on the distributed fibre optic sensors technology, to measure simultaneously temperature and relative humidity directly inside a concrete structure using a set with two optical fibres and a single optical interrogation system. The technology provides a comprehensive view of the curing process and when mapped with the properties and curing charts of concrete, an absolute view of the strength and failure points of concrete. In summary, the presented technology provides an unique and important monitoring information system during four different moments:

- The need of water during the initial irrigation step;
- Determination of the correct moment to strip the concrete formwork;
- Temperature and moisture stabilization of concrete;
- Continuous monitoring of the structural health for the entire concrete lifetime.

5.1 Experimental Setup

The home-made optical interrogator setup behind the distributed temperature and RH measurements is fully described in Section 3.1.1. The selected fibres for this test were a polyimide-coated fibre with 4 layers of coating and a desolite-coated fibre with 26.5 μm of coating thickness, due to its RH insensitivity at temperatures above 15°C [90, 104]. The desolite-coated fibre was used as temperature reference for the RH measurements acquired with the polyimide-coated fibre. The optical fibres were properly isolated from the mechanical stress with a permeable silicone wrap tube, as seen in Figure 5.1 and with a permeable tissue to avoid the direct contact with solid concrete fragments.

The data analysis methodology was already demonstrated in Section 3.2.2 but, in summary,

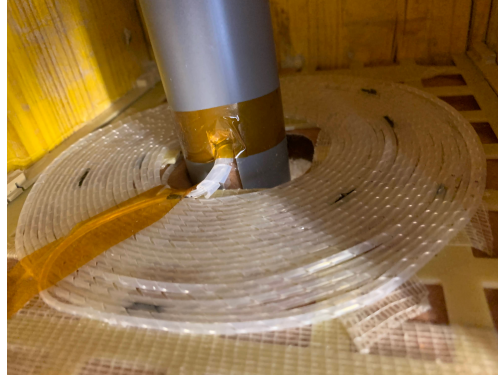


Figure 5.1 – Permeable silicone wrap tube in which the selected optical fibres were inserted.

the equations to calculate temperature and RH are:

$$T = \frac{\Delta F_{Des}}{S_{T_{Des}}} + T_0 \quad (5.1)$$

$$RH = \frac{\Delta F_{PI}}{S_{RH_{PI}}} + RH_0 \quad (5.2)$$

where ΔF_{Des} and $S_{T_{Des}}$ are the frequency shift of the desolite-coated fibre, which is only temperature dependent, and the temperature sensitivity of the desolite-coated fibre, respectively. ΔF_{PI} is the frequency shift of the polyimide-coated fibre already temperature compensated and $S_{RH_{PI}}$ is its RH sensitivity. T_0 and RH_0 are the initial temperature and RH measured by the electronic references.

5.1.1 Setup Preparation

A parallelepiped shaped holding box of 25x25x50 cm was prepared beforehand and the full schematic of the test is shown in Figure 5.2.

The two optical fibres are coiled together in a spiral configuration, to increase the length of the fibre, in three different positions: base, middle and top. In the centre of each position, one temperature (PT100) and RH (HIH4000) electronic references were installed. All the electronic sensors were properly calibrated and were inserted in a PVC tube that was also used to pass the optical fibres from one level to the other. The electronic references, which are not embedded in concrete, provide the initial references values used to convert the optical fibres frequency shift to temperature and RH. The lower end of the PVC tube was initially closed with a thermal sponge to avoid the dispersion of water residuals. A temperature and a RH sensor

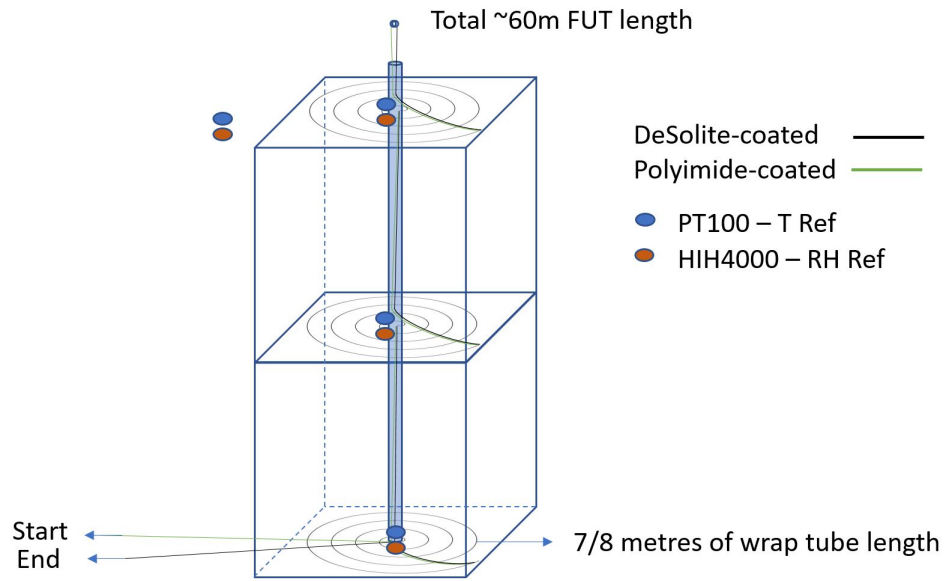


Figure 5.2 – Full schematic of experimental setup.

were additionally placed outside for monitoring the environmental conditions.

The concrete used for this test was a sample of the concrete used in the final lining of the new tunnels of the High Luminosity Large Hadron Collider (HL-LHC) of CERN. It is a C35/45 minimum strength class, XC4 exposure class, with a cement of 42.5 type I, II and aggregates of 32 mm maximum. Normally, the concrete should have reached the required 8 MPa after approximately 12 hours, but if the mass concrete achieves a much higher hydration heat than concrete in small quantities, it cures much faster.

Figure 5.3 shows photographs of: the wood formwork before and after pouring with concrete, still in the HL-LHC working area; the moment where the measurements started in the laboratory; the concrete block after few days of curing.



Figure 5.3 – Wood formwork before and after pouring concrete, and concrete block after a few days of curing.

5.2 Experimental Results

The results section is divided into 3 parts: 1) Temperature analysis. 2) Relative humidity analysis. 3) Three-dimension general analysis of temperature and relative humidity.

5.2.1 Temperature Analysis

The temperatures measured by the 4 electronic references temperature are shown in Figure 5.4.

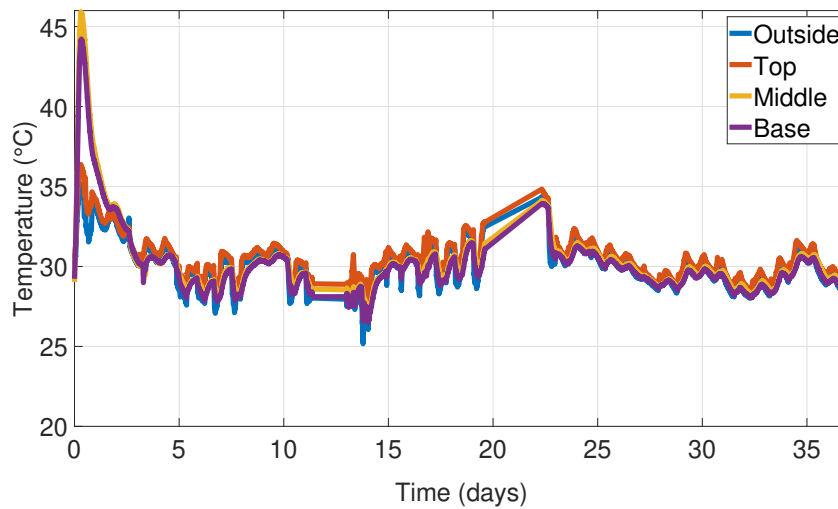


Figure 5.4 – Reference temperature measured by PT100 during the 37 days of testing.

The test lasted 37 days and, as expected, the temperature of the concrete block increased in the first 12 hours due to the nature of the exothermic reaction of the curing of the concrete. The maximum temperature reached was around 46°C in the middle of the concrete, while in the base it reached 44°C. On top of the block, mostly because the reference sensor was partially in direct contact with environmental air, the temperature was lower and reached 36°C. The temperature outside, which increased due to the heat generated by the concrete, reached a maximum of 35°C. After reaching the maximum, the temperature naturally decreased until reaching the room temperature. The periodical oscillations observed are the day/night fluctuations of the laboratory temperature. During the test, there were two acquisitions interruptions that resulted in some missing data represented by the straight lines in the plot.

The spatial resolution of the interrogator was set to 1 metre, so as the total length of each fibre in each stage is around 6/7 meters, we are able to distinguish 6/7 different points. Nevertheless, due to some losses caused by the splicing between each fibre, the extreme points are ignored and only 5 points of temperature and 5 points of RH for each stage of measurement are considered. All the plots of this section show the individual variations of the 5 different regions per stage of measurement, distributed in a spiral configuration, as

explained in Figure 5.5.

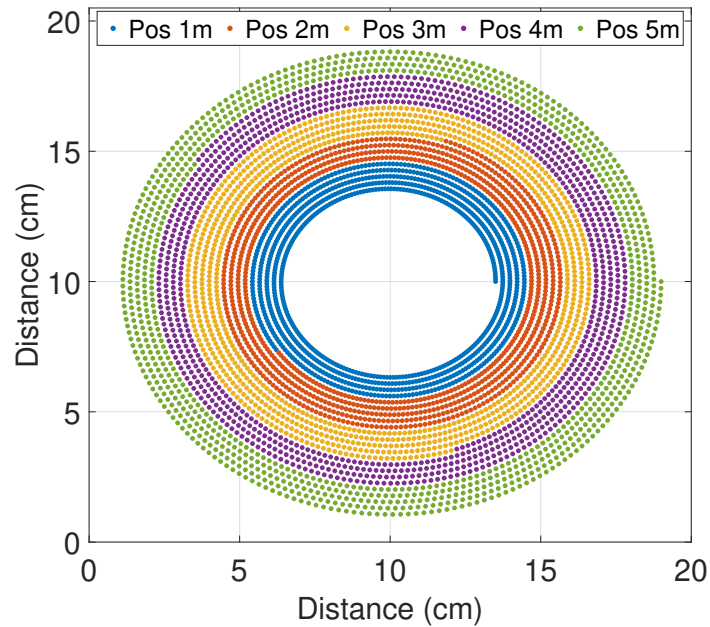


Figure 5.5 – Fibre distribution in a spiral configuration.

The temperature measurement results at the bottom, in the middle and at the top of the concrete block are shown in Figure 5.6, Figure 5.7 and Figure 5.8, respectively.

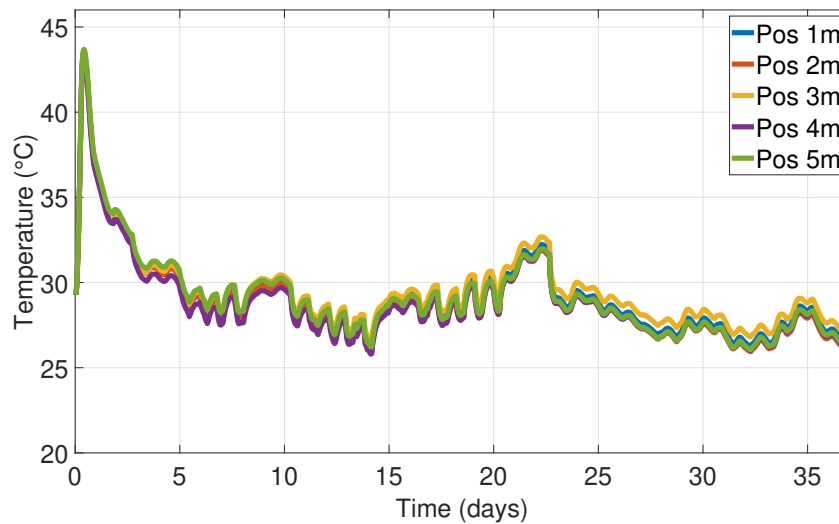


Figure 5.6 – Temperature measured by the desolite-coated fibres at the base of the block.

At the beginning of the curing process, the temperature at the base of the concrete block reached a maximum of around 44°C after 12 hours, and started to decrease afterwards. The

fluctuations present in the plots are the real fluctuations of the day/night temperature of the room, as confirmed by the reference temperature sensors.

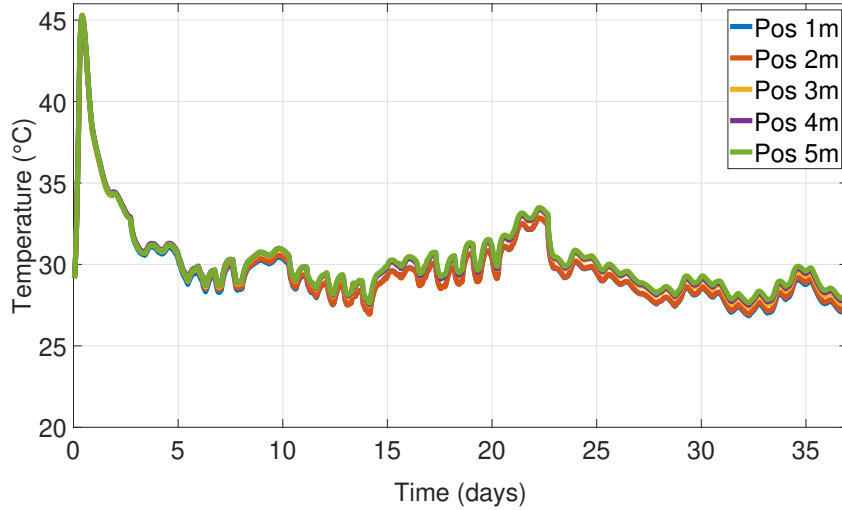


Figure 5.7 – Temperature measured by the desolite-coated fibres in the middle of the block.

In the middle of the concrete, a maximum temperature of 45°C was reached, as shown in Figure 5.7. Both in the middle and at the base, the maximum temperature difference between the regions in the same plane was inferior to 1°C.

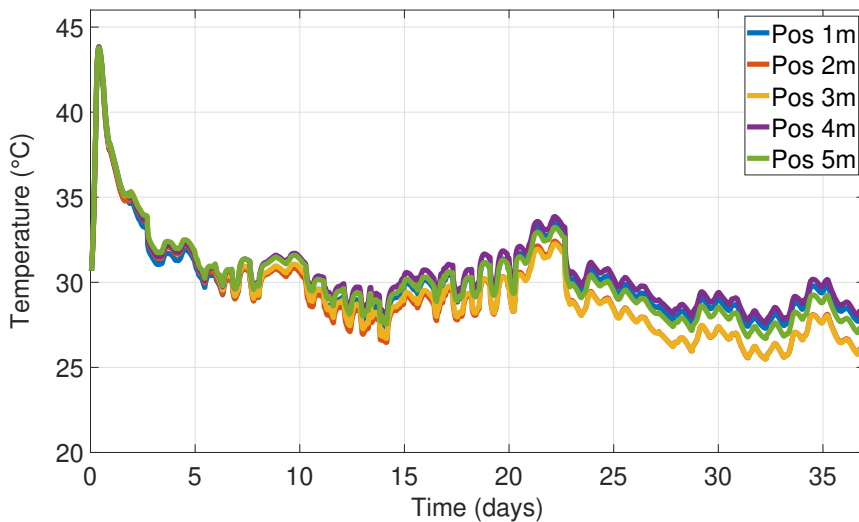


Figure 5.8 – Temperature measured by the desolite-coated fibres on the top of the block.

At the top of the concrete, the temperature variation follows the same trend as the previous measurements, but with a slight distinction in terms of difference between the regions in the same plane, expressed by the spread of the curves, as Figure 5.8 shows. In this case, the

maximum difference between the regions in the same plane is around 2.5°C. This higher variation is explained by the imperfect way that the fibres were embedded at top of the concrete, and only a thin layer of heterogeneous concrete was placed between the air and the fibre, as shown in Figure 5.9. The same happened at the base, but as the lower wood holder was kept until the end of the test, the contact with air was negligible and the differences between the regions were not significant.



Figure 5.9 – Imperfections in the concrete structure.

The first conclusion of this analysis is that the block can be considered thermally stable after 5 days. In the meantime, even if a temperature gradient can be observed between the 3 levels, the temperature does not change significantly inside the concrete block.

As the temperature measured by the desolite-coated fibres is used as a reference for the polyimide-coated fibre, a comparison with the electronic reference is needed, to verify if the temperature reference is correct. Figure 5.10 shows the variation of the electronic temperature reference placed in the middle of the concrete and one of the temperature measurements from the desolite-coated fibre also from the middle of the concrete.

As expected, the temperature variations measured by the fibres agree well with those measured by the reference temperature sensors. The observed differences are of the same order of magnitude as the PT100 precision (1°C).

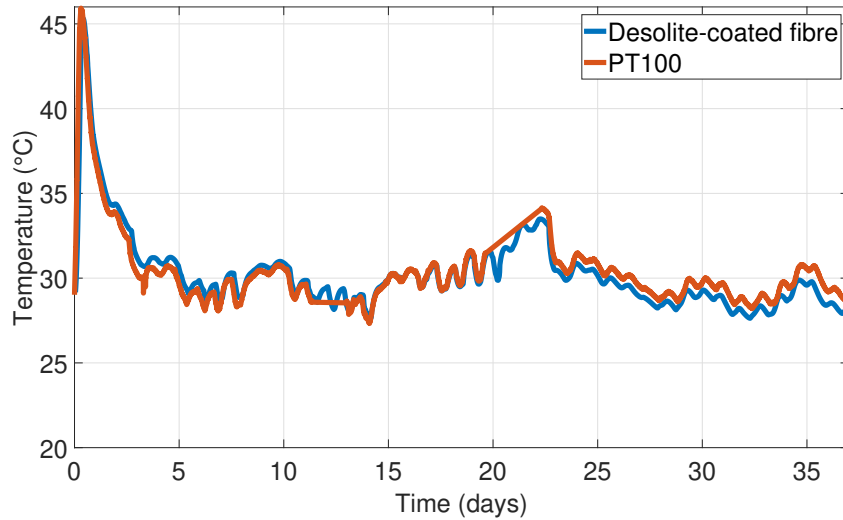


Figure 5.10 – Comparison between the electronic reference and one fibre's measurement.

5.2.2 Relative Humidity Analysis

The RH electronic reference measurements of the full test are plotted in Figure 5.11.

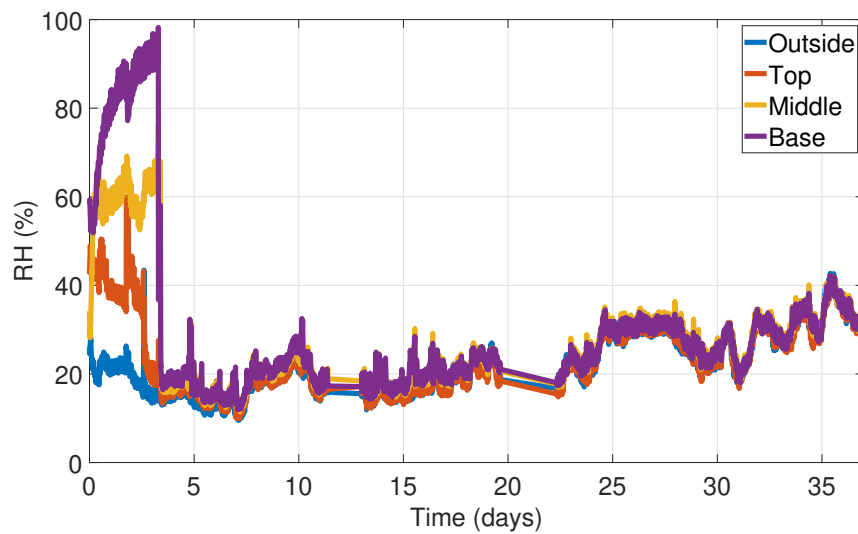


Figure 5.11 – Reference RH measured by HIH4000.

The RH reference sensors were not embedded in concrete and, consequently, the initial value of the RH was not an accurate reference for the optical fibres measurements. As the PVC tube was closed in the lower end, the humidity at the base naturally increased due to the accumulation of water in the tube. At the moment that the cover was removed, after 4 days, the environmental air started to circulate inside the tube and all sensors measurements dropped significantly to the environmental RH. After that moment, all sensors reacted similarly with

a negligible variation between all of them. At the end of the test, the reading of all sensors agreed, which means that the RH is uniform in the environment.

Due to the impossibility of having a precise initial RH value, because the RH references were not embedded in concrete, a corrective factor was applied at each stage of measurement. Given that the concrete is semi-fluid at the start, and as can be understood from literature as well (see e.g. [114]), the RH can be estimated to be near its saturation value of 100%.

Figure 5.12, Figure 5.13 and Figure 5.14 present the RH variations of the 5 points at each measurement position: base, middle and top of the concrete block respectively.

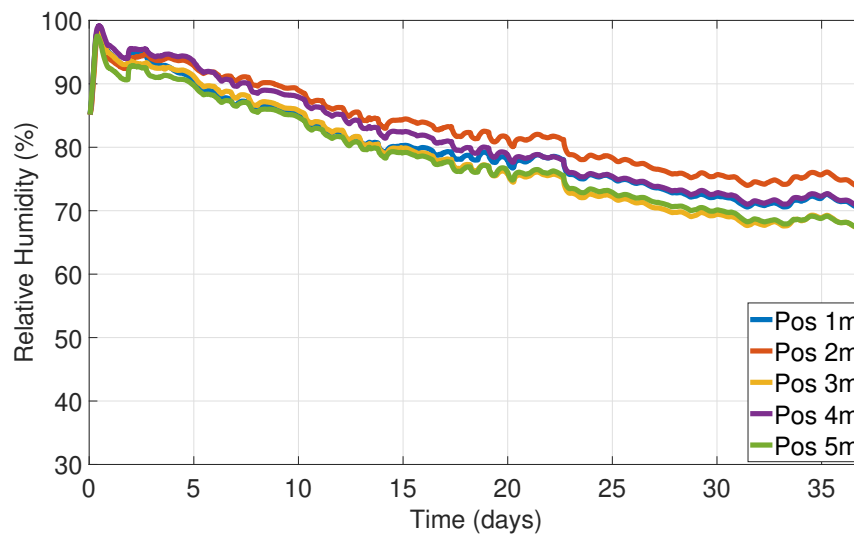


Figure 5.12 – RH measured by the polyimide-coated fibres on the base of the block.

As expected, the RH increased at the beginning because the fibres took some time to absorb water molecules from the semi-fluid concrete. After reaching the maximum of the RH, it started to slowly decrease, as concrete starts to expel water vapours. Figure 5.12 shows that in the base of the block, the RH took around 31 days to stop the descent trend, losing around 30% and stabilized around 70%. The maximum difference between points at the base is around 8%, which is expected due to the random position of the aggregates and water inside concrete [126].

The RH measurements in the middle of the block, presented in Figure 5.13 are similar, but the stability was reached before, around 27 days. In terms of RH losses in the middle of the concrete, they were situated around 20% and the maximum difference between the points is around 5%.

The lower losses of RH, compared with the losses at the base, are explained by the exposure of the fibres at the base to the environmental air, as shown in Figure 5.9. The fibres in the middle were completely embedded and for that reason, more water molecules were trapped between the concrete aggregates.

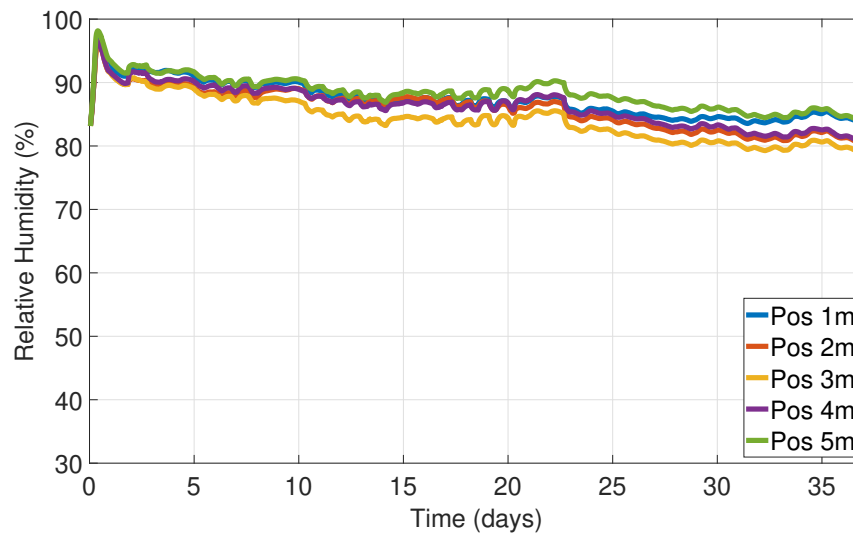


Figure 5.13 – RH measured by the polyimide-coated fibres in the middle of the block.

The RH variation at the top of the block showed a different behavior compared with the other levels, as Figure 5.14 presents. The maximum value of RH was not reached at the beginning of the test but only after 5 days of curing.

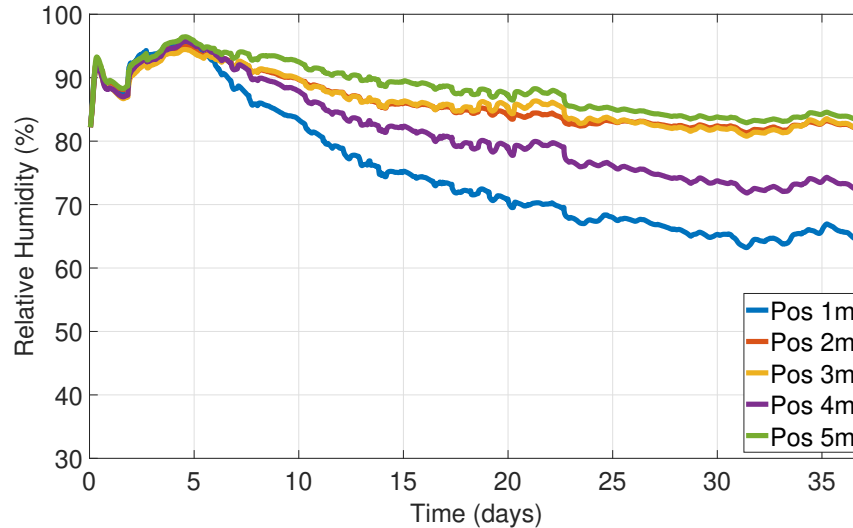


Figure 5.14 – RH measured by the polyimide-coated fibres on the top of the block.

This is explained by the bleeding effect in concrete that brings the water upwards while the heavier aggregates accumulate on the base [118, 127]. If at the beginning of the test, the majority of water tends to be pushed downwards due to its low viscosity compared with the semi-fluid concrete, after a few days of curing, it is pushed upward because of the settlement of heavier aggregates. Nevertheless, the stability was reached after 25 days but, the maximum

variation between the points at the same level is significant and around 20%. This is caused by the heterogeneous and thin layer of concrete that is placed between the fibres on top and the air, which makes part of the fibre completely embedded in the concrete and part in contact with air.

A final comparison between the RH reference sensors and the polyimide-coated response was performed and shown in Figure 5.15.

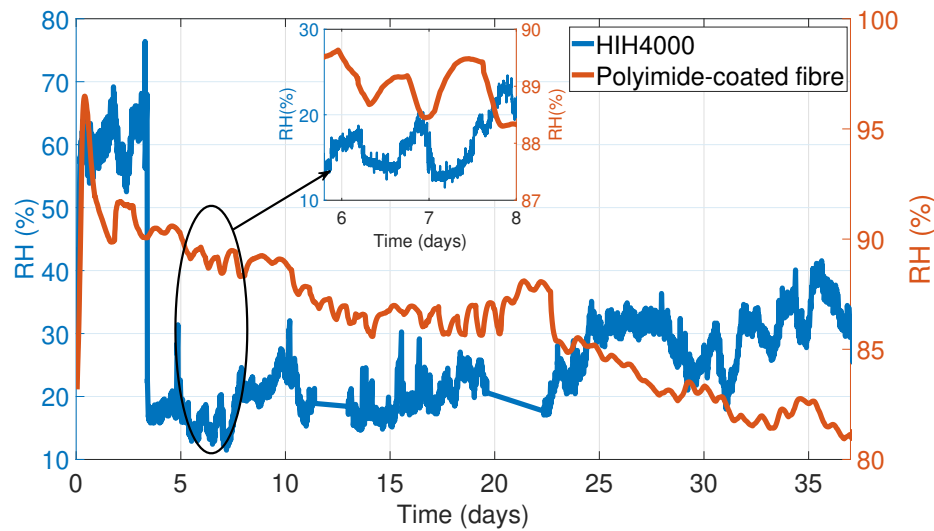


Figure 5.15 – Comparison between the electronic reference and one fibre measurement in the middle of the block.

It is important to note that the RH reference sensor was in contact with air and not embedded in concrete, where a large amount of water molecules are trapped. This creates a significant difference and for that reason, the two traces are not comparable, but their variations can be analysed. The inset plot of Figure 5.15 shows that the polyimide-coated fibres follow the variation of the environmental RH but with a delay of some hours. The peaks are shifted and this is expected because the concrete acts as a sponge that slowly absorbs and releases the environmental RH. As the fibre was completely embedded, the variation of RH takes some hours to be detected. These similarities in the trends of both signals can be observed many times over the full length of the test.

During the curing process, RH was analysed at a specific moment when some water was added at the top of the concrete. At the moment when the water was added, the RH responses of the polyimide-coated fibres, already temperature compensated, were stable and the three of them reacted differently, as shown in Figure 5.16.

The fibre at the top of the concrete reacted immediately to the water, because the water reached that fibre immediately, while the fibre in the middle reacted after 6 minutes. That is expected because the water needs some time to penetrate into the concrete. The fibre at

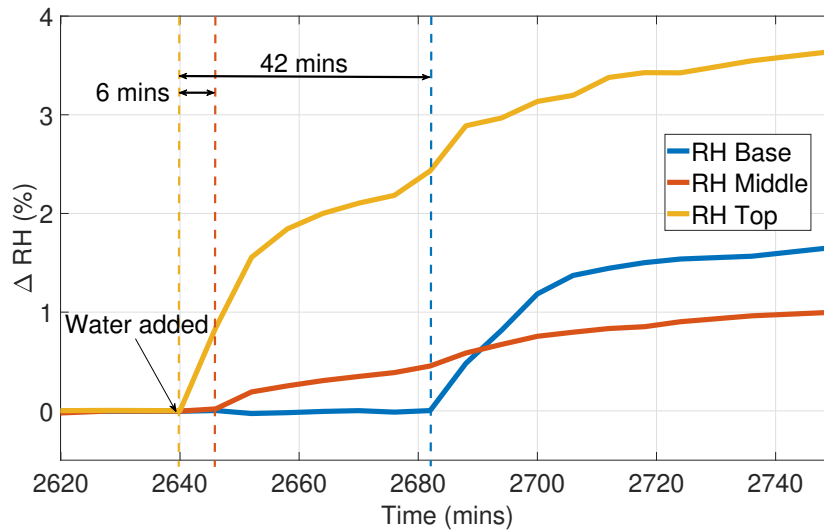


Figure 5.16 – Response of the polyimide-coated fibres after adding water at the top of the block.

the base reacted only after 42 minutes because there was much more concrete to penetrate. In terms of the magnitude of the RH variations, the fibre at the top was the one with higher variations of RH, because was the drier fibre when the water was added and had more capacity of absorbing. In the middle, the RH was initially higher and for that reason, the fibre was not able to absorb the same amount of water than the fibre on top. The same explanation can be used for the fibre on the base, where the variation of RH was lower than the variation on the top, but as the base accumulated some water, the variation was slightly higher than the variation in the middle.

5.2.3 Three-dimensional General Analysis

After the individual analysis of temperature and RH per level of measurement, this section presents the full analysis of the block at 4 different moments of the curing process. The first moment was 1 hour after the curing start and the results are presented in Figure 5.17.

Figure 5.17 shows that at the beginning of the test, the temperature at the base was slightly higher than in the rest of the block, as expected, because the block was opened at the top and completely closed at the bottom. The same happened with humidity, 1 hour after the curing had started, there was a large amount of water on the base on block, as shown in the right plot. The low viscosity of water, compared with aggregates and cement, pushes it downwards.

The second moment was 12 hours later, when the concrete reached the maximum temperature during the exothermic reaction. The highest temperature, of around 45°C, was reached at the middle of the block, as seen in in Figure 5.18, while the RH was almost saturated at the base.

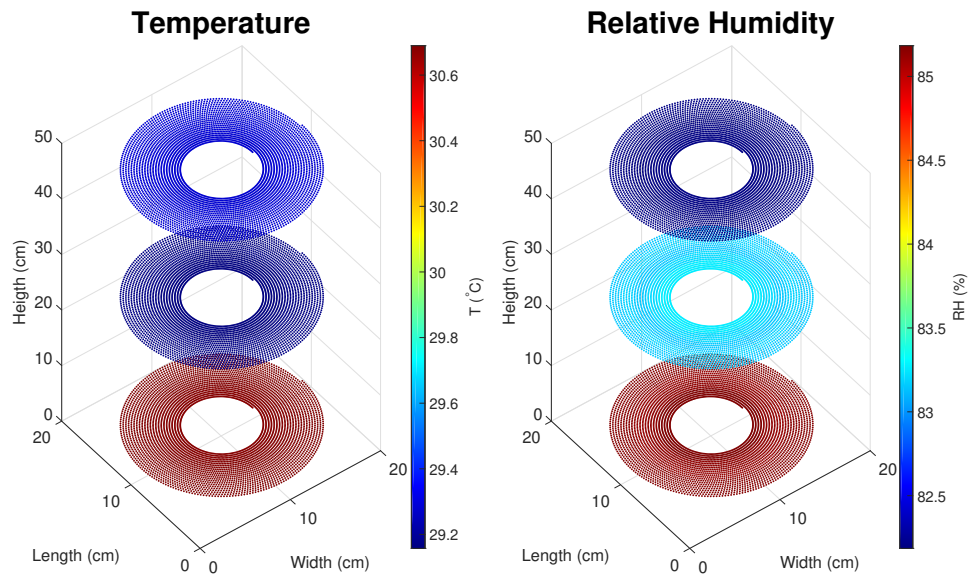


Figure 5.17 – Temperature and RH measurements after 1 hour of curing.

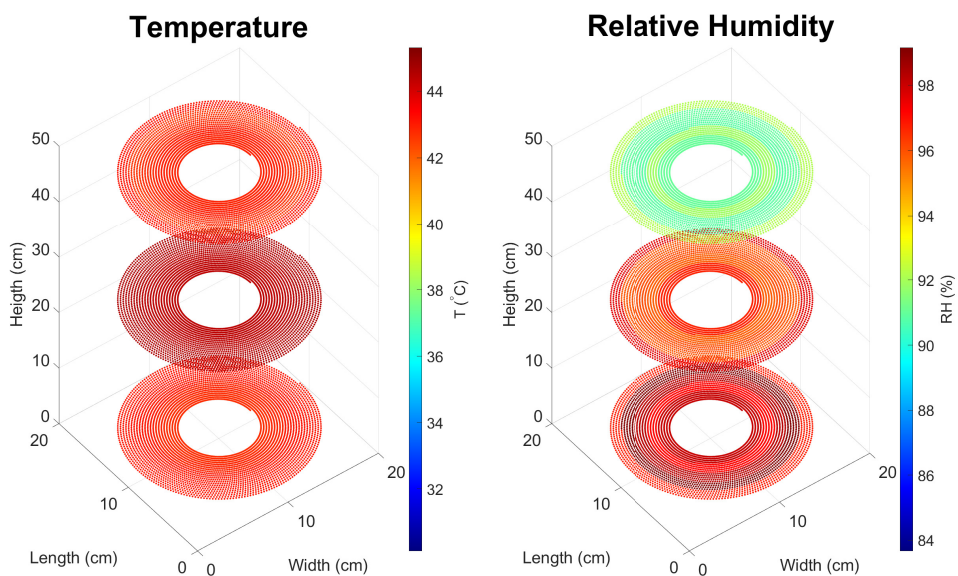


Figure 5.18 – Temperature and RH measurements after 12 hours of curing.

After 2 days, both temperature and RH started to decrease, starting from the top due to the interaction with environmental air, as shown in Figure 5.19. At that moment, there is still an excess of water at the base, which explains why the RH remains higher in the lower part of the concrete.

By the end of the test, after 37 days, the temperature readings remained stable at room

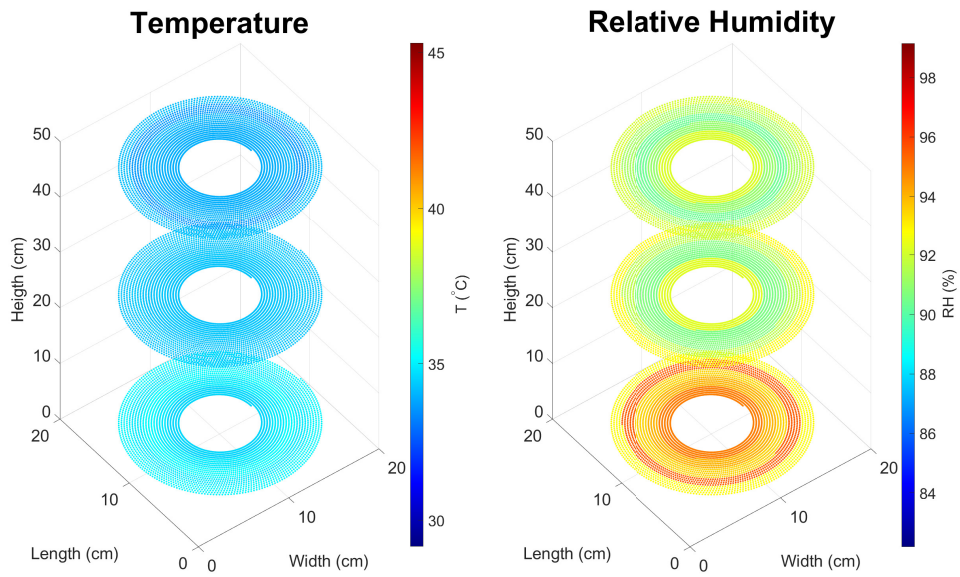


Figure 5.19 – Temperature and RH measurements after 2 days of curing.

temperature, with negligible variations from level to level, as shown in Figure 5.20. The concrete block, after suffering the effect of bleeding, presented a significant reduction of RH at the base, while the differences in the RH measured in the middle were negligible. At the top, due to the interaction with air, there were significant variations of RH.

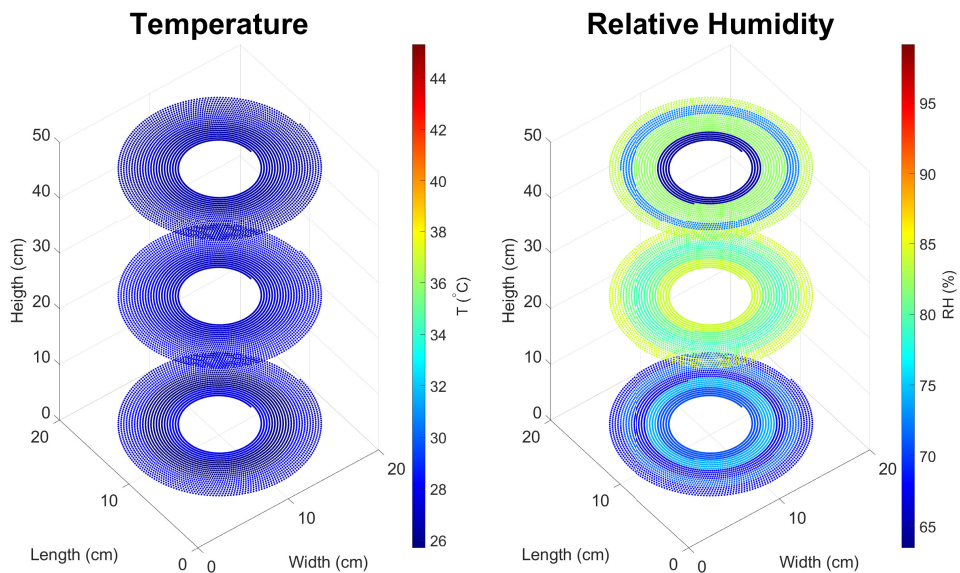


Figure 5.20 – Temperature and RH view measurements 37 days of curing.

5.3 Conclusion

The main conclusion of this study is that the first distributed thermo-hygrometer, with kilometres of sensing range, to be embedded in concrete was built. The presented solution, which uses a single optical interrogator and a single optical fibre setup, monitored the curing of a block of concrete during 37 days uninterruptedly, and allowed determining when the concrete was thermally stable with negligible variation of RH. The 3-dimensional analysis allowed studying the evolution of both variables during the full curing process. The solution represents an enormous improvement of the structural health monitoring systems for concrete applications, and can be easily implemented in large structures such as tunnels, bridges or pre-cast concrete panels.

6 Conclusions and Research Perspectives

The main objectives of this dissertation were successfully achieved. First of all, the first RH distributed fibre sensor with kilometres of sensing range, something never done before, was built. To reach that, the best optical fibres for RH measurements were identified and it was concluded that the polyimide-coated fibres are the best candidates for a RH distributed fibre sensor. Then, it was also discovered that the standard acrylate-coated fibres used in most of the distributed fibre sensors show a non-negligible RH sensitivities. The effect of RH in acrylate-coated fibres was completely overlooked in previous studies and this dissertation demonstrates that it can not be disregarded. Apart from the non-negligible RH sensitivity, the acrylate-coated fibres show drastic differences in their response to RH at different temperatures. Surprisingly, the RH sensitivities increase significantly at lower temperatures and vanish entirely at high temperatures. Additionally, the difference between standard acrylate-coated fibres from different manufacturers is also significant, which means that the RH sensitivity should be addresses distinctively and can not be considered similar to all fibres of the same kind of coating.

Given that the acrylate-coated fibres are also RH sensitive, and as temperature and RH are two parameters that can not be separated without a decoupling method, a new search for a RH insensitive fibre was initiated. The RH insensitive fibre would be used as a temperature reference in a thermo-hygrometer distributed fibre sensor. First of all, different desolite-coated fibres were produced due to its fast and low-cost production. Desolite shows a low coefficient of RH expansion, and several coating thicknesses were produced in order to evaluate their RH sensitivity. The results demonstrated that the thinner coated fibres (26.5-27.5 μm) using desolite coatings are completely RH insensitive at temperatures above 15°C and with a negligible RH sensitivity at lower temperatures. The same fibre samples were also found to be extremely sensitive to temperature, if the coating thickness was 280-322.5 μm . Their temperature sensitivity can be 5 times higher than the standard acrylate-coated fibres at negatives temperatures and can provide a measurement error in the order of 0.2 mK. However, their non-linear behaviour complicates the data analysis.

Most of the applications at CERN experience an environment with temperatures below 0°C, and in order to apply a good temperature reference, a RH insensitive at negative temperatures should be found. Based on the well-known hydrophobic properties of silicone, 7 samples of silicone-coated fibres were produced. The results prove that a silicone-coated fibre is completely insensitive to RH in the range of temperatures from -20 to 55°C. A pure temperature reference was found and completed the best suitable pair of fibres for a thermo-hygrometer sensors. In summary, the developed system seems to provides an adequate solution to measure environmental RH within LHC detectors enclosure, in order to avoid any condensation risk, potentially damaging the associated complex electronics. Nevertheless, in order to guarantee to correct performance, a radiation impact study should be performed.

After finding the best pair of coated optical fibres, an in-field application was identified and explored. More than 30 metres of each fibre were installed inside a block of concrete to monitor RH and temperature since the very first moment of its curing process. The objective of this final test was to determine when the concrete block was finally stable and ready for the next step of construction and the system was fully working for 37 days.

This results represent a breakthrough improvement in the civil engineering monitoring solutions because up to the moment, there was not a technology that was able to monitor the RH and temperature in thousands of points inside concrete with a single optical interrogator with a set of 2 coated optical fibres. Additionally, the presented technology provides an unique and important monitoring information system to evaluate the need of water during the initial irrigation step and will provide a continuous monitoring of the structural health for the entire concrete lifetime.

The obtained results open a wide range of continuity projects to be performed in the future:

- The radiation impact study should be performed in the selected optical fibres in order to understand their resistance to survive in the LHC main detectors. The studies should be performed in order to understand the differences in the RH sensitivities, induced by the deformed coating under radiation, but also to identify the maximum sensing length due to the increasing radiation-induced losses in the silica fibre's core. Different optical fibres such as radiation-hard or pure silica fibres should be tested owing to their higher resistance to radiation environments [128, 129].
- Even if the optical interrogators used in the dissertation were not significantly changed from what is available in the state-of-the-art, several optimizations for specific applications should be done. The choice of the components can be optimized in order to miniaturize the setup and to reduce the full cost of the interrogator. Ideally, the optical interrogation should be easily transported to a in-field application. Additionally, the characteristics of the interrogation unit should be explored further. Parameters such as the maximum sensing length, the minimum spatial resolution and the acquisition time can be optimized.

- The RH insensitive fibres found and tested in this dissertation are not commercial products, and in order to turn the thermo-hygrometer distributed fibre sensor a valuable product for applications out of the research environment, either the studied fibres should be produced in large quantities, or a new search for a commercial coated fibre insensitive to RH should be started.

To conclude, this dissertation presents the first complete study of humidity sensing in optical fibres and its validation for concrete curing applications. Together with monitoring large scientific instruments and civil engineering structures, the developed technology may also prove use useful in a range of applications such as water leaking detection in public piping, agriculture, pharmacological and aerospace industry.

Bibliography

- [1] CERN. (2021), [Online]. Available: <https://home.cern/>.
- [2] E. Amaldi, “Rapports aux états membres: présentés par le secrétaire-général du conseil européen pour la recherche nucléaire (cern), 1952-1954”, CERN, Tech. Rep., 1955.
- [3] M. Fossa and P. Petagna, “Use and calibration of capacitive rh sensors for the hygrometric control of the cms tracker”, CERN-CMS-NOTE-2003-024, Tech. Rep., 2003.
- [4] J. Daguin, K. Arndt, W. Bertl, J. Noite, P. Petagna, H. Postema, P. Tropea, and B. Verlaat, “Evaporative co2 cooling system for the upgrade of the cms pixel detector at cern”, *13th InterSociety Conference on Thermal and Thermomechanical Phenomena in Electronic Systems*, 2012, pp. 723–731.
- [5] E. Carrone, A. Tsirou, and P. Verdini, “A discrete event system the cms tracker interlocks”, *proceedings of 10th International Conference on Accelerator and Large Experimental Physics Control Systems, Geneva, Switzerland, Citeseer*, 2005.
- [6] H. Farahani, R. Wagiran, and M. N. Hamidon, “Humidity sensors principle, mechanism, and fabrication technologies: a comprehensive review”, *“Sensors”*, vol. 14, no. 5, 2014.
- [7] G. M. Berruti, “Radiation tolerant fiber optic humidity sensors for high energy physics applications”, Ph.D. dissertation, University of Sannio, Benevento, Italy, 2015.
- [8] F. Berghmans and A. Gusarov, “Fiber bragg grating sensors in nuclear environments”, “Fiber Bragg grating sensors: recent advancements, industrial applications and market exploitation”, 2011.
- [9] X. Bao and L. Chen, “Recent progress in distributed fiber optic sensors”, *“Sensors”*, vol. 12, no. 7, 2012.
- [10] K. C. Kao and G. A. Hockham, “Dielectric-fibre surface waveguides for optical frequencies”, *Proceedings of the Institution of Electrical Engineers*, IET, vol. 113, 1966, pp. 1151–1158.
- [11] J. Ballato and P. Dragic, “Glass: the carrier of light-a brief history of optical fiber”, *“International Journal of Applied Glass Science”*, vol. 7, no. 4, 2016.

-
- [12] S. Girard, J. Kuhnhehn, A. Gusarov, B. Brichard, M. Van Uffelen, Y. Ouerdane, A. Boukenter, and C. Marcandella, "Radiation effects on silica-based optical fibers: recent advances and future challenges", ["IEEE Transactions on Nuclear Science"](#), vol. 60, no. 3, 2013.
 - [13] Z. Fang, K. Chin, R. Qu, and H. Cai, *Fundamentals of optical fiber sensors*. John Wiley & Sons, 2012, vol. 226.
 - [14] D. Gloge, "Optical-fiber packaging and its influence on fiber straightness and loss", ["Bell System Technical Journal"](#), vol. 54, no. 2, 1975.
 - [15] U. Uyor, A. Popoola, O. Popoola, and V. Aigbodion, "Polymeric cladding materials under high temperature from optical fibre perspective: a review", ["Polymer Bulletin"](#), vol. 77, no. 4, 2020.
 - [16] V. I. Busurin, A. S. Semenov, and N. Udalov, "Optical and fiber-optic sensors", ["Soviet Journal of Quantum Electronics"](#), vol. 15, no. 5, 1985.
 - [17] D. A. Krohn and T. W. MacDougall, *Fiber optic sensors*. Instrument society of America Research Triangle Park, 1988.
 - [18] E. Udd, "An overview of fiber-optic sensors", ["review of scientific instruments"](#), vol. 66, no. 8, 1995.
 - [19] B. Culshaw, "Optical fiber sensor technologies: opportunities and-perhaps-pitfalls", ["Journal of lightwave technology"](#), vol. 22, no. 1, 2004.
 - [20] K. Fidanboyly and H. Efendioglu, "Fiber optic sensors and their applications", *5th International Advanced Technologies Symposium (IATS'09)*, vol. 6, 2009, pp. 2–3.
 - [21] B. Culshaw, "Fiber-optic sensors: applications and advances", ["Optics and photonics news"](#), vol. 16, no. 11, 2005.
 - [22] S. Pevec and D. Donlagić, "Multiparameter fiber-optic sensors: a review", ["Optical Engineering"](#), vol. 58, no. 7, 2019.
 - [23] L. Thevenaz, *Advanced fiber optics: concepts and technology*. EPFL press, 2011.
 - [24] K. Hill, Y. Fujii, D. C. Johnson, and B. Kawasaki, "Photosensitivity in optical fiber waveguides: application to reflection filter fabrication", ["Applied physics letters"](#), vol. 32, no. 10, 1978.
 - [25] A. Fedorov, V. Lazarev, I. Makhrov, N. Pozhar, M. Anufriev, A. Pnev, and V. Karasik, "Structural monitoring system with fiber bragg grating sensors: implementation and software solution", *Journal of Physics: Conference Series*, IOP Publishing, vol. 594, 2015, p. 012 049.
 - [26] K. O. Hill and G. Meltz, "Fiber bragg grating technology fundamentals and overview", ["Journal of lightwave technology"](#), vol. 15, no. 8, 1997.
 - [27] T. Yeo, T. Sun, K. Grattan, D. Parry, R. Lade, and B. Powell, "Characterisation of a polymer-coated fibre bragg grating sensor for relative humidity sensing", ["Sensors and Actuators B: Chemical"](#), vol. 110, no. 1, 2005.

BIBLIOGRAPHY

- [28] N. A. David, P. M. Wild, and N. Djilali, "Parametric study of a polymer-coated fibre-optic humidity sensor", "[Measurement Science and Technology](#)", vol. 23, no. 3, 2012.
- [29] T. L. Yeo, T. Sun, K. T. Grattan, D. Parry, R. Lade, and B. D. Powell, "Polymer-coated fiber bragg grating for relative humidity sensing", "[IEEE Sensors Journal](#)", vol. 5, no. 5, 2005.
- [30] Y.-J. Rao, "In-fibre bragg grating sensors", "[Measurement science and technology](#)", vol. 8, no. 4, 1997.
- [31] J. K. Sahota, N. Gupta, and D. Dhawan, "Fiber bragg grating sensors for monitoring of physical parameters: a comprehensive review", "[Optical Engineering](#)", vol. 59, no. 6, 2020.
- [32] Z. Szillási, S. Buontempo, N. Béni, G. Breglio, A. Cusano, A. Laudati, M. Giordano, A. Saccomanno, D. Druzhkin, and A. Tsirou, "One year of fos measurements in cms experiment at cern", "[Physics Procedia](#)", vol. 37, 2012.
- [33] P. Giaccari, H. Limberger, and P. Kronenberg, "Influence of humidity and temperature on polyimide-coated fiber bragg gratings", *Bragg Gratings, Photosensitivity, and Poling in Glass Waveguides*, Optical Society of America, 2001, BFB2.
- [34] P. Kronenberg, P. K. Rastogi, P. Giaccari, and H. G. Limberger, "Relative humidity sensor with optical fiber bragg gratings", "[Optics letters](#)", vol. 27, no. 16, 2002.
- [35] G. Berruti, M. Consales, M. Giordano, L. Sansone, P. Petagna, S. Buontempo, G. Breglio, and A. Cusano, "Radiation hard humidity sensors for high energy physics applications using polyimide-coated fiber bragg gratings sensors", "[Sensors and Actuators B: Chemical](#)", vol. 177, 2013.
- [36] G. M. Berruti, P. Petagna, S. Buontempo, A. Makovec, Z. Szillasi, N. Beni, M. Consales, and A. Cusano, "One year of fbg-based thermo-hygrometers in operation in the cms experiment at cern", "[Journal of Instrumentation](#)", vol. 11, no. 03, 2016.
- [37] L. Inc. (2021), [Online]. Available: <https://lunainc.com/product/si255-optical-sensing-instrument>.
- [38] N. Safari Yazd, J. Kawakami, A. Izaddoost, and P. Mégret, "Effect of peak tracking methods on fbg calibration derived by factorial design of experiment", "Sensors", vol. 21, no. 18, 2021.
- [39] T. Venugopalan, T. Sun, and K. Grattan, "Long period grating-based humidity sensor for potential structural health monitoring", "[Sensors and Actuators A: Physical](#)", vol. 148, no. 1, 2008.
- [40] A. M. Vengsarkar, P. J. Lemaire, J. B. Judkins, V. Bhatia, T. Erdogan, and J. E. Sipe, "Long-period fiber gratings as band-rejection filters", "[Journal of lightwave technology](#)", vol. 14, no. 1, 1996.
- [41] V. Bhatia, "Applications of long-period gratings to single and multi-parameter sensing", "[Optics express](#)", vol. 4, no. 11, 1999.

-
- [42] D. A. C. Enríquez, A. R. da Cruz, and M. T. M. R. Giraldi, "Hybrid fbg-lpg sensor for surrounding refractive index and temperature simultaneous discrimination", *"Optics & Laser Technology"*, vol. 44, no. 4, 2012.
- [43] S. W. James and R. P. Tatam, "Optical fibre long-period grating sensors: characteristics and application", *"Measurement science and technology"*, vol. 14, no. 5, 2003.
- [44] J. Yang, L. Yang, C.-Q. Xu, C. Xu, W. Huang, and Y. Li, "Long-period grating refractive index sensor with a modified cladding structure for large operational range and high sensitivity", *"Applied optics"*, vol. 45, no. 24, 2006.
- [45] M. Consales, G. Berruti, A. Borriello, M. Giordano, S. Buontempo, G. Breglio, A. Makovec, P. Petagna, and A. Cusano, "Nanoscale tio₂-coated lpgs as radiation-tolerant humidity sensors for high-energy physics applications", *"Optics letters"*, vol. 39, no. 14, 2014.
- [46] G. M. Berruti, T. F. P. D. Neves, M. Consales, P. Vaiano, G. Quero, P. Petagna, and A. Cusano, "Radiation sensitivity of long period gratings written in b-ge doped fiber under proton irradiation at cern", *Optical Fiber Sensors*, Optical Society of America, 2018, WF57.
- [47] G. M. Berruti, P. Vaiano, G. Quero, T. F. P. D. Neves, A. Boniello, M. Consales, P. Petagna, and A. Cusano, "Analysis of uncoated lpgs written in b-ge doped fiber under proton irradiation for sensing applications at cern", *"Scientific reports"*, vol. 10, no. 1, 2020.
- [48] L. Scherino, "Fiber optics sensors (fos) in the atlas inner detector", *"Nuclear Instruments and Methods in Physics Research - UNDER REVIEW"*, 2021.
- [49] L. Alwis, T. Sun, and K. Grattan, "Optical fibre-based sensor technology for humidity and moisture measurement: review of recent progress", *"Measurement"*, vol. 46, no. 10, 2013.
- [50] X. Lu, P. J. Thomas, and J. O. Hellevang, "A review of methods for fibre-optic distributed chemical sensing", *"Sensors"*, vol. 19, no. 13, 2019.
- [51] H. C. Hulst and H. C. van de Hulst, *Light scattering by small particles*. Courier Corporation, 1981.
- [52] A. Masoudi and T. P. Newson, "Contributed review: distributed optical fibre dynamic strain sensing", *"Review of Scientific Instruments"*, vol. 87, no. 1, 2016.
- [53] W. Zhi, R. Guobin, L. Shuqin, and J. Shuisheng, "Loss properties due to rayleigh scattering in different types of fiber", *"Optics express"*, vol. 11, no. 1, 2003.
- [54] L. Palmieri and L. Schenato, "Distributed optical fiber sensing based on rayleigh scattering", *"The Open Optics Journal"*, vol. 7, no. 1, 2013.
- [55] B. R. Masters, "Lord rayleigh: a scientific life", *"Opt. Photon. News"*, vol. 20, no. 6, Jun. 2009.
- [56] M. Arumugam, "Optical fiber communication—an overview", *"Pramana"*, vol. 57, no. 5, 2001.

BIBLIOGRAPHY

- [57] M.-J. Li and T. Hayashi, “Advances in low-loss, large-area, and multicore fibers”, *Optical Fiber Telecommunications VII*, Elsevier, 2020, pp. 3–50.
- [58] M. Barnoski and S. Jensen, “Fiber waveguides: a novel technique for investigating attenuation characteristics”, *Applied optics*, vol. 15, no. 9, 1976.
- [59] A. J. Rogers, “Polarization-optical time domain reflectometry: a technique for the measurement of field distributions”, *Applied optics*, vol. 20, no. 6, 1981.
- [60] H. F. Taylor and C. E. Lee, Apparatus and method for fiber optic intrusion sensing, US Patent 5,194,847, 1993.
- [61] Y. Koyamada, M. Imahama, K. Kubota, and K. Hogari, “Fiber-Optic Distributed Strain and Temperature Sensing With Very High Measurand Resolution Over Long Range Using Coherent OTDR”, *Journal of Lightwave Technology*, vol. 27, no. 9, May 2009.
- [62] X. Lu, “Coherent rayleigh time domain reflectometry”, Ph.D. dissertation, EPFL - École polytechnique fédérale de Lausanne, Lausanne, Switzerland, 2016.
- [63] L. Zhang, Z. Yang, N. Gorbatov, R. Davidi, M. Galal, L. Thévenaz, and M. Tur, “Distributed and dynamic strain sensing with high spatial resolution and large measurable strain range”, *Optics Letters*, vol. 45, no. 18, 2020.
- [64] J. Pastor-Graells, H. Martins, A. Garcia-Ruiz, S. Martin-Lopez, and M. Gonzalez-Herraez, “Single-shot distributed temperature and strain tracking using direct detection phase-sensitive otdr with chirped pulses”, *Optics express*, vol. 24, no. 12, 2016.
- [65] M. R. Fernández-Ruiz, L. Costa, and H. F. Martins, “Distributed acoustic sensing using chirped-pulse phase-sensitive otdr technology”, *Sensors*, vol. 19, no. 20, 2019.
- [66] L. Costa, H. F. Martins, S. Martín-López, M. R. Fernández-Ruiz, and M. González-Herráez, “Fully distributed optical fiber strain sensor with $10-12\epsilon/\sqrt{Hz}$ sensitivity”, *Journal of Lightwave Technology*, vol. 37, no. 18, 2019.
- [67] H. Gabai and A. Eyal, “SNR characterization in distributed acoustic sensing”, *Sixth European Workshop on Optical Fibre Sensors*, International Society for Optics and Photonics, vol. 9916, 2016, 99162W.
- [68] M. R. Fernández-Ruiz, H. F. Martins, J. Pastor-Graells, S. Martin-Lopez, and M. Gonzalez-Herraez, “Phase-sensitive otdr probe pulse shapes robust against modulation-instability fading”, *Optics letters*, vol. 41, no. 24, 2016.
- [69] W. Eickhoff and R. Ulrich, “Optical frequency domain reflectometry in single-mode fiber”, *Applied Physics Letters*, vol. 39, no. 9, 1981.
- [70] S. Madabhushi, M. Elshafie, and S. Haigh, “Accuracy of distributed optical fiber temperature sensing for use in leak detection of subsea pipelines”, *Journal of Pipeline Systems Engineering and Practice*, vol. 6, no. 2, 2015.
- [71] C. V. Raman, “A new radiation”, *Indian Journal of physics*, vol. 2, 1928.
- [72] J. Dakin, D. Pratt, G. Bibby, and J. Ross, “Distributed antistokes ratio thermometry”, *Optical Fiber Sensors*, Optical Society of America, 1985, PDS3.

-
- [73] A. Ukil, H. Braendle, and P. Krippner, "Distributed temperature sensing: review of technology and applications", *"IEEE Sensors Journal"*, vol. 12, no. 5, 2011.
- [74] S. W. Tyler, J. S. Selker, M. B. Hausner, C. E. Hatch, T. Torgersen, C. E. Thodal, and S. G. Schladow, "Environmental temperature sensing using raman spectra dts fiber-optic methods", *"Water Resources Research"*, vol. 45, no. 4, 2009.
- [75] L. Brillouin, "Diffusion de la lumière et des rayons x par un corps transparent homogène", *Annales de physique*, vol. 9, 1922, pp. 88–122.
- [76] F. Wang, W. Zhan, X. Zhang, and Y. Lu, "Improvement of spatial resolution for botdr by iterative subdivision method", *"Journal of Lightwave Technology"*, vol. 31, no. 23, 2013.
- [77] R. W. Boyd, *Nonlinear optics*. Academic press, 2007.
- [78] C. A. Galindez-Jamioy and J. M. Lopez-Higuera, "Brillouin distributed fiber sensors: an overview and applications", *"Journal of Sensors"*, vol. 2012, 2012.
- [79] A. Kharaz and B. Jones, "A distributed fibre optic sensing system for humidity measurement", *"Measurement and Control"*, vol. 28, no. 4, 1995.
- [80] C. Galíndez, F. Madruga, M. Lomer, A. Cobo, and J. López-Higuera, "Effect of humidity on optical fiber distributed sensor based on brillouin scattering", Apr. 2008, pp. 70 044–1.
- [81] C. Galindez, F. J. Madruga, and J. M. Lopez-Higuera, "Influence of humidity on the measurement of brillouin frequency shift", *"IEEE Photonics Technology Letters"*, vol. 20, no. 23, 2008.
- [82] S. Liehr, M. Breithaupt, and K. Krebber, "Distributed humidity sensing in pmma optical fibers at 500 nm and 650 nm wavelengths", *"Sensors"*, vol. 17, no. 4, 2017.
- [83] P. J. Thomas and J. O. Hellevang, "A fully distributed fibre optic sensor for relative humidity measurements", *"Sensors and Actuators B: Chemical"*, vol. 247, 2017.
- [84] R. F. Wright, N. Diemler, J. C. Egbu, M. Badar, P. Lu, M. P. Buric, and P. R. Ohodnicki Jr, "Fully distributed optical fiber sensor for humidity monitoring at high temperatures", *Optical Waveguide and Laser Sensors*, International Society for Optics and Photonics, vol. 11405, 2020, 114050E.
- [85] P. Stajanca, K. Hicke, and K. Krebber, "Distributed fiber optic sensor for simultaneous humidity and temperature monitoring based on polyimide-coated optical fibers", *"Sensors"*, vol. 19, no. 23, 2019.
- [86] D. Di Francesca, I. Toccafondo, G. L. Vecchi, S. Calderini, S. Girard, A. Alessi, R. Ferraro, S. Danzeca, Y. Kadi, and M. Brugger, "Distributed optical fiber radiation sensing in the proton synchrotron booster at cern", *"IEEE Transactions on Nuclear Science"*, vol. 65, no. 8, 2018.
- [87] V. Di Murro, L. Pelecanos, K. Soga, C. Kechavarzi, R. F. Morton, and L. Scibile, "Long-term deformation monitoring of cern concrete-lined tunnels using distributed fibre-optic sensing", *"Geotechnical Engineering Journal of the SEAGS & AGSSEA"*, vol. 50, no. 1, 2019.

BIBLIOGRAPHY

- [88] J. A. Kreuz and J. R. Edman, "Polyimide films", ["Advanced Materials"](#), vol. 10, no. 15, 1998.
- [89] T. F. Neves, L. Zhang, F. Yang, K. H. Tow, P. Petagna, and L. Thévenaz, "A kilometre-range distributed relative humidity sensor", *Seventh European Workshop on Optical Fibre Sensors*, International Society for Optics and Photonics, vol. 11199, 2019, p. 1 119 922.
- [90] T. Neves, R. Magalhães, L. Scherino, S. Martin-Lopez, H. F. Martins, P. Petagna, and L. Thévenaz, "Humidity effect on acrylate-and polyimide-coated fibres for distributed sensing applications", *Optical Fiber Sensors*, Optical Society of America, 2020, T3–73.
- [91] P. Petagna, B. Verlaet, and A. Francescon, "Two-phase thermal management of silicon detectors for high energy physics", *Encyclopedia of Two-Phase Heat Transfer and Flow III: Macro and Micro Flow Boiling and Numerical Modeling Fundamentals Volume 4: Special Boiling Topics*, World Scientific, 2018, pp. 335–412.
- [92] A. Jankowski, E. Grabiec, K. Nocoń-Szmajda, A. Marcinkowski, H. Janeczek, and A. Wolińska-Grabczyk, "Polyimide-based membrane materials for co2 separation: a comparison of segmented and aromatic (co) polyimides", ["Membranes"](#), vol. 11, no. 4, 2021.
- [93] A. Zrelli, M. Bouyahi, and T. Ezzedine, "Simultaneous monitoring of humidity and strain based on bragg sensor", ["Optik"](#), vol. 127, no. 18, 2016.
- [94] A. Swanson, S. Raymond, S. Janssens, R. Breukers, M. Bhuiyan, J. Lovell-Smith, and M. Waterland, "Investigation of polyimide coated fibre bragg gratings for relative humidity sensing", ["Measurement Science and Technology"](#), vol. 26, no. 12, 2015.
- [95] I. Yulianti, A. S. M. Supa'at, S. M. Idrus, and M. R. S. Anwar, "Design of fiber bragg grating-based fabry-perot sensor for simultaneous measurement of humidity and temperature", ["Optik"](#), vol. 124, no. 19, 2013.
- [96] P. K. Bachmann, W. Hermann, H. Wehr, and D. U. Wiechert, "Stress in optical waveguides. 2: fibers", ["Applied optics"](#), vol. 26, no. 7, 1987.
- [97] P. J. Thomas and J. O. Hellevang, "A high response polyimide fiber optic sensor for distributed humidity measurements", ["Sensors and Actuators B: Chemical"](#), vol. 270, 2018.
- [98] P. Antunes, F. Domingues, M. Granada, and P. André, Mechanical properties of optical fibers. INTECH Open Access Publisher, 2012.
- [99] L. Silva, S. Tognana, and W. Salgueiro, "Study of the water absorption and its influence on the young's modulus in a commercial polyamide", ["Polymer testing"](#), vol. 32, no. 1, 2013.
- [100] S.-C. Her and C.-Y. Huang, "Effect of coating on the strain transfer of optical fiber sensors", ["Sensors"](#), vol. 11, no. 7, 2011.
- [101] X. Li, S. Lin, J. Liang, Y. Zhang, H. Oigawa, and T. Ueda, "Fiber-optic temperature sensor based on difference of thermal expansion coefficient between fused silica and metallic materials", ["IEEE Photonics Journal"](#), vol. 4, no. 1, 2011.

-
- [102] C. P. Chawla, T. E. Bishop, D. M. Szum, and K. P. Murray, "New test method for determining the water sensitivity of optical fiber coatings", ["Optical Engineering"](#), vol. 30, no. 6, 1991.
- [103] S. C. Shit and P. Shah, "A review on silicone rubber", ["National academy science letters"](#), vol. 36, no. 4, 2013.
- [104] T. Neves, L. Scherino, R. Bernard, M. Bouet, R. Magalhães, H. F. Martins, P. Petagna, and L. Thévenaz, "Humidity insensitive optical fibre for distributed sensing applications at room temperatures", ["Journal of Lightwave Technology - Under Review"](#),
- [105] T. Neves, P. Petagna, and L. Thévenaz, "Humidity insensitive optical fibre for distributed sensing applications", ["Applied Optics - Under Review"](#),
- [106] T. F. Neves, R. Magalhães, L. Scherino, S. Martin-Lopez, H. F. Martins, P. Petagna, and L. Thévenaz, "Cross-sensitivity of coated optical fibre", ["Journal of Lightwave Technology - Submitted"](#),
- [107] C. Ishiyama and Y. Higo, "Effects of humidity on young's modulus in poly (methyl methacrylate)", ["Journal of Polymer Science Part B: Polymer Physics"](#), vol. 40, no. 5, 2002.
- [108] A. Sarkar, S. Izadpanah, T. Bishop, C. Coady, J. Martin, and G. Pasternack, "High performance uv-cured optical fiber primary coating", ["Fiber & Integrated Optics"](#), vol. 6, no. 2, 1987.
- [109] E. Tsai, T. Blanton, D. Harding, and S. Chen, "Temperature dependence of the properties of vapor-deposited polyimide", ["Journal of applied physics"](#), vol. 93, no. 7, 2003.
- [110] T. Neves, P. Petagna, and L. Thévenaz, "Thermo-hygrometer distributed fibre sensor for concrete curing monitoring", ["IEEE Sensors - Under Review"](#),
- [111] D. Gardner, R. Lark, T. Jefferson, and R. Davies, "A survey on problems encountered in current concrete construction and the potential benefits of self-healing cementitious materials", ["Case studies in construction materials"](#), vol. 8, 2018.
- [112] K. Tan and O. E. Gjorv, "Performance of concrete under different curing conditions", ["Cement and Concrete Research"](#), vol. 26, no. 3, 1996.
- [113] T. Ayano and F. H. Wittmann, "Drying, moisture distribution, and shrinkage of cement-based materials", ["Materials and Structures"](#), vol. 35, no. 3, 2002.
- [114] J. Zhang, K. Qi, and Y. Huang, "Calculation of moisture distribution in early-age concrete", ["Journal of engineering mechanics"](#), vol. 135, no. 8, 2009.
- [115] T. Voigt, G. Ye, Z. Sun, S. P. Shah, and K. Van Breugel, "Early age microstructure of portland cement mortar investigated by ultrasonic shear waves and numerical simulation", ["Cement and concrete research"](#), vol. 35, no. 5, 2005.
- [116] V. Baroghel-Bouny, M. Mainguy, T. Lassabatere, and O. Coussy, "Characterization and identification of equilibrium and transfer moisture properties for ordinary and high-performance cementitious materials", ["Cement and concrete research"](#), vol. 29, no. 8, 1999.

BIBLIOGRAPHY

- [117] B. Bissonnette, P. Pierre, and M. Pigeon, "Influence of key parameters on drying shrinkage of cementitious materials", *"Cement and Concrete Research"*, vol. 29, no. 10, 1999.
- [118] İ. B. Topçu and V. B. Elgün, "Influence of concrete properties on bleeding and evaporation", *"Cement and concrete research"*, vol. 34, no. 2, 2004.
- [119] C. Andrade, J. Sarria, and C. Alonso, "Relative humidity in the interior of concrete exposed to natural and artificial weathering", *"Cement and concrete research"*, vol. 29, no. 8, 1999.
- [120] J. Zhang, H. Dongwei, and S. Wei, "Experimental study on the relationship between shrinkage and interior humidity of concrete at early age", *"Magazine of Concrete Research"*, vol. 62, no. 3, 2010.
- [121] S. Taheri, "A review on five key sensors for monitoring of concrete structures", *"Construction and Building Materials"*, vol. 204, 2019.
- [122] T. Geernaert, S. Sulejmani, C. Sonnenfeld, G. Luyckx, K. Chah, L. Areias, P. Mergo, W. Urbanczyk, P. Van Marcke, E. Coppens, *et al.*, "Microstructured optical fiber bragg grating-based strain and temperature sensing in the concrete buffer of the belgian supercontainer concept", *23rd International Conference on Optical Fibre Sensors*, International Society for Optics and Photonics, vol. 9157, 2014, p. 915 777.
- [123] L. Pelecanos, K. Soga, M. Z. Elshafie, N. de Battista, C. Kechavarzi, C. Y. Gue, Y. Ouyang, and H.-J. Seo, "Distributed fiber optic sensing of axially loaded bored piles", *"Journal of Geotechnical and Geoenvironmental Engineering"*, vol. 144, no. 3, 2018.
- [124] Sensohive. (2021), [Online]. Available: <https://sensohive.com/>.
- [125] A. BAdr, W. vAnder Meer, and P. Fischer, "Concremote: application of concrete maturity in digital construction", *"Concrete for the Modern Age Developments in materials and processes"*, 2017.
- [126] J. Zhang, J. Wang, and Y. Gao, "Moisture movement in early-age concrete under cement hydration and environmental drying", *"Magazine of Concrete Research"*, vol. 68, no. 8, 2016.
- [127] F. Matalkah, Y. Jaradat, and P. Soroushian, "Plastic shrinkage cracking and bleeding of concrete prepared with alkali activated cement", *"Heliyon"*, vol. 5, no. 4, 2019.
- [128] H. Henschel, J. Kuhnhehn, and U. Weinand, "Radiation hard optical fibers", *OFC/N-FOEC Technical Digest. Optical Fiber Communication Conference, 2005.*, IEEE, vol. 4, 2005, 4–pp.
- [129] S. Girard, A. Alessi, N. Richard, L. Martin-Samos, V. De Michele, L. Giacomazzi, S. Agnello, D. Di Francesca, A. Morana, B. Winkler, *et al.*, "Overview of radiation induced point defects in silica-based optical fibers", *"Reviews in Physics"*, vol. 4, 2019.

List of Acronyms

CERN	European Organization for Nuclear Research
LINAC	Linear Accelerator
PSB	Proton Synchrotron Booster
PS	Proton Synchrotron
SPS	Super Proton Synchrotron
LHC	Large Hadron Collider
ALICE	A Large Ion Collider Experiment
ATLAS	A Toroidal LHC ApparatuS
CMS	Compact Muon Solenoid
LHCb	Large Hadron Collider beauty
RH	Relative Humidity
FOS	Fibre Optic Sensors
RH-FOS	Relative Humidity Fibre Optic Sensors
FBG	Fibre Bragg Grating
LPG	Long Period Grating
DFOS	Distributed Fibre Optic Sensor
ϕ -OTDR	Phase-sensitive Optical Time-Domain Reflectometry
LASER	Light Amplification by Stimulated Emission of Radiation
SMF	Single-Mode Fibres
PVA	Polyvinyl Alcohol
EM	ElectroMagnetic
OTDR	Optical Time-domain Reflectometry
I-OTDR	Incoherent Optical Time-domain Reflectometry
P-OTDR	Polarization Optical Time-domain Reflectometry
SOP	State of Polarization
RI	Refractive Index
CP- ϕ -OTDR	Chirped-pulse Phase-sensitive Optical Time-domain Reflectometry
DAS	Distributed Acoustic Sensing
SNR	Signal-to-Noise Ratio
OFDR	Optical Frequency-Domain Reflectometry
FFT	Fast Fourier Transform

BFS	Brillouin Frequency Shift
BOTDR	Brillouin Optical Time-Domain Reflectometry
BOTDA	Brillouin Optical Time-Domain Analyser
SBS	Stimulated Brillouin Scattering
CV	Continuous Wave
HCS	Hard Clad Silica
PMMA	PolyMethyl MethAcrylate
POF	Polymer Optical Fibres
OBR	Optical Backscattered Reflectometer
ν -OTDR	Photon-counting OTDR
FUT	Fibre Under Test
DFB	Distributed Feedback
SOA	Semiconductor Optical Amplifier
PG	Pulse Generator
EDFA	Erbium-doped Fibre Amplifier
PD	PhotoDetector
OSA	Optical Spectrum Analyser
VI	Visual Interface
OSC	Oscilloscope
VOA	Variable Optical Attenuators
MFC	Mass Flow Controllers
NI-DAQ	National Instruments Data Acquisition Module
PC	Personal Computer
ECL	External Cavity Laser
BPF	Band Pass Filters
AC	Acrylate
PI	Polyimide
SYNC	Synchronization
CTE	Coefficient of Thermal Expansion
MSE	Mean Squared Error
DWS	Dynamic Water Sensitivity
MCVD	Modified Chemical Vapor Deposition
HL-LHC	High Luminosity Large Hadron Collider
MOFBG	Microstructures Optical Fibre Bragg Grating-based

List of Symbols

Symbol	Unit	Definition
eV	eV	Electron Volt
Gy	Gy	Gray
ϕ		Phase of electric field
λ_B	nm	Bragg's wavelength
Λ	nm	Grating pitch
n_0		Refractive index
ε		Strain
ε_z		Axial strain
ε_r		Radial strain
p_{11}		Principals components of the strain-optic tensor
p_{12}		Principals components of the strain-optic tensor
ξ		Thermo-optic coefficient
P_e		Effective strain-optic coefficient
ν		Poisson's ration
ε_{RH}		Strain induced by relative humidity
ε_T		Strain induced by temperature
S_{RH}		Relative humidity sensitivity
S_T		Temperature sensitivity
\mathbf{P}	$C \cdot m^{-2}$	Polarization vector
\mathbf{D}	$C \cdot m^{-2}$	Electric displacement vector
\mathbf{E}	V/m	Electric field
ϵ_0	F/m	Permittivity of free space
$\boldsymbol{\epsilon}$	F/m	Dielectric tensor of the medium
$\boldsymbol{\chi}$	F/m	Susceptibility tensor
\mathbf{I}		Identity matrix
β		Propagation constant of an optical wave
ω	Hz	Optical angular frequency
E_0	J	Energy of ground state of a molecular
E_1	J	Energy of an exited state of a molecular
c	m/s	Speed of light in free space

T	K	Temperature
I	$\text{W}\cdot\text{m}^2$	Optical intensity
V	m^3	Volume
p	N/m^2	Pressure
s	J/K	Entropy
K_B	$\text{m}^2\text{kg}\cdot\text{s}^{-2}\text{K}^{-1}$	Boltzmann constant
C_T	m^2/N	Isothermal compressibility
P	W	Optical power
W	s	Pulse width
α_s	m^{-1}	Fibre scattering losses
h	$\text{m}^2\cdot\text{kg}/\text{s}$	Planck constant
r_e		Complex reflection coefficient
B_c		Capture coefficient
ν	Hz	Optical wave frequency
Ω_A	Hz	Angular frequency of the thermal vibration
ν_R	Hz	Raman frequency shift
N_{ave}		Average number of phonons
L	m	Fibre length
\mathbf{k}	m^{-1}	Optical wave vector
V_a	m/s	Acoustic velocity
\mathbf{q}	m^{-1}	Acoustic wave vector
ν_a	Hz	Acoustic wave frequency
ν_B	Hz	Brillouin shift
Γ	s^{-1}	Damping factor
g_B	$\text{m}\cdot\text{W}^{-1}$	Brillouin gain factor
ρ	kg^3m^{-3}	Density of a material
A_{eff}	m^2	Effective core area
F	Hz	Frequency scan range
E	Pa	Young's modulus
t	s	Time
β	$\%\text{RH}^{-1}$	Moisture expansion coefficient

List of Publications

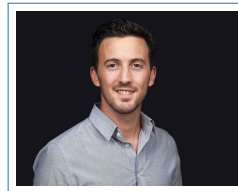
- 2021 - **T. Neves**, L. Scherino, R. Bernard, M. Bouet, R. Magalhães, S. Martin-Lopez, H. F. Martins, P. Petagna and L. Thévenaz, "Humidity Insensitive Fibre for Distributed Fibre Sensing at Room Temperature". IEEE Journal of Lightwave Technology - Under Review
- 2021 - **T. Neves**, P. Petagna and L. Thévenaz, "Distributed thermo-hygrometer for concrete curing process monitoring". IEEE Sensors - Under Review
- 2021 - **T. Neves**, P. Petagna and L. Thévenaz, "Humidity Insensitive Optical Fibre for Distributed Sensing Applications". Applied Optics - Under Review
- 2021 - **T. Neves**, R. Magalhães, L. Scherino, S. Martin-Lopez, H. F. Martins, P. Petagna and L. Thévenaz, "Humidity Cross-sensitivity of Coated Optical Fibres for Sensing Applications", IEEE Photonics Technology Letters, Submitted
- 2021 - R. Magalhães, **T. Neves**, L. Costa, L. Scherino, S. Martin-Lopez, M. Gonzalez-Herraez and H. F. Martins, "Reaching long-term stability in CP-OTDR". IEEE Journal of Lightwave Technology - Submitted
- 2021 - L. Scherino, E. J. Schioppa, A. Arapov, G. M. Berruti, W. J. Bock, A. Boniello, A. Borriello, S. Campopiano, M. Consales, A. Cusano, F. Esposito, A. Iadicco, S. Kachiguine, P. Mikulice, K. Nagai, **T. Neves**, P. Petagna, G. Quero, D. Robinson, A. Srivastava, P. Vaiano, N. Venturi, M. Zarrelli, A. Zotti, S. Zuppolini, "Fiber Optics Sensors (FOS) in the ATLAS Inner Detector". Nuclear Instruments and Methods in Physics Research - Submitted
- 2020 - **T. Neves**, R. Magalhães, L. Scherino, S. Martin-Lopez, H. F. Martins, P. Petagna, and L. Thévenaz, "Humidity effect on acrylate- and polyimide-coated fibres for distributed sensing applications", Optical Fiber Sensors, Optical Society of America, 2020, T3-73
- 2020 - R. Magalhães, **T. Neves**, L. Costa, L. Scherino, P. Petagna, L. Thévenaz, S. Martin-Lopez, M. Gonzalez-Herraez and H. F. Martins, "Reaching mk-scale stability in CP- ϕ -OTDR over daily measurements". Optical Fiber Sensors 27
- 2020 - G. Berruti, P. Vaiano, G. Quero, **T. Neves**, A. Boniello, M. Consales, P. Petagna, A. Cusano, "Analysis of uncoated LPGs written in B-Ge doped fiber under proton irradiation for sensing applications at CERN". Scientific Reports 2020, 10, 1344

- 2019 - **T. Neves**, L. Zhang, F. Yang, K.H. Tow, P. Petagna, L. Thévenaz, "A kilometre-range distributed relative humidity sensor". Proc. SPIE 2019, 11199, 1119922
- 2018 - G. Berruti, **T. Neves**, M. Consales, P. Vaiano, G. Quero, P. Petagna, A. Cusano, "Radiation Sensitivity of Long Period Gratings written in B-Ge doped fiber under proton irradiation at CERN". Proc. 26th Int. Conf. Opt. Fiber Sensors, 2018, Paper WF57

Tiago Neves

Curriculum Vitae

60 Rue Blaise Pascal
01630 Saint-Genis-Pouilly
France
☎ +351918824315
☎ +41227670439
✉ tiago.neves@cern.ch



Personal Information

Date of birth 28/03/1990
Nationality Portuguese
Driving Licence **B**
LinkedIn <https://www.linkedin.com/in/tiago-neves-36b17943/>

Education

07/2017- **PhD**, *École polytechnique fédérale de Lausanne (EPFL)*, Group for Fibre Optics (GFO),
Present Lausanne, Switzerland.
Development of a Kilometre-range Distributed Relative Humidity Fibre Sensor
Defense expected: 30/11/2021

09/2011- **MSc**, *University of Coimbra*, Coimbra, Portugal.
09/2013 Specialization in Instrumentation, Final GPA of 17 out of 20

09/2008- **BSc**, *University of Coimbra*, Coimbra, Portugal.
09/2011 Physics Engineering, Final GPA of 14 out of 20

Work Experience

01/2021 - **CERN: COAS (Corresponding Associateship)**, *EP-DT (Experimental Physics - Detector Technologies) group*, Geneva, Switzerland.
Present

- Development of the first kilometre-range distributed relative humidity sensor prototype.
- Prototype installation, testing and validation in a in-field application.
- Starting the prototype miniaturization process.

07/2017 - **CERN: Doctoral Student**, *EP-DT-FS (Experimental Physics - Detector Technologies - Fluidic System) section*, Geneva, Switzerland.
12/2020

- Development of a new interrogation technique fully capable of measuring temperature and relative humidity over kilometres of sensing range, using optical fibres as the sensing element.
- Finding the best suitable optical fibre for relative humidity and temperature measurements.

05/2015 - **CERN: Trainee Engineer**, *EP-DT Group*, in the frame of the FCT (Portuguese national
04/2017 funding agency for science, research and technology) program, Geneva, Switzerland.

- Improvement and automatization of the thermo-regulated chamber.
 - Graphical user interface development (LabVIEW) for reference sensors acquisition.
 - Mass flow controllers integration and development of their control interfaces.
 - Characterization of the relative humidity and temperature responses of fibre optic sensors.
 - Development of Matlab scripts to analyse the fibre optic sensors data.
 - Preliminary study about the behaviour of LPG sensors under γ ionizing radiation dose.
 - Installation of LPG sensors in ATLAS detector.
- 09/2013 - **ISR: Researcher**, *Institute of Systems and Robotics - University of Coimbra*, Coimbra, Portugal.
- 04/2015
- TIRAMISU (Toolbox Implementation for Removal of Anti-personnel Mines, Sub-munitions and UXO) Project.
 - Landmines' vapour sensor design and development.
 - Sensor's shape optimization.
 - Design and development of a setup to study the optical properties (reflectance, transmittance and absorption) of solid materials.
- 03/2013 - **Unplugg: Engineer**, *Coimbra*, Portugal.
- 10/2013
- Development of a wireless smart meter pulses counter for energy monitoring with real-time readings of the house consumptions.
- 06/2011 - **ISA: Trainee**, *Intelligent Sensing Anywhere*, Coimbra, Portugal.
- 10/2011
- Software and hardware beta tester.
 - Market study about smart LED lighting systems to turn Coimbra into the first LED city in Portugal.
- 09/2009 - **LIP: Researcher**, *Laboratory of Instrumentation and Experimental Particles Physics*, Coimbra, Portugal.
- 09/2010
- Bachelor student trainee.
 - Root introduction.
 - Particles physics introduction.

Publications

- 2021 **T. Neves, L. Scherino, R. Bernard, M. Bouet, R. Magalhães, S. Martin-Lopez, H. F. Martins, P. Petagna and L. Thévenaz**, "Humidity Insensitive Fibre for Distributed Fibre Sensing at Room Temperature", *IEEE Journal of Lightwave Technology* - Under Review.
- 2021 **T. Neves, P. Petagna and L. Thévenaz**, "Distributed thermo-hygrometer for concrete curing process monitoring", *IEEE Sensors*, Under Review.
- 2021 **T. Neves, P. Petagna and L. Thévenaz**, "Humidity Insensitive Optical Fibre for Distributed Sensing Applications", *Applied Optics*, Under Review.
- 2021 **T. Neves, R. Magalhães, L. Scherino, S. Martin-Lopez, H. F. Martins, P. Petagna and L. Thévenaz**, "Humidity Cross-sensitivity of Coated Optical Fibres for Sensing Applications", *IEEE Photonics Technology Letters*, Submitted.

- 2021 R. Magalhães, T. Neves, L. Costa, L. Scherino, S. Martin-Lopez, M. Gonzalez-Herraez and H. F. Martins, "Reaching long-term stability in CP-OTDR", IEEE Journal of Lightwave Technology, Submitted.
- 2021 L. Scherino, E. J. Schioppa, A. Arapov, G. M. Berruti, W. J. Bock, A. Boniello, A. Borriello, S. Campopiano, M. Consales, A. Cusano, F. Esposito, A. Iadicicco, S. Kachiguine, P. Mikulice, K. Nagai, T. Neves, P. Petagna, G. Quero, D. Robinson, A. Srivastava, P. Vaiano, N. Venturi, M. Zarrelli, A. Zotti, S. Zuppolini, "Fiber Optics Sensors (FOS) in the ATLAS Inner Detector", Nuclear Instruments and Methods in Physics Research, Submitted.
- 2020 T. Neves, R. Magalhães, L. Scherino, S. Martin-Lopez, H. F. Martins, P. Petagna and L. Thévenaz, "Humidity Effect on Acrylate- and Polyimide-Coated Fibres for Distributed Sensing Applications", Optical Fiber Sensors 27, 2020.
- 2020 R. Magalhães, T. Neves, L. Costa, L. Scherino, P. Petagna, L. Thévenaz, S. Martin-Lopez, M. Gonzalez-Herraez and H. F. Martins, "Reaching mk-scale stability in CP- ϕ -OTDR over daily measurements", Optical Fiber Sensors 27, 2020.
- 2020 G. Berruti, P. Vaiano, G. Quero, T. Neves, A. Boniello, M. Consales, P. Petagna, A. Cusano, "Analysis of uncoated LPGs written in B-Ge doped fiber under proton irradiation for sensing applications at CERN", Sci. Rep. 2020, 10, 1344.
- 2019 T. Neves, L. Zhang, F. Yang, K.H. Tow, P. Petagna, L. Thévenaz, "A kilometre-range distributed relative humidity sensor", Proc. SPIE 2019, 11199, 1119922.
- 2018 G. Berruti, T. Neves, M. Consales, P. Vaiano, G. Quero, P. Petagna, A. Cusano, "Radiation Sensitivity of Long Period Gratings written in B-Ge doped fiber under proton irradiation at CERN", in Proc. 26th Int. Conf. Opt. Fiber Sensors, 2018, Paper WF57.
- 2017 L. Martelo, T. Neves, J. Figueiredo, L. Marques, A. Federov, A. Charas, M. Berberan-Santos, H. Burrows, "Towards the development of a low-cost device for the detection of explosives vapors by fluorescence quenching of conjugated polymers in solid matrices", MDPI Sensors 2017, 17(11), 2532.
- 2014 T. Neves, L. Marques, L. Martelo, H. Burrows, "Conjugated Polymer-based Explosives Sensor: Progresses in the Design of a Handheld Device", IEEE Sensors 2014, 11, 1415–1418.

Extra Curricular Activities

- 03/2010 - **jeKnowledge Associação: Human Resources Manager**, Coimbra , Portugal.
03/2012
- 02/2012 - **jeKnowledge Associação: General Assembly**, Coimbra , Portugal.
02/2013
- 02/2012 - **jeKnowledge Associação: Treasurer and Administrator**, Coimbra , Portugal.
03/2013
- 02/2013 - **jeKnowledge Associação: Audit Committee**, Coimbra , Portugal.
05/2015
- 04/2012 - **FCTUC: Pedagogical Council**, Faculty of Sciences and Technologies of University of
09/2013 Coimbra, Coimbra, Portugal.

Languages

Portuguese	Native
English	Professional working proficiency
French	Intermediate
Spanish	Intermediate